Implementing plant hydraulics in an Earth System Model and the implications for the global carbon and water cycles

Daniel Joseph Kennedy

Submitted in partial fulfillment of the
requirements for the degree of
Doctor of Philosophy
in the Graduate School of Arts and Sciences

COLUMBIA UNIVERSITY

2020

ABSTRACT

Implementing plant hydraulics in an Earth System Model and the implications for the global carbon and water cycles

Daniel Joseph Kennedy

Uncertainty in the representation of vegetation in Earth System Models is a major contributor to the intermodel spread in climate projections under global warming. Empirical soil moisture stress parameterizations to model drought effects on photosynthesis have been identified as a major driver of this uncertainty, leading to a call to develop more mechanistic models that leverage the principles of soil and plant hydraulic theory. The goal of this dissertation is to develop and install a simplified plant hydraulics representation within a major Earth System Model, compare its dynamics with a non-hydraulic model, and refine methods to use transient leaf water potential observations to infer vegetation water-use strategy.

Chapter 1 presents the full model description of Plant Hydraulic Stress (PHS), which we developed to implement plant hydraulics within the Community Land Model (CLM). PHS has since been adopted as the default representation of vegetation water use in version 5 of the CLM. PHS updates vegetation water stress and root water uptake to better reflect plant hydraulic theory, advancing the physical basis of the modeled vegetation hydrodynamics. Point simulations of a tropical forest site (Caxiuanã, Brazil) under ambient conditions and partial precipitation exclusion highlight the differences between PHS and the previous CLM implementation. Model description and simulation results are contextualized with a list of benefits and limitations of the new model formulation, including hypotheses that were not testable in previous versions of the model. Key results include reductions in transpiration

and soil moisture biases relative to a control model under both ambient and exclusion conditions, correcting excessive dry season soil moisture stress in the control model. The new model structure, which bases water stress on leaf water potential, could have significant implications for vegetation-climate feedbacks, including increased sensitivity of photosynthesis to atmospheric vapor pressure deficit.

Chapter 2 extends the analysis of PHS to the global scale. Historical simulations with and without plant hydraulics are compared to understand the influence on interannual soil moisture and photosynthesis dynamics. The focus of this chapter is on analyzing model dynamics across the semi-arid tropics. The PHS simulation yields longer soil moisture memory and increases interannual photosynthesis variability as compared to the non-hydraulic model. With an analytical derivation and analyses of soil moisture dynamics, we demonstrate the importance of the root water uptake parameterization for soil moisture memory and carbon cycle variability.

Chapter 3 investigates methods to use transient leaf water potential observations to infer vegetation water-use strategy. We use a set of soil-plant-atmosphere models, ranging in complexity, to investigate the underlying meaning of three isohydricity metrics and identify potential classification errors. The model-based approach allows us to derive analytical expressions for the three metrics and to more methodically sample both environmental space and trait space to generate idealized experiments to test the fidelity of the resulting water-use strategy classifications. We consider two previously defined metrics, isohydricity slope and hydroscape area, in comparison to a third metric, relative isohydricity, defined herein. We describe classification challenges resulting from trait coordination and environmental variability, suggest practical recommendations for metric retrieval, and discuss the value

and limitations of isohydricity and the broader pursuit of response-based metrics of vegetation traits. Our results indicate that the major limitations of the isohydricity slope and hydroscape area metrics can be corrected with the relative isohydricity methods described here.

Contents

List of Figures

List of Tables

Acknowledgments

Sometimes it feels like I made it here against all odds, but in reality it is probably more like what they say about former president George W. Bush, that he was born on third base and thinks he hit a triple. Access to the resources that lead to pursuing graduate study are inequitable, and I must acknowledge the tremendous privilege bestowed by my gender, race, class, and background. Let us who have benefitted in this way not take it for granted, but instead do the work to broaden access to include all segments of our society and achieve a much higher level of fairness in educational outcomes.

I owe special gratitude to my very large family for their very enthusiastic support of my academic pursuits. Cousins, nieces, nephews, aunts, uncles, and step-parents have all contributed to the pride and motivation I have felt in pursuit of this degree. I thank my siblings, who have often acted as co-parents: taking me to visit schools, cheering me on at science team competitions, and celebrating each benchmark along this path. And of course I would not be here but for the hard work and support of my parents. Somehow I have never felt there were any limits to what I can achieve, and I suspect I will never fully understand the efforts and machinations on your part to make that possible.

I would like to thank the many graduate students and postdocs of the Gentine Lab and the Columbia Water Center, from whom I learned a tremendous amount about science and how

to be a graduate student. I must pay special thanks to Julia Green, who encountered every piece of bureaucratic red tape about 6-12 months before me, sharing her lessons accordingly. I am grateful to the ad hoc Riverside Ramblers, the running group that helped me maintain a broader perspective and some work-life balance. My best friend through it all was Ruth Oliver, the mentor and role model for whom my praise has no limits.

I would like to thank the Department of Earth and Environmental Engineering for supporting my graduate study, and the School of Engineering for the Presidential Fellowship that allowed me the latitude to undertake a high activation energy research project. I feel very fortunate to have conducted my graduate work here at Columbia University, which supports an incredible diversity of environmental science and engineering research across multiple departments and institutes. Through its classes, seminars, and colloquia I had access to all the resources I could need in support of my research and scholarship. I especially thank Kevin Griffin for his classes and seminars on plant physiology and ecology, which I will always remember fondly.

I must also acknowledge the support of the Terrestrial Sciences Section of the NCAR Climate and Global Dynamics Laboratory, which included funding a four-month visit in 2016, during which much of the work presented here was developed. Computing resources for my work were graciously provided by the Climate Simulation Laboratory at NCAR's Computational and Information Systems Laboratory. I thank Dave Lawrence for marshaling considerable resources in support of my research and for his work developing and maintaining the many platforms I have used to share my work. Likewise I thank Sean Swenson, Rosie Fisher, and Keith Oleson for help conceiving and implementing the work described in Chapters 1 and 2. I especially thank Keith, who had the unfortunate tasks of getting me up

to speed on Yellowstone and figuring out how to extract my plant hydraulics model from an ad-hoc CLM emulator I wrote on my laptop, because I was afraid of the supercomputer. I must also thank Erik Kluzek and Bill Sacks among others for technical support of my work and CLM in general, without which our plant hydraulics model would never see the light of day. Thanks also to the rest of the extended land model working group for support and feedback on my work.

I thank Rosie Fisher, Patrick Meir, Antonio Carlos Lola da Costa, and all those involved in data collection at the Caxiuanã forest throughfall exclusion experiment, which was critical for Chapter 1 of this dissertation. Likewise I acknowledge CNPQ grant 457914/2013-0/MCTI/CNPq/ FNDCT/LBA/ESECAFLOR and U.K. NERC grant NE/J011002 for support of this field work.

Lastly, I must acknowledge the vast array of scientists working in the broad field of ecohydrology, whose work has motivated and substantiated the efforts described here. This includes Kim Novick, who has graciously shared her expertise and experience to help me wade into the isohydricity debate. I am grateful to my dissertation committee members who have helped steer my research and graciously provided their time in support of my academic pursuits. Finally I must thank Pierre Gentine, who has been the ideal advisor, equipped with a surfeit of novel ideas and the generosity to promote my work enthusiastically. Pierre, thank you for your patience and guidance through this process.

Introduction

Overlaid on the long-term trend of increasing atmospheric CO_2 concentration is a seasonal cycle that belies the tremendous influence of plant activity on the global carbon cycle [Keeling, 1960]. Though CO_2 concentrations have been increasing by upwards of 2ppm per year, each year concentrations in Mauna Loa, Hawaii actually tend to decrease from May to September [Le Quéré et al., 2018]. This coincides with the Northern Hemisphere growing season, when CO_2 sinks to photosynthesis can temporarily outpace fossil fuel emissions, due to the large concentration of land mass above the equator. But then, through the Northern Hemisphere winter, global respiration exceeds photosynthesis, with a large portion of the previously fixed carbon returned to the atmosphere. Overall this cycle features an approximately 6ppm seasonal amplitude from peak-to-trough as measured at Mauna Loa, and has been increasing on average by 0.32% per year [Graven et al., 2013]. The fact that this annual cycle is roughly three times the size of the long-term trend indicates the scale of vegetation activity.

Not all of the summer carbon gains are returned to the atmosphere in the winter, but instead, most years a small fraction has remained on land. The long-term terrestrial carbon sink has absorbed as much as one-third of anthropogenic carbon emissions [Keenan and Williams, 2018], representing a valuable ecosystem service that has effectively subsidized

the cost of global warming. However the fate of the terrestrial carbon sink under climate change is highly uncertain, and has been identified as a major source of the disagreement between Earth System Models (ESMs) on future climate projections [De Kauwe et al., 2017, Friedlingstein et al., 2014, Trugman et al., 2018]. Trees face emerging risk from climate change globally, which may lead to increases in mortality and decreases in the terrestrial carbon sink [Allen et al., 2010, Anderegg et al., 2013, McDowell et al., 2016]. Increases in vapor pressure deficit (VPD) are occurring with global warming [Ficklin and Novick, 2017, Seager et al., 2015], and are associated with impacts on vegetation, such as large-scale die-off [Williams et al., 2013, McDowell and Allen, 2015]. In addition to a drying atmosphere, vegetation must adapt to expected increases in precipitation variability [Pendergrass et al., 2017]. Soil moisture has a large influence on long-term carbon uptake in ESMs [Green et al., 2019], but the representation of soil moisture stress on photosynthesis has been identified as a leading cause of intermodel carbon cycle uncertainty [Trugman et al., 2018].

Understanding how the carbon cycle has responded to past environmental variability can be used as an emergent constraint on the sensitivity of future carbon dynamics to climate change [Cox et al., 2013]. ESMs have been shown to systematically overestimate the effect of soil moisture drought on evaporative fluxes [Ukkola et al., 2016, Bonan et al., 2014]. At the same time, climate-vegetation models have underestimated the persistence of drought legacy effects on forest carbon dynamics, which can last 1 to 4 years after severe drought [Anderegg et al., 2015b], and likewise tend to underestimate the correlation between water availability and global carbon dynamics on an interannual basis [Humphrey et al., 2018]. In the tropics models have been shown to exaggerate dry season reductions in photosynthesis [Restrepo-Coupe et al., 2017]. Models that represent plant hydraulics have shown promise

in representing the seasonal and diurnal cycles of water stress [Fisher et al., 2006, Powell et al., 2013, Bonan et al., 2014].

The principles of plant hydraulics can be used to parameterize vegetation water supply and transpiration demand [Sperry and Love, 2015]. Plant hydraulics are used to calculate water supply, typically using an Ohm's law analogy to model water fluxes through the soil-plant-atmosphere continuum (SPAC), with parameters to represent hydraulic conductivity, vulnerability to cavitation and embolism during drought, as well as the capacitance of plant tissue to store water [Tyree and Ewers, 1991]. Likewise steps must be made to estimate root, stem, and crown area/structure [Bohrer et al., 2005]. Root water uptake especially is sensitive to the absolute and relative distribution of root mass throughout the soil column [Bouda and Saiers, 2017, Javaux et al., 2013]. SPAC models can be difficult to parameterize [Verhoef and Egea, 2014], but the various parameters are often correlated [Bartlett et al., 2016], which provides a basis for model dimensionality reduction [Christoffersen et al., 2016].

A wide range of empirical (e.g. Ball et al. [1987]) and optimization-based models (e.g. Cowan and Farquhar [1977]) have been used to model stomatal behavior to predict transpiration demand. Furthermore recent work has developed an approach to unify the two paradigms [Medlyn et al., 2011]. However significant challenges remain in how to adjust these solutions under drought conditions [Zhou et al., 2013]. Incorporating plant water potential, which requires a plant hydraulic supply model, has been shown to improve empirical stomatal models [Anderegg et al., 2017]. Relatedly, several approaches have been devised for how to incorporate soil moisture, hydraulic constraints, and/or hydraulic costs into stomatal optimization [Manzoni et al., 2013b, Novick et al., 2016b, Wolf et al., 2016, Sperry et al., 2017].

Pairing representations of hydraulic water supply and a stomatal model with hydraulic constraints or costs yields a fully functional SPAC model [Sperry and Love, 2015]. Such models range significantly in complexity [Sperry et al., 1998, Bohrer et al., 2005], with multiple reviews cataloguing the history and evolution of SPAC models [Tyree and Ewers, 1991, Fatichi et al., 2016, Mencuccini et al., 2019]. Mounting evidence suggests that hydraulic traits are important regulators of ecosystem response to drought [Choat et al., 2012, Mackay et al., 2015, Giardina et al., 2018, Anderegg et al., 2018]. This and other work has served to inspire multiple calls to represent plant hydraulics in the next generation of ESMs [Joetzjer et al., 2014, Trugman et al., 2018], and two such implementations in prominent ecosystem demography models [Xu et al., 2016, Christoffersen et al., 2016]. Likewise, this has served to motivate my work to install a plant hydraulics scheme within the Community Land Model, the land component of the Community Earth System Model.

Finally, we must consider the availability of data to constrain and evaluate such models. Site-level data, including experimental manipulations, provide the most detail for evaluation including potentially observations of sap flux, soil moisture, basal increment, and leaf gas exchange. Such data have been used in many instances to evaluate ESMs and/or plant hydraulic models (e.g. Fisher et al. [2006, 2007], Powell et al. [2013], Joetzjer et al. [2014] among many others). Site-based model evaluation can likewise leverage the availability of site-level forcing data and parameters, such as the soil properties measured in Fisher et al. [2008], which were used in Chapter 1. Eddy covariance methods provide a level of automation that allows for continuous observation of gas exchange from forests, albeit integrated across the flux tower footprint [Baldocchi et al., 2001]. Such observations have likewise been a valuable resource for model evaluation, for example as in Bonan et al. [2014], which tests

an implementation of the SPA model [Williams et al., 1996] across six Ameriflux sites, finding that a non-hydraulic modeling approach systematically over-estimated vegetation water stress. Lastly is the constellation of Earth-observing satellites, which have been referred to as flux towers in the sky and can offer insights into photosynthesis, transpiration, soil moisture, and vegetation water content, subject to retrieval error and potentially coarse spatial/temporal resolution [Schimel et al., 2019]. Leveraging satellite observations to infer vegetation traits is an area of active research [Momen et al., 2017, Konings and Gentine, 2017], with applications across multiple vegetation biomes [Konings et al., 2017, Giardina et al., 2018].

This dissertation is comprised of three chapters, which describe and analyze a novel plant hydraulics model, as well as develop techniques to better leverage available observations of leaf water potential to infer vegetation water use strategy.

Chapter 1 presents the full model description of Plant Hydraulic Stress (PHS), which is now the default representation of vegetation water use in version 5 of the Community Land Model. PHS updates vegetation water stress and root water uptake to better reflect plant hydraulic theory, advancing the physical basis of the modeled vegetation hydrodynamics. Point simulations of a tropical forest site (Caxiuanã, Brazil) under ambient conditions and partial precipitation exclusion highlight the differences between PHS and the previous CLM implementation. The new model structure, which bases water stress on leaf water potential, could have significant implications for vegetation-climate feedbacks, including increased sensitivity of photosynthesis to atmospheric vapor pressure deficit.

Chapter 2 extends the analysis of PHS to the global scale. Historical simulations with and without plant hydraulics are compared to understand the influence on interannual soil

moisture and photosynthesis dynamics. The focus of this chapter is on analyzing model dynamics in a broad semi-arid tropical domain. The PHS simulation yields longer soil moisture memory and increases interannual photosynthesis variability as compared to the non-hydraulic model. With an analytical derivation and analyses of soil moisture dynamics, we demonstrate the importance of the root water uptake parameterization for soil moisture memory and carbon cycle variability.

Chapter 3 investigates methods to use transient leaf water potential observations to infer vegetation water-use strategy. We consider two established metrics, isohydricity slope and hydroscape area, in comparison to a third metric, relative isohydricity, defined herein. We describe classification challenges resulting from trait coordination and environmental variability, suggest practical recommendations for metric retrieval, and discuss the value and limitations of isohydricity and the broader pursuit of response-based metrics of vegetation traits. Our results indicate that the major limitations of the isohydricity slope and hydroscape area metrics can be corrected with the relative isohydricity methods described here.

Chapter 1

Implementing plant hydraulics

in the Community Land Model, version 5

1.1 Introduction

Trees face emerging risk from climate change globally, which may lead to increases in mortality and decreases in the terrestrial carbon sink [Allen et al., 2010, Anderegg et al., 2013, McDowell et al., 2016]. In addition to stress from soil moisture drought, vegetation is susceptible to increasing atmospheric demand for evapotranspiration [Restaino et al., 2016, Novick et al., 2016a, Lemordant et al., 2018]. Increases in vapor pressure deficit (VPD) are occurring with global warming [Ficklin and Novick, 2017, Seager et al., 2015], and are associated with impacts on vegetation, such as large-scale die-off [Williams et al., 2013, McDowell and Allen, 2015]. Understanding vegetation response to environmental drivers is important both for discerning future climate impacts on forests and for modeling feedbacks to the carbon and hydrological cycles [Lemordant et al., 2018]. Significant uncertainty remains in Earth System Model (ESM) predictions of the carbon cycle, partly attributed to the response of vegetation to changes in hydroclimate [De Kauwe et al., 2017, Friedlingstein et al., 2014, Trugman et al., 2018].

Soil moisture stress parameterizations are used by ESMs to determine the regulation of

surface fluxes (photosynthesis, transpiration) by vegetation in response to water fluctuations [Egea et al., 2011, Verhoef and Egea, 2014]. Such parameterizations relate a metric of soil moisture status to leaf gas exchange, defining the response of stomatal conductance to declining soil water, serving to attenuate transpiration, photosynthesis, and root water uptake with drying. Water stress dynamics have broad effects on critical land surface processes within models [Joetzjer et al., 2014], such as evapotranspiration. Likewise, because vegetation water use strategies modulate carbon uptake, creating a close coupling between the Earth System's carbon and hydrological cycles [Green et al., 2017], vegetation water stress regulates the global carbon cycle. This occurs on seasonal and interannual timescales, with stress attenuating transpiration [De Kauwe et al., 2015] and photosynthesis [Stocker et al., 2018]. Furthermore, water stress parameterizations influence the diurnal cycle, through the partitioning of latent versus sensible heat, modifying the Bowen ratio [Gentine et al., 2007, 2011]. This in turn feeds back onto surface and air temperature, through land-atmosphere feedbacks [Bonan, 2008, Seneviratne et al., 2006]. Recent studies have shown that soil moisture stress functions are a major driver of uncertainty in leaf gas exchange in ESMs [Trugman et al., 2018] and can systematically overestimate the effect of soil moisture drought on evaporative fluxes [Ukkola et al., 2016, Bonan et al., 2014]. In Amazonia, which is the focus area of our model test runs, studies suggest that the CLM (version 3.5) simultaneously underestimates the effect of experimental drought treatment [Powell et al., 2013] and overestimates dry-season reductions in GPP [Restrepo-Coupe et al., 2017].

More mechanistic representations of stress and vegetation water use dynamics have been achieved by incorporating plant hydraulic theory into land surface models, modeling water flow throughout the Soil-Plant-Atmosphere continuum (SPAC)[Xu et al., 2016, Christof-

fersen et al., 2016, Sperry et al., 2017]. Explicit modeling of water flow through the vegetation substrate increases model complexity, but is consistent with evidence of dynamic regulation of vegetation water use in response to both soil and atmospheric drying [Tardieu and Simonneau, 1998, Sperry et al., 1998, Sperry and Love, 2015]. Furthermore, because they are based on Darcy's Law, plant hydraulic models have a robust physical basis compared to models that utilize empirical water stress formulations. Plant hydraulic models involve new parameters, which may prove challenging to constrain [Drake et al., 2017], but plant hydraulic trait data are available [Kattge et al., 2011, Anderegg, 2015a], providing constraints on parameter estimation. Such trait data have been shown to improve predictions of species vulnerability to drought [Choat et al., 2012, Mackay et al., 2015, Powell et al., 2018, Giardina et al., 2018, Anderegg et al., 2018]. Likewise vegetation water status observations are now available from remote sensing platforms, at a scale that is directly comparable to model development [Konings et al., 2016, Grant et al., 2016] and therefore can be used to validate model results [Momen et al., 2017, Konings et al., 2017].

In this study, we develop a new plant water stress parameterization based on hydraulic theory within the recently released Community Land Model, version 5 (CLM5, the land component of the Community Earth System Model, version 2). We refer to this hydraulics-based implementation as the 'Plant Hydraulic Stress' (PHS) configuration. Previous versions of the CLM employed an empirical soil moisture stress function, as described above.

PHS, by explicitly representing plant hydraulics, introduces modeled vegetation water potential (discretized into leaf, stem and root elements) into the CLM, as well as a physical model of water supply, from the soil through the vegetation substrate. Transpiration is attenuated in the model based on leaf water potential, capturing dynamic vegetation water

use regulation in response to both soil moisture and atmospheric evaporative demand. These changes in the parameterization framework have numerous implications, including:

1. Leaf water potential serves as a metric for plant water status instead of soil water or soil matric potential. As such, it reflects vegetation sensitivity to both soil and atmospheric drying, while serving as a diagnostic for excessive xylem tension and cavitation risk.
2. Using a Darcy's Law approximation to model plant hydrodynamics allows representation of hydraulic redistribution [Lee et al., 2005], as water fluxes are always directed down gradients of water potentials.
3. Root water potential can be used to predict gradient-based root water uptake approximated by Darcy's law, replacing the previous empirical transpiration partitioning heuristic. This provides the means to vary, for example, the mean depth of extraction with changing soil water conditions.
4. Representation of a range of water use strategies (e.g. isohydricity and anisohydricity), improving the connection between leaf gas exchange and water availability.
5. Modeling vegetation water potential allows improved connection to remote sensing observations of vegetation water status (Vegetation Optical Depth) [Konings et al., 2016].

To assess the new model formulation, we carried out site-level simulations at Caxiuanã National Forest in Brazil, a terra-firme moist tropical evergreen forest [Fisher et al., 2006]. Starting in 2001, a plot at this site was subjected to an approximately 50% percent precipitation throughfall exclusion. Due to the large drop in soil moisture at the precipitation exclusion site, significant vegetation water stress regulation of transpiration and photosyn-

thesis was observed [da Costa et al., 2010, 2014], providing a drought signal to demonstrate model dynamics [Fisher et al., 2007].

In this chapter, I therefore:

1. Introduce the PHS theory and implementation in the CLM (Section 1.2)
2. Describe the details of the experiment setup (Section 1.3)
3. Analyze the dynamics of modeled water stress, root water uptake, transpiration, and soil moisture profiles (Section 1.4)
4. Discuss differences between PHS and the previous CLM water stress configuration (Section 1.5)
5. Outline the benefits and limitations of the new model (Section 1.5.5)

1.2 Model description

This study develops a new parameterization of water stress (Sections 1.2.4 and 1.2.5) and root water uptake (Sections 1.2.4 and 1.2.5) within the CLM. We use two configurations of CLM5 to compare the new parameterization with the corresponding parameterization from CLM4.5. The new parameterization is called Plant Hydraulic Stress (PHS); PHS is the default configuration of CLM5. The alternative configuration, which we refer to as Soil Moisture Stress (SMS), deploys the CLM4.5 default root water uptake and water stress implementations within CLM5. In Sections 1.2.1-1.2.3, we describe the components that the two configurations share in common. In Sections 1.2.4 and 1.2.5, we describe their differences.

1.2.1 Stomatal conductance

CLM5 implements the Medlyn stomatal conductance model [Franks et al., 2018, Medlyn et al., 2011], which reconciles the empirical approach to modeling stomatal conductance with a carbon-water optimization framework [Cowan and Farquhar, 1977]. The Cowan and Farquhar [1977] optimization requires plants to maximize photosynthesis relative to transpiration costs, which the Medlyn model captures in an empirically tractable form (Equation 1.1). Stomatal conductance of water (g_s) is directly related to net photosynthesis (A_n) and inversely related to the square root of the vapor pressure deficit near the leaf surface ($\sqrt{D}$) and the concentration of CO_2 at the leaf surface (C_a).

$$g_s = g_0 + 1.6 \left(1 + \frac{g_1}{\sqrt{D}}\right) \frac{A_n}{C_a} \tag{1.1}$$

The model features two parameters: g_0 (μmol / m^2 / s) and g_1 (kPa$^{0.5}$). The g_0 parameter is the minimum stomatal conductance, representing cuticular and epidermal losses (small). The g_1 parameter relates to the marginal water cost guiding the optimization of carbon assimilation. These parameters are plant functional type dependent.

While maximizing assimilation relative to water transpiration costs, the Medlyn model does not resolve concurrent limitations to stomatal conductance associated with declining soil water (such as in Manzoni et al. [2013b]) or excessive xylem tension. To represent such water stress, and its impact on leaf-gas exchange, land surface models typically include a 'water stress factor'. The PHS implementation follows this approach, using the Medlyn model to calculate stomatal conductance absent water stress, which is attenuated as leaf water potential declines (see Section 1.2.3). More recent stomatal conductance models eschew

the Cowan and Farquhar [1977] optimization in favor of a framework to maximize carbon assimilation relative to hydraulic costs [Wolf et al., 2016, Sperry et al., 2017, Anderegg et al., 2018b], which directly incorporate leaf water potential and hydraulic safety margin into the stomatal conductance formulation. Such models do not require a water stress factor and should be tested for future versions of PHS.

1.2.2 Photosynthesis

The CLM5 photosynthesis model is described in detail in Bonan et al. [2011], Thornton and Zimmermann [2007], and Oleson et al. [2013]. Photosynthesis is limited by three factors: carboxylation-limitations, light-limitations, and export-limitations following Farquhar et al. [1980] and Harley et al. [1992]. Water stress (as discussed in the next section) is applied within the carboxylation-limited regime, by attenuating the maximum rate of carboxylation (V_{cmax}). The implementation extends Sellers et al. [1996a,b] with co-limitation following Collatz et al. [1991].

The CLM5 photosynthesis module, in its default configuration, is a two-big-leaf model, with a sunlit and shaded leaf for each plant functional type [Thornton and Zimmermann, 2007, Dai et al., 2004, Oleson et al., 2013]. The canopy fluxes module iterates the solution for leaf temperatures to satisfy the leaf surface energy balances on both sunlit and shaded leaves, in response to forcing conditions. Within this, the photosynthesis module further iterates to solve for stomatal conductance and intercellular CO_2 concentration, balancing stomatal flux of CO_2 with photosynthetic assimilation flux of CO_2 (see Appendix Figure A.1 for a flow chart of these iterations).

1.2.3 Water stress factor

Uncertainty remains within the literature as to how and where to apply water stress factors to photosynthesis and/or stomatal conductance [Zhou et al., 2013, Novick et al., 2016b, Sperry and Love, 2015]. In the CLM, the water stress factor (f_w) multiplies the 'well-watered rate' of maximum carboxylation ($V_{\text{cmax,ww}}$) to effect water stress (as described in Oleson et al. [2013]).

$$V_{\text{cmax}} = f_w \, V_{\text{cmax,ww}} \tag{1.2}$$

Attenuating V_{cmax} is not the only method for incorporating a response to declining water availability. Other models opt to apply water stress directly to stomatal conductance, linking the stomatal conductance model slope parameter to soil moisture (e.g. De Kauwe et al. [2015]). However, Lin et al. [2018] found that only the intercept parameter and photosynthesis (through changes in light-use efficiency) were sensitive to soil moisture based on eddy-covariance observations and not the slope parameter. Furthermore Zhou et al. [2013] suggest that changes in assimilation tend to exceed those predicted by modulating g_1 with soil moisture, but could be captured by changing V_{cmax}. These results would thus suggest that it is appropriate to modulate V_{cmax}. Other field studies, however, suggest that measured V_{cmax} at the leaf level does not change with drought [Flexas et al., 2004]. On the other hand, the modeled V_{cmax} is a bulk measure of V_{cmax} and may implicitly account for mesophyll conductance changes [Rogers et al., 2017], which has been shown to be water stress dependent [Flexas et al., 2012].

For now, applying water stress through V_{cmax} seems well-supported, but future refine-

ments may be appropriate. In this study, we preserve the method of applying water stress used in CLM4.5, while instead experimenting with how f_w responds to environmental conditions.

1.2.4 SMS (CLM4.5 default)

SMS water stress factor

In SMS, f_w is calculated as the summation of a soil layer wilting factor (w_i) across the n soil layers, weighted by root fraction (r_i) [Oleson et al., 2013]. The soil wilting factor is a bounded linear function of soil matric potential ($\psi_{\text{soil},i}$). The function is defined by two parameters, the soil potential at (and above) which stomates are fully open (ψ_o) and the value at which stomates are fully closed (ψ_c).

$$f_{w,\text{SMS}} = \sum_{i=1}^{n} r_i w_i \tag{1.3}$$

$$w_i = 0 \leq \frac{\psi_{\text{soil},i} - \psi_c}{\psi_o - \psi_c} \leq 1 \tag{1.4}$$

SMS root water uptake

The CLM features a vertically discretized soil column with variable soil layer thicknesses. The number of soil layers (n) can vary, depending on the depth to bedrock. Soil water movement in each soil layer is governed by Richards' equation, with root water uptake (q_i) incorporated as a sink term. Summed over the soil column, root water uptake is required to equal transpiration (T).

$$T = \sum_{i}^{n} q_i \tag{1.5}$$

In the SMS configuration, a heuristic function (based on $f_{w,\mathrm{SMS}}$) is used to determine q_i. Transpiration is partitioned among the soil layers based on the product of the root fraction and the wilting factor, which is then normalized by $f_{w,\mathrm{SMS}}$ to satisfy Equation 1.5. Because the relative root fractions are used to partition transpiration, root water uptake is not connected to absolute root biomass. For example, if root biomass doubles in every soil layer, the relative root fractions do not change, with no impact on modeled soil water availability.

$$q_i = \frac{r_i w_i}{f_{w,\mathrm{SMS}}} T \tag{1.6}$$

Substituting for w_i yields the SMS root water uptake equation as a function of the layer-i soil potential ($\psi_{\mathrm{soil},i}$).

$$q_i = \begin{cases} 0 & \text{if } \psi_{\mathrm{soil},i} < \psi_c \\ \dfrac{T}{f_{w,\mathrm{SMS}}} \dfrac{r_i}{\psi_o - \psi_c} \left(\psi_{\mathrm{soil},i} - \psi_c\right) & \text{if } \psi_c \leq \psi_{\mathrm{soil},i} \leq \psi_o \\ \dfrac{T}{f_{w,\mathrm{SMS}}} r_i & \text{if } \psi_{\mathrm{soil},i} > \psi_o \end{cases} \tag{1.7}$$

In the Darcy framework, water fluxes are the product of hydraulic conductance (k_i) and hydraulic gradient ($\Delta\psi$). Although SMS does not explicitly calculate hydraulic conductance, Equation 1.7 can be used to define hydraulic analogs resulting from the transpiration partitioning heuristic function, allowing easier comparison to the PHS root water uptake

implementation.

$$
\begin{aligned}
q_i &= -k_i \Delta\psi \\
\Delta\psi &= \psi_c - \psi_{\text{soil},i} \\
k_i &= \frac{T}{f_{w,\text{SMS}}} \frac{r_i}{\psi_o - \psi_c} \qquad (1.8) \\
\text{constrained by:} \qquad \Delta\psi &= \begin{cases} 0 & \text{if } \psi_{\text{soil},i} < \psi_c \\ \psi_c - \psi_o & \text{if } \psi_{\text{soil},i} > \psi_o \end{cases}
\end{aligned}
$$

1.2.5 PHS (CLM5 default)

PHS water stress factor

PHS introduces a new formulation for f_w, which is based on leaf water potential (ψ_{leaf}) instead of soil potential (described further in Section 1.2.5). The relationship is modeled with a sigmoidal function, subject to two parameters: the water potential at 50% loss of stomatal conductance (p_{50}) and a shape-fitting parameter (c_k).

$$f_{w,\text{PHS}} = 2^{-\left(\frac{\psi_{\text{leaf}}}{p_{50}}\right)^{c_k}} \qquad (1.9)$$

$$\psi_{\text{leaf}} = \psi_{\text{soil}} + \Delta\psi \qquad (1.10)$$

Utilizing leaf water potential has been shown to improve stomatal models [Anderegg et al., 2017] and reflects hydraulic limits on plant transpiration [Manzoni et al., 2013a, Sperry et al., 1998]. Leaf water potential is modulated by supply of sap to the leaves and by evaporative

demand, as regulated by stomatal dynamics [Sperry and Love, 2015]. As a result, low soil water induces stress due to limited water supply, but in addition, high atmospheric VPD can induce stress with the associated increases in the gradient in water potential across the plant xylem. This latter mechanism was absent from the previous water stress function (dependent on soil water potential only), by construction. Given the observed increase in VPD with global warming, it appears critical to include such mechanistic dependence of water stress [Novick et al., 2016a]. While the Medlyn stomatal conductance model does depend on VPD, the model does not (given constant g_1) reflect the risk of hydraulic failure [Zhou et al., 2013]. The new stress factor formulation reflects the dual risks of soil moisture deficit and atmospheric demand on hydraulic safety [Williams et al., 2013], requiring vegetation to avoid excessive xylem tension associated with risk of cavitation.

PHS root water uptake

PHS implements an alternative to the SMS heuristic approach for root water uptake, using a mechanistic representation utilizing Darcy's Law for flow through porous media to approximate the vegetation water fluxes. Instead of a constant parameter (ψ_c) defining the gradient in water potential within the SMS hydraulic analogy (Equation 1.8), PHS implements a physical model of vegetation water potential (details in Section 1.2.5). The water flux from a given soil layer is driven by the gradient between soil potential ($\psi_{\text{soil},i}$) and the water potential in the root collar (ψ_{root}), after accounting for the effects of gravity ($\rho g z_i$, where z_i is the soil layer depth). Hydraulic conductance across the soil and roots (k_{sr}) is modeled based on soil hydraulic properties and xylem vulnerability, accounting for both the path across the soil matrix and through the xylem conduits. Furthermore, in lieu of using

relative root fraction (as in SMS), k_{sr} depends on the root area index, an absolute measure of root abundance (details in Appendix Section A.1).

$$q_i = -k_{sr,i} \left(\psi_{\text{root}} - \psi_{\text{soil},i} + \rho g z_i \right) \tag{1.11}$$

Modeling vegetation water potential

The PHS model within CLM5 uses Darcy's law to approximate the flow of water through the SPAC, which can be represented with an electrical circuit analogy (Figure 1.1). PHS solves for vegetation water potential along the path from soil-to-atmosphere. Vegetation water supply and demand are both coupled to vegetation water potential, as described in the previous two sections. The solution for vegetation water potential is the set of values that matches supply with demand, maintaining water balance across each of the vegetation water potential nodes.

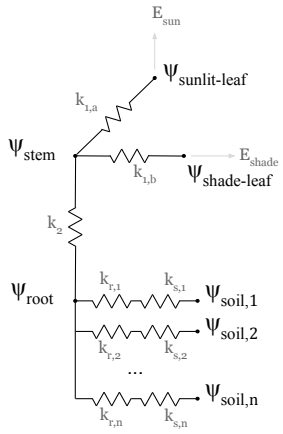

Figure 1.1: Plant hydraulic circuit analog schematic

PHS solves for vegetation water potential at four locations: ψ_{root}, ψ_{stem}, $\psi_{\text{shade-leaf}}$, and $\psi_{\text{sun-leaf}}$. The number of nodes is chosen as the strict minimum to allow for differences in segment parameterizations [Simonin et al., 2015, Sperry and Love, 2015], while also conform-

ing to existing CLM model structure (vertically discretized soil layers, 2-big-leaf). At each node in the circuit diagram (Figure 1.1), we model water potential, and, between nodes, we resolve the flux of water based on Darcy's law. Water uptake from the different soil layers is assumed to operate in parallel; a typical assumption justified by higher resistance in lateral versus central roots (e.g. Williams et al. [2001]). Two resistors operate in series between each ψ_{soil} and ψ_{root}, to represent the path across the soil matrix and then through the root tissue [Williams et al., 1996]. Specifics on the parameterization of hydraulic conductance for each segment are provided in Appendix Section A.1.1. Solving for vegetation water potential requires matching vegetation water supply (root water uptake, sap flux through the stem) with vegetation water demand (sunlit and shaded leaf transpiration).

Water supply

Water supply is modeled via Darcy's Law, where the flux of water (q) is the product of the path hydraulic conductance (k) and the gradient in water potential ($\psi_2 - \psi_1$) after accounting for gravitational potential ($\rho g \Delta z$). Equation 1.12 represents the flow from a generic node 1 to node 2.

$$q = -k\left(\psi_2 - \psi_1 + \rho g \Delta z\right) \tag{1.12}$$

For simplicity, PHS does not represent plant tissue water storage (or capacitance, using the electrical circuit analogy), which is in line with recent supply-loss theory [Sperry and Love, 2015]. Capacitance significantly complicates the water potential solution [Celia et al., 1990] and is challenging to parameterize [Bartlett et al., 2016]. However, buffering of water

stress provided by tissue water storage could potentially be important especially on sub-daily timescales [Meinzer et al., 2009, Epila et al., 2017], whereby its inclusion may be warranted in future model versions.

Hydraulic conductance through vegetation segments is modeled following empirical xylem vulnerability curves [Tyree and Sperry, 1989], where segments lose conductance with increasing xylem tension related to cavitation and embolism [Holbrook et al., 2001]. The vulnerability curves model loss of conductance relative to maximum conductance ($k_{\max}$) using two parameters: c_k, a sigmoidal shape-fitting parameter, and p_{50}, the water potential at 50% loss of segment conductance (following Gentine et al. [2016]).

$$k = k_{\max} 2^{-\left(\frac{\psi_1}{p_{50}}\right)^{c_k}} \tag{1.13}$$

Both c_k and p_{50} can be estimated from field experiments [Sack et al., 2002], and p_{50} is available in the TRY trait database [Kattge et al., 2011]. Parameterization based on p_{50} aligns with the call for a transition to models that use a wider range of plant functional trait data in their parameterization [Anderegg, 2015a]. The loss of xylem conductivity is based on lower terminal water potential (ψ_1) as is typical in other simplified models [Xu et al., 2016], but may underestimate the integrated loss of conductivity [Sperry and Love, 2015]. This bias could underestimate hydraulic limits on gas exchange and/or affect parameter estimation (e.g. requiring lower $k_{\max}$). Likewise, xylem are assumed to symmetrically regain conductance, which may lead to underestimating persistent drought legacies [Anderegg et al., 2015b]. PHS was explicitly designed as a simplified model that can be refined in future versions.

PHS models root, stem, and leaf tissue conductances according to equation 1.13. The parameterization of $k_{\max}$ varies by hydraulic segment. The conductances across the soil matrix ($k_{s,1}$,...,$k_{s,n}$) to the root surface follows Williams et al. [2001] and Bonan et al. [2014], which scales soil conductivity [Brooks and Corey, 1964, Clapp and Hornberger, 1978] by an appropriate conducting distance based on the root distribution. Details are provided in Appendix Section A.1.1

Water demand

Water demand is calculated using the Medlyn stomatal conductance model (see Section 1.2.1) modulated by the CLM water stress factor. As discussed earlier f_w is based on leaf water potential in PHS, where stress increases as leaf water potential becomes more negative [Klein and Niu, 2014]. Emerging from this new stress formulation is a connection between drought stress and hydraulic safety margin (HSM), which measures the difference between the minimum leaf water experienced by vegetation and the water potential at a given percent loss of conductivity (e.g. $HSM = p_{50} - \psi_{\text{leaf,min}}$). Variations in HSM have been shown to explain a significant portion of the variance in ecosystem drought sensitivity [Anderegg et al., 2018].

$$\begin{aligned} f_{w,sun} &= 2^{-\left(\frac{\psi_{\text{sun-leaf}}}{p_{50}}\right)^{c_k}} \\ f_{w,shade} &= 2^{-\left(\frac{\psi_{\text{shade-leaf}}}{p_{50}}\right)^{c_k}} \end{aligned} \tag{1.14}$$

Because leaf water potential is modeled separately for sunlit and shaded leaves, f_w takes on distinct sunlit and shaded values. Shaded and sunlit leaf transpiration (E_{sun}, E_{shade})

are calculated by attenuating maximal transpiration ($E_{\text{sun,max}}$,$E_{\text{shade,max}}$) according to f_w. $E_{\text{sun,max}}$ and $E_{\text{shade,max}}$ are calculated at the beginning of each timestep by running the stomatal conductance model with $f_w = 1$. Equations (1.14) and (1.15) reflect a simplification used within iterations of the PHS module, neglecting non-linear components of the relationship between stress and transpiration (which is resolved through iteration, as described in Appendix Section A.1.3).

$$\begin{aligned} E_{\text{sun}} &= f_w E_{\text{sun,max}} \\ E_{\text{shade}} &= f_w E_{\text{shade,max}} \end{aligned} \tag{1.15}$$

PHS solution

PHS solves for the set of vegetation water potential values (ψ) that matches water supply (root water uptake) to water demand (transpiration), while satisfying continuity across the four water flow segments (soil-to-root, root-to-stem, stem-to-leaf, and leaves-to-transpiration). Beginning from an initial condition of ψ (from the previous timestep), PHS computes the flux divergence f (representing the mismatch of flow in and out of each segment) and iteratively updates ψ until it reaches convergence, i.e. $f \to 0$.

$$\psi = \begin{bmatrix} \psi_{\text{sun}} \\ \psi_{\text{shade}} \\ \psi_{\text{stem}} \\ \psi_{\text{root}} \end{bmatrix} \tag{1.16}$$

$$f(\psi) = \begin{bmatrix} E_{sun} - q_{sun} \\ E_{shade} - q_{shade} \\ q_{sun} + q_{shade} - q_{stem} \\ q_{stem} - \sum_{j=1}^{n} q_{root,j} \end{bmatrix} \tag{1.17}$$

$$A = \frac{df}{d\psi} \tag{1.18}$$

While $|f| > 0$

$$\begin{aligned} \Delta\psi &= A^{-1} f(\psi_i) \\ \psi_{i+1} &= \psi_i + \Delta\psi \end{aligned} \tag{1.19}$$

The numerics are tractable because f has continuous, analytical derivatives and A (a 4x4 matrix with six null entries) is easy to invert when well-conditioned. Supply and demand converge, because transpiration demand decreases with more negative leaf water potentials and supply increases with more negative leaf water potentials. The PHS loop is nested within iterations for intercellular CO_2 concentration and leaf temperature. Details on the numerical implementation are provided in Appendix Section A.1.3.

1.3 Experiment description

We use a set of four simulations to demonstrate the impact of the plant hydrodynamics model (PHS versus SMS) on a tropical rainforest site, under ambient conditions and partial precipitation throughfall exclusion. This site is located in Eastern Amazonia (Caxiuanã,

Table 1.1: Select parameter values

Full Name	Symbol	Value
Maximum Sun Branch Conductance	$k_{\text{sun,max}}$	4e-8 s^{-1}
Maximum Shade Branch Conductance	$k_{\text{shade,max}}$	4e-8 s^{-1}
Maximum Stem Conductivity	$k_{\text{stem,max}}$	4e-8 m/s
Maximum Root Conductivity	$k_{r,\text{max}}$	6e-9 m/s
Water potential at 50% loss of conductivity	p_{50}	-1.75 MPa
Vulnerability shape parameter	c_k	2.95
Soil potential with stomata fully open	ψ_o	-0.65 MPa
Soil potential with stomata fully closed	ψ_c	-2.5 MPa
Medlyn intercept	g_0	100 μmol / m2 / s
Medlyn slope	g_1	6 $kPa^{0.5}$
Soil porosity to 4.64 meters	n	0.42
Soil porosity beyond 4.64 meters	n	0.28
Saturated soil hydraulic conductivity	$k_{\text{s,max}}$	3e-5 m/s
Saturated soil matric potential	ψ_{sat}	461 Pa
Brooks-Corey parameter	b	6

Brazil) and part of the Large-Scale Biosphere-Atmosphere Experiment in the Amazon [Avissar et al., 2002].

1. SMS, with ambient precipitation throughfall (AMB)
2. SMS, with 60% of precipitation throughfall excluded (TFE)
3. PHS, AMB
4. PHS, TFE

All four simulations use the same version of CLM5 (development version r270, www.github.com/ESCOMP/ctsm/releases/tag/clm4_5_18_r270), which features a switch that can toggle between SMS and PHS configurations. Simulations are run offline (uncoupled from an active atmospheric model), spanning from 2001 through 2003, utilizing the satellite phenology (SP) mode of CLM5 in which vegetation state (LAI, canopy height) is prescribed and biogeochemistry is inactive. Six-year spin-up simulations (one each for SMS and PHS)

are used to create initial conditions, repeating the ambient simulation twice. This satisfied steady state soil conditions, with soil matric potential changing by less than 0.2% between the two loops. Descriptions of site characteristics, forcing data, and observational sap flux and soil moisture, can be found in Fisher et al. [2007] and Fisher et al. [2008].

1.3.1 Parameter values and throughfall exclusion

Parameter values concerning vegetation hydrodynamics are presented in Table 1. All other parameters use the default values associated with the r270 version of CLM5. Informed by parameter values reported in Fisher et al. [2008], we tuned soil hydraulic parameters and the throughfall exclusion rate, to improve simulated soil moisture relative to observations (Figure S9). An ensemble of simulations was used to tune the parameters for the PHS configuration to reasonably reflect sap flux observations (see Appendix A.1).

1.4 Results

1.4.1 Comparison with observations

We tested two configurations of CLM5 (PHS, SMS) with simulations of the Caxiuanã throughfall exclusion experiment over 2001-2003. We compared modeled transpiration with observations derived from sap flux velocity and modeled soil moisture with observations using TDR sensors (see above for experiment and observation details).

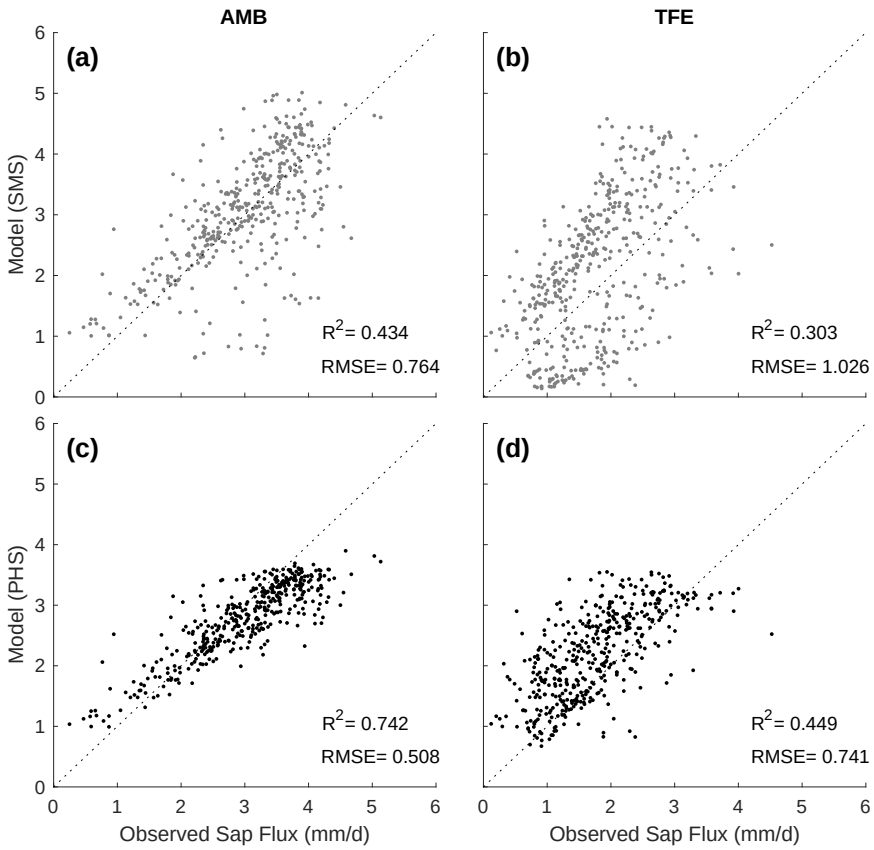

Figure 1.2: Modeled versus observed daily total transpiration. Observations are derived from field observations of sap flux velocity (see Section 1.3). (a,b) SMS configuation, under ambient conditions and 60% TFE. (c,d) PHS configuation, under ambient conditions and 60% TFE.

Transpiration, ambient conditions

Under ambient conditions, PHS reduces error and improves correlation between modeled and observed transpiration (compared to SMS, Figure 1.2a,c). While the two models make a similar number of small errors, SMS commits more errors exceeding 1 mm/day. The absolute value of SMS-OBS transpiration (Figure S3g) exceeds 1 mm/d in 67 of 414 days with available observations, as compared to just 23 with PHS. And while PHS error is limited to a maximum of 1.6 mm/d, SMS error exceeds 2 mm/d twelve times. These twelve SMS errors all result from underestimating transpiration relative to observations, coinciding with

dry soils, which is discussed further in Section 1.5.4.

While PHS offers improvements in modeled transpiration as measured by RMSE and correlation, the ambient simulation seems to underestimate transpiration variability, with a standard deviation of daily transpiration of 0.61 mm/d compared to 0.87 mm/d in the observations (with SMS, the standard deviation is 0.97 mm/d). As such, PHS features a low bias for high transpiration values and a high bias for low transpiration values (Figure 1.2c). The difference in modeled transpiration between PHS and SMS derives from divergent water stress dynamics, which are discussed in Section 1.5.2.

Transpiration, TFE

PHS performs better than SMS at reproducing transpiration observations under TFE (Figure 1.2b,d), featuring a higher R^2 (0.45 vs. 0.3) and lower RMSE (0.74 vs. 1.03 mm/d). However, both implementations show degraded results under TFE as compared to ambient rainfall conditions. Simulating the wet season under TFE (February-March-April) is prone to high transpiration biases in both models, where, in the observations, transpiration is reduced 32% by TFE, as compared to modeled reductions of only 1.6 and 4% for PHS and SMS, respectively. This may indicate that the models' sensitivity to soil potential declines are underestimated, or that water drains from the root zone more quickly after precipitation events than we represent with the soil hydraulic parameters (Figure 1.3b,d). Difficulty reproducing the effect of TFE (and the influence of soil moisture on leaf gas exchange) at Caxiuanã has precedent in the literature [Restrepo-Coupe et al., 2017, Powell et al., 2013].

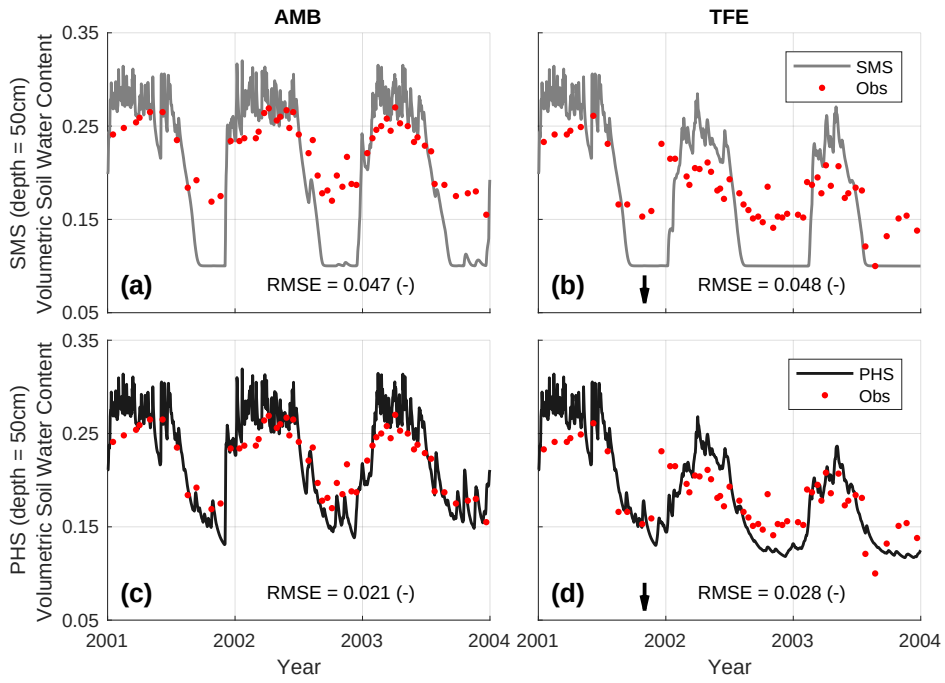

Figure 1.3: Volumetric soil water content (-) over time under ambient and TFE conditions at a depth of 50cm. (a/b) SMS (c/d) PHS. Arrows indicate start of TFE. Supplementary Figure S11 plots 7 other soil depths. In the SMS configuration, soil moisture can tend to 'stick' at water content of 0.1 during the dry season, which corresponds to ψ_{soil}=-2.5MPa and is the value of the SMS soil wilting parameter, ψ_c.

Soil moisture

The second source of observations for model evaluation is volumetric soil moisture. These data are used to evaluate the parameterization of root water uptake. Modeled soil moisture values (at a depth of 50 cm) are comparable between model configurations during the wet season (February-March-April) under ambient conditions, both yielding averages of 28% (Figure 1.3a,c). With excess rainfall, soil moisture is largely determined by the soil field capacity and saturated conductivity, which are the same in both model configurations. With water shortfalls, the root water uptake parameterizations drive the soil moisture dynamics, and the models diverge, as SMS consistently generates lower soil moisture values (than PHS)

within the first meter of the soil column (Figure 1.3, Figure S11). Soil moisture averages to 10% during the dry season (September-October-November, ambient case, depth=50cm) with SMS, as compared to 16% with PHS. PHS better comports with observations, reducing RMSE by 57% relative to SMS (Figure 1.3a,c).

We highlight the soil moisture at 50 cm depth, but similar patterns are observed throughout the first meter of the soil column (Figure S11). The 50-cm depth emphasizes the effect of modeled root water uptake, because it features higher root fraction than the deeper soil layers (Figure S1), but avoids the high frequency dynamics of the top soil layer from soil evaporation and precipitation events that do not relate to differences between PHS and SMS. Under TFE, SMS minimum soil moisture is again 10%, but holds there for a longer duration (Figure 1.3). Contrastingly, PHS achieves lower dry season soil moisture values under TFE as compared to ambient conditions. PHS better comports with observations, reducing RMSE by 42% relative to SMS (Figure 1.3a,c), however both models seem to feature a high bias in soil moisture in the root-zone (under TFE) during the wet season (Figure 1.3, Figure S11).

1.4.2 Vegetation water potential

PHS updates both the water stress and root water uptake parameterizations based on modeling vegetation water potential. Leaf water potential features a pronounced diurnal cycle, reaching -1.65 MPa at midday (Figure 1.4a). Most of the midday pressure drop occurs between ψ_{root} and ψ_{stem} (Δ=-1.47 MPa), representing the root collar and upper stem, respectively. Stem, shade, and leaf curves are all roughly equal, resulting in overlapping lines

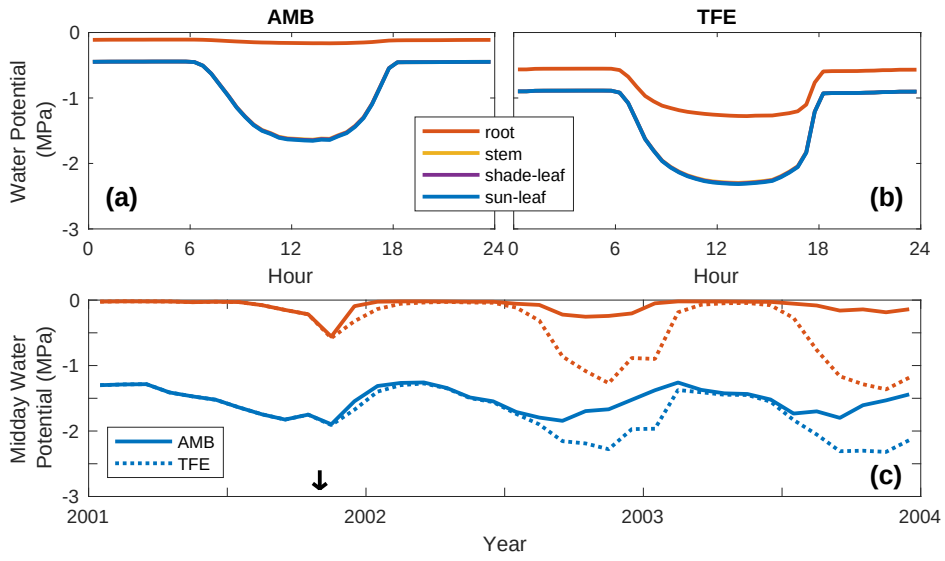

Figure 1.4: (a,b) 2003 dry season (September-October-November) diurnal mean of modeled vegetation water potential under ambient and TFE conditions. Curves are drawn for sunlit leaf, shaded leaf, stem, and root water potentials, with the latter three overlapping. (c) Monthly mean midday (12h-14h) vegetation water potential under ambient (solid line) and TFE (dotted line) conditions. Here curves are drawn only for sunlit leaf and root water potential. The arrow indicates the start of TFE.

in Figure 1.4a, relating to high stem-to-leaf conductance from the parameter values used in this experiment. Stem-to-leaf conductance does not drive leaf water potential in the current parameterization of the model, but may be important to investigate further, given the reported dynamics of leaf conductance [Simonin et al., 2015].

Under TFE, model midday leaf water potential decreases to -2.31 MPa (Figure 1.4b). This change derives from a decrease in predawn root water potential (lower soil moisture) and in the drop in root water potential between predawn and midday (due to reduced soil-to-root conductance). This comports with previous evidence that seasonal changes in hydraulic resistance are larger belowground [Fisher et al., 2006]. Despite reduced stem conductance, the pressure drop from root-to-stem acts in the opposite direction, reduced in magnitude to -1.02 MPa (from -1.47 MPa), following from 54% reductions in transpiration. In this way,

stomatal regulation serves to mitigate the drop in leaf water potential due to soil drying and reduced hydraulic conductance.

Midday leaf water potential features a seasonal cycle, with lower values during the dry season (Figure 1.4c). Under ambient conditions, modeled root water potential values comport well with wet season observations in Fisher et al. [2006], but are less negative than dry season observations. Modeled leaf water potential values under ambient conditions are less negative than field observations (Fisher et al. [2006] report average ψ_{leaf} of -1.71 MPa during the wet season and -2.47 MPa during the dry season), but are within the range of observations. The parameter values used here may underestimate isohydricity (which would be reflected by minimal leaf water potential drop during drought) in response to TFE, given that observations showed no significant difference between ambient and TFE leaf water potential [Fisher et al., 2006].

1.4.3 Stress dynamics

Modeling vegetation water potential enables a diurnal mode of variability in vegetation water stress. While the SMS stress factor has minimal diurnal variability, PHS features increased stress at midday (Figure 1.5a,b), corresponding to the drop in leaf water potential induced by increasing demand for transpiration (Figure 1.4b,c). Average midday stress values are comparable between the two model configurations during the 2003 dry season (Figure 1.5), but PHS achieves more photosynthesis over the course of the average dry-season day (Figure S4), due to lower stress in the mornings and afternoons.

The SMS stress factor lacks diurnal variability, because it is based on average root-zone

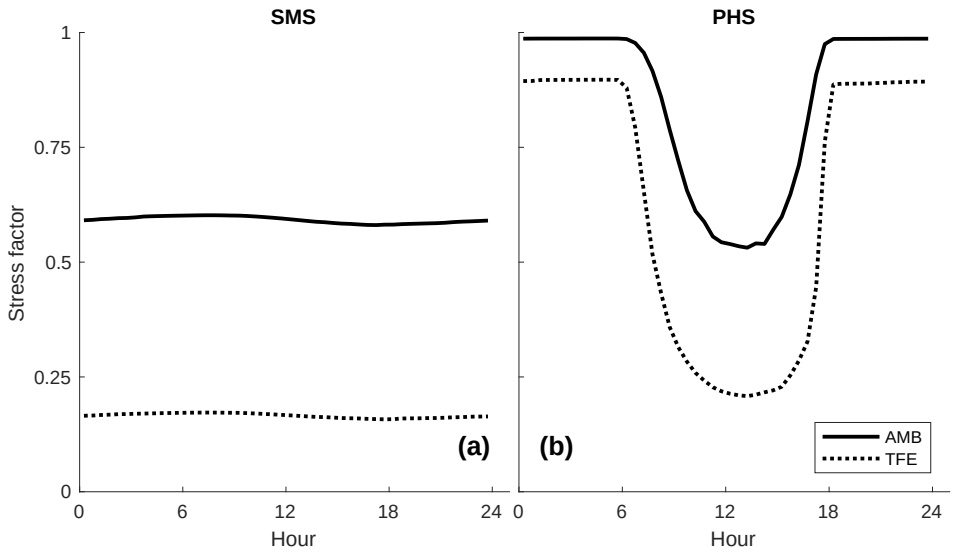

Figure 1.5: 2003 dry season (SON) diurnal mean water stress function for (a) SMS, and (b) PHS. Note that the water stress factor equals 1 when there is no stress and 0 when fully stressed.

soil matric potential (Equation 1.3), which evolves over longer timescales. PHS utilizes leaf water potential to calculate stress (Equation 1.9), which responds to both water supply and transpiration demand. As such, the PHS stress factor responds to both soil moisture and VPD, while SMS responds only to soil moisture (Figure 1.6). Under ambient conditions, SMS features significant stress associated with declining soil water status, but PHS stress is primarily demand-driven, with less impact from soil moisture (Figure 1.6a,c). With TFE, stress increases in both model configurations, and the effect of soil moisture on PHS stress increases markedly (Figure 1.6d).

1.4.4 Gross primary productivity (GPP)

The two stress parameterizations feature differing seasonal cycles of GPP, with PHS experiencing less seasonal variability in stress (Figure 1.7a-d). Under ambient conditions, SMS predicts little to no stress (f_w=1) during the wetter months (January through July). Mean-

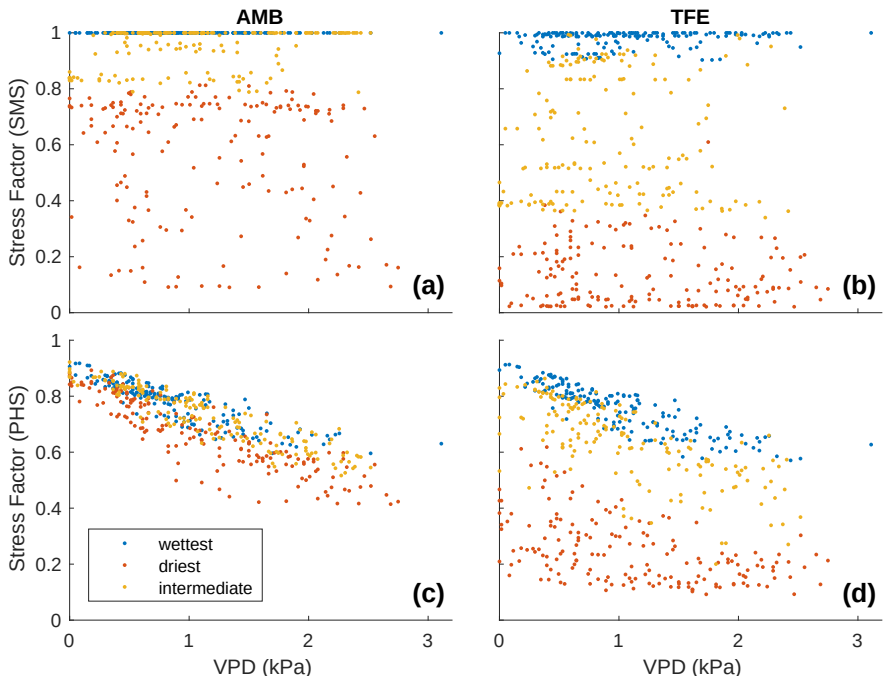

Figure 1.6: Water stress factor versus vapor pressure deficit (2002-2003), constrained to timesteps with downwelling shortwave radiation between 400 and 425 W/m2 (n=515). Radiation is controlled to highlight the relationship with VPD, the reverse (controlling for VPD) is shown in Supplementary Figure S6. For SMS (a,b), data are subdivided based on average soil matric potential, weighted by root fraction. For PHS (c,d), data are subdivided based on predawn (5h) root water potential. Blue dots represent the wettest tercile, yellow dots represent the intermediate tercile, and red dots represent the driest tercile (values defining each tercile are in Table 1.2). PHS utilizes leaf water potential as the basis for its water stress factor, which introduces a dependence on transpiration demand.

while PHS models significant stress, with highly variable f_w, ranging as low as 0.5. Despite abundant soil water, PHS still imposes stress, due to high transpiration demand when VPD and downwelling solar radiation are high. This results in lower wet season GPP and lower GPP variability than with SMS (Figure 1.7e,g). Contrastingly, SMS imposes more stress than PHS during the dry season (Figure 1.7b,d), resulting in lower dry season GPP. Observations show that GPP increases at Caxiuanã during the dry season [Restrepo-Coupe et al., 2017], suggesting that both model configurations, but especially SMS, may overestimate dry season water stress under ambient conditions.

Table 1.2: Root-zone soil potential[a] (MPa) terciles. The two cut-points are used to divide the points in each subplot of Figure 1.6 into three groups, based on root-zone soil moisture.

Simulation	T1	T2
SMS, Ambient	-0.01	-0.54
SMS, TFE	-0.29	-1.74
PHS, Ambient	-0.01	-0.05
PHS, TFE	-0.05	-0.33

[a]SMS values correspond to daily mean root-fraction weighted soil potential. PHS values correspond to predawn root water potential.

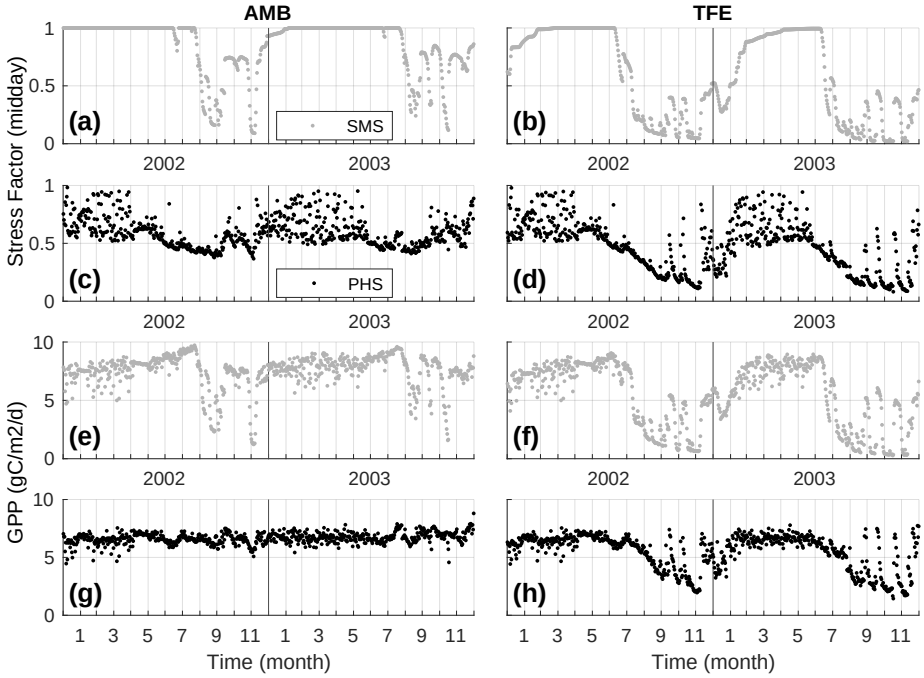

Figure 1.7: (a-d) Daily stress factor (midday, averaged over 12h-14h) and (e-h) GPP (daily total) over 2002-2003 under ambient (left column) and TFE (right column) conditions. Output from the SMS configuration (a,b,e,f) are plotted with gray color, while output from the PHS configuration (c,d,g,h) are plotted in black.

The modeled effect of TFE is relatively small during the wet season, with modeled reductions in GPP of 1.3 and 3.8% for PHS and SMS, respectively. Based on transpiration observations, both configurations likely underestimate the TFE effect during the wet season (discussed further in Section 1.5.2). SMS imposes more dry season stress, resulting in a 63%

reduction of GPP due to TFE, compared to 44% with PHS. Comparing dry season stress to the wet season, and TFE conditions to ambient, precipitation shortfalls (and the associate reductions in soil moisture) lead to less added stress under PHS as compared to SMS. However, PHS experiences more stress overall, due to the effects of xylem tension imposed by the gradient of water potential from soil-to-leaf (discussed further in Section 1.5.2). The sensitivity of leaf gas exchange to transpiration demand is subject to the representation of hydraulic conductance in PHS, which requires caveats related to parametric uncertainty and hydraulic simplifications (see Section 1.2.5).

1.4.5 Root water uptake (RWU)

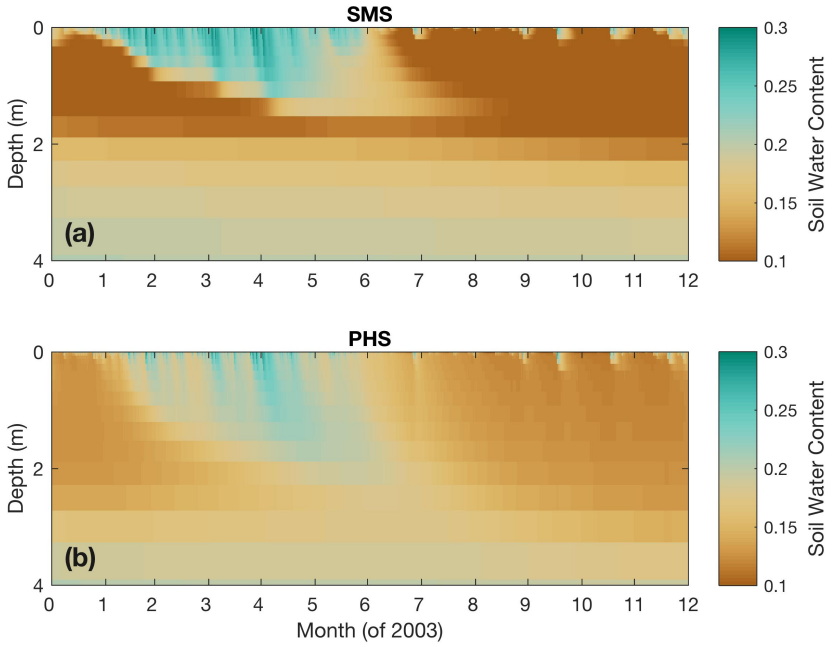

Figure 1.8: Vertical profile of soil water content (by volume) over 2003 under 60% throughfall exclusion, for (a) SMS, and (b) PHS. Soil water content under ambient conditions is shown in Supplementary Figure S9. PHS spreads the vegetation transpiration sink over a larger vertical extent, which prevents the very low soil moisture values observed in SMS.

In addition to updating water stress, PHS implements updated RWU, consistent with hydraulic theory [Cai et al., 2018, Warren et al., 2015]. The parameterization of RWU affects the vertical distribution of soil water (Figure 1.8, Figure S9), as SMS tends to achieve drier upper soil layers, whereas PHS spreads the drying effects of transpiration over a larger vertical extent. As described in Section 1.4.1 (Figure 1.3), this yields a dry bias relative to soil moisture observations in the root-zone for SMS (within the dry season).

RWU, within a given soil layer, is the product of hydraulic conductance ($k_{s,r}$) for water flow and the gradient ($\Delta\psi$) in water potential from $\psi_{\text{soil,i}}$ to ψ_{root} (see Section 1.2.5). With PHS, reductions in RWU with drying are imposed by declining $k_{s,r}$, which decreases by almost 3 orders of magnitude as soil potential declines from 0 to -1 MPa (Soil Layer 5, Figure S7). This derives primarily from the exponential dynamics of soil conductivity [Brooks and Corey, 1964]. $\Delta\psi$ tends to increase with drying (due to dynamic ψ_{root}), partially mitigating the reductions to RWU imposed by $k_{s,r}$. With SMS, the opposite is true: reductions in RWU are imposed by declining $\Delta\psi$ and are (to a small extent) mitigated by increases in the (implied) conductance. RWU (within a given soil layer) is more sensitive to soil potential with PHS (Figure S10), which prevents soil potential from getting much lower than -1 MPa, as compared to values as low as -2.5MPa under SMS.

While RWU within a given soil layer is more sensitive to soil potential with PHS, transpiration overall is less sensitive to shortfalls in precipitation associated with dry season onset and TFE (as compared to SMS, Figure S3). This is because, within PHS, there is more flexibility to compensate for dry layers by switching the RWU to moist layers. As such, PHS can compensate for its sensitivity to soil potential by spreading the drying associated with the transpiration sink over a larger vertical extent (Figure 1.8). Following from this, with

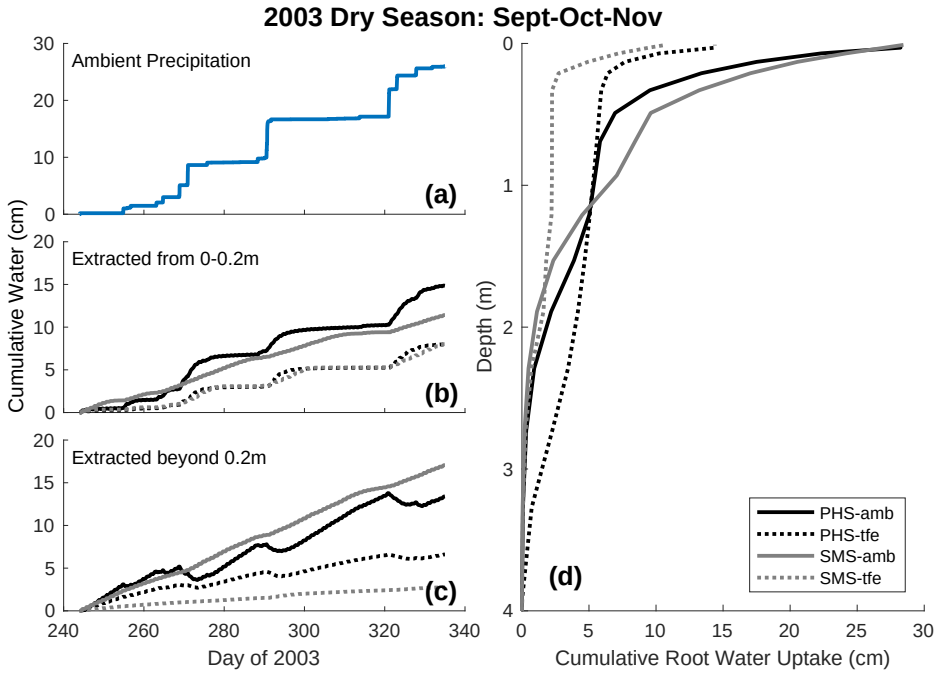

Figure 1.9: 2003 dry season (SON) cumulative root water uptake and precipitation. (a) Cumulative precipitation over time under ambient conditions (b,c) Cumulative water uptake over time from above and below 0.2m, respectively. (d) Cumulative root water uptake over the soil column (accumulating from depth). An equivalent plot for the wet season is shown in Supplementary Figure S5. The new root water uptake parameterization allows PHS to maintain more transpiration under TFE by utilizing more deep soil water.

PHS, dry season transpiration is less sensitive to TFE, due to increased RWU from below 2 meters in depth (Figure 1.9d). The shifting of water extraction based on water availability is also present under ambient conditions, as PHS shifts RWU from near-surface (0-0.2m depth) to the deeper soil layers (beyond 0.2m) during drydowns (Figure 1.9a-c).

Lastly, PHS eschews constraints on RWU imposed by SMS (Equation 1.7), that sets extraction to zero if $\psi_{\text{soil,i}}$ is drier than ψ_c and to a maximal value when $\psi_{\text{soil,i}}$ is wetter than ψ_o (SMS parameters for soil potential with stomates fully closed and open, respectively). Hydraulic theory does not support either constraint. Furthermore, the non-linearity of RWU at ψ_c (Figure S7), creates a situation where dry soil layers tend to stick at $\psi_{\text{soil,i}}=\psi_c$ (Figure

1.3). Likewise, the constraint at ψ_c precludes the representation of hydraulic redistribution.

1.4.6 Hydraulic redistribution (HR)

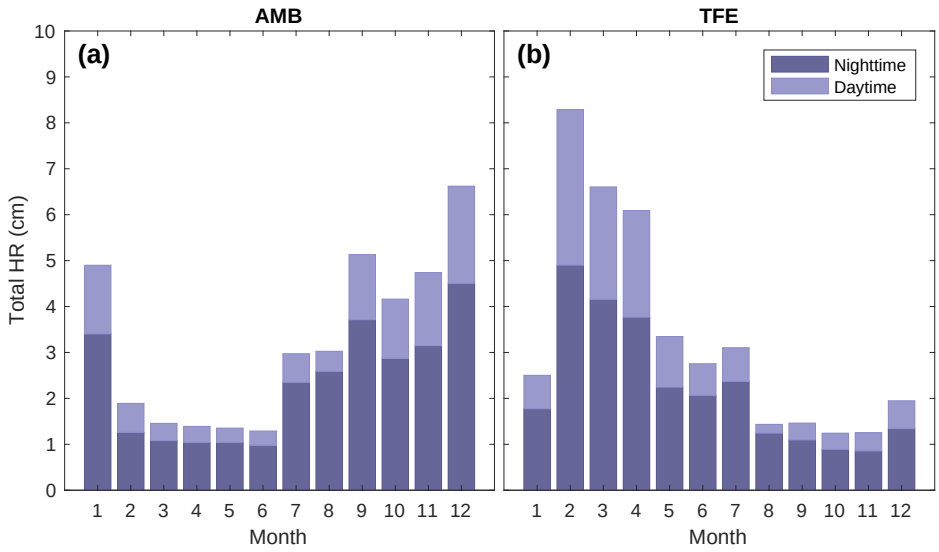

Figure 1.10: Total hydraulic redistribution (cm) by month across 2003. For (a) ambient throughfall conditions, and (b) 60% throughfall exclusion. Darker shading shows portion of HR at night [6pm,6am), lighter shading shows portion of HR during the day [6am,6pm). Total HR refers to the sum of all negative root water uptake flows, whenever water is deposited by roots into a given soil layer (instead of being extracted).

SMS precludes HR (contrary to PHS) setting root water uptake to zero when reversed gradients in water potential occur ($\psi_{\text{soil,i}} \psi_c$). With PHS, HR totals to 38.9 cm under ambient conditions and 40.0 cm under TFE over the course of 2003, with the majority (28.0, 26.7 cm) of this HR occurring at night (Figure 1.10), in line with established theory [Jackson et al., 2000, Lee et al., 2005] and observations [Oliveira et al., 2005, Burgess et al., 1998]. HR occurs in both directions (Figure S8), but is predominately downwards (AMB: 30.7cm, TFE: 33.8cm). The amount of HR is difficult to evaluate due to scarce observations. The simplicity of the hydraulic representation may lead to overestimating HR, which is discussed

further in Section 1.5.3.

1.4.7 Soil moisture effect on transpiration

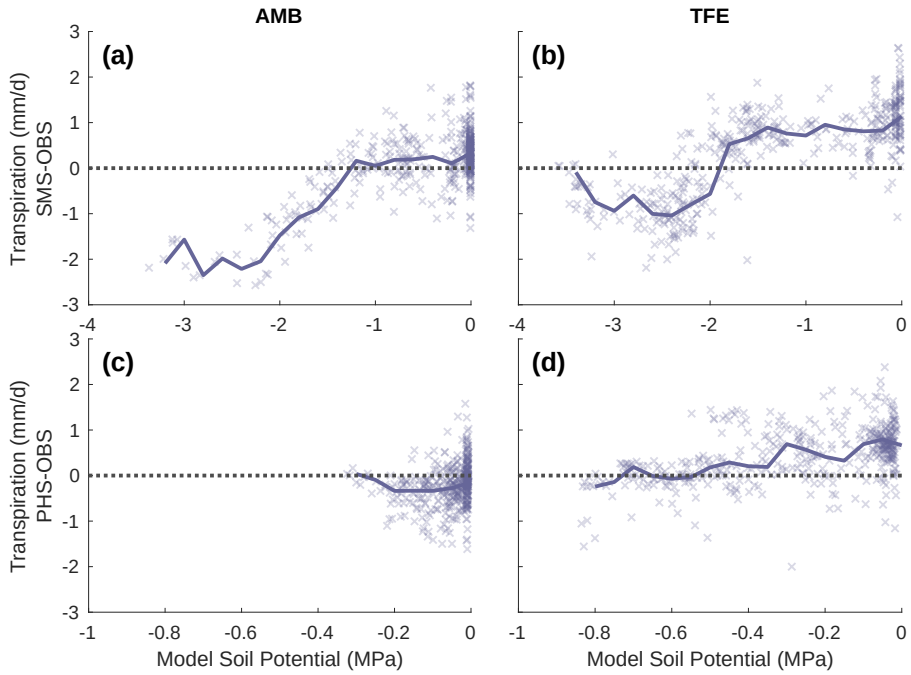

Figure 1.11: Difference between modeled and observed transpiration (mm/d) versus model soil potential (MPa), for (a,b) SMS and (c,d) PHS. Solid lines are drawn at the median, binning points every 0.2MPa for SMS and 0.05 MPa for PHS (note the different soil potential axes). Dotted lines are drawn at zero, where modeled and observed transpiration are in agreement. The two models use different root water uptake paradigms, from which we define different operators for column effective soil potential. For SMS we average over the soil column weighted by root fraction and over time (daily mean). For PHS we use predawn (5h) root water potential. Based on available observations, n = 414/436 days under ambient/TFE conditions.

Model soil potential shows limited relationship to sap flux observations under ambient conditions (Figure S12b,f), which is indicative of limited soil moisture stress. However, in the SMS configuration, modeled transpiration decreases strongly with more negative soil potential (Figure S12a), biasing the model relative to observations (Fig 1.11a).

Sap flux observations under TFE show a stronger relationship with soil potential especially with PHS (Figure S12h,d). With SMS, the modeled attenuation of transpiration with soil potential again seems to bias modeled transpiration (Fig 1.11b). The two PHS simulations feature less structure in transpiration bias vs. soil potential and less bias overall (Fig 1.11c,d).

1.5 Discussion

1.5.1 Can modeling vegetation water potential improve the CLM?

In this study, we have implemented plant hydraulic theory within CLM5, using dynamic vegetation water potential to modulate leaf gas exchange and root water uptake. Darcy's Law, which is already used to model soil water movement in the CLM, offers a useful approximation for vegetation water fluxes [Sperry et al., 1998]. PHS installs a model for predicting vegetation water potential by extending Darcy's Law through the vegetation substrate (Figure 1.1), creating four new water potential prognostic variables (ψ_{root}, ψ_{stem}, $\psi_{\text{shade-leaf}}$, and $\psi_{\text{sun-leaf}}$). The model is able to capture expected diurnal and seasonal dynamics of vegetation water potential, with lower values within the stem and leaves at midday and during the dry season (Figure 1.4). PHS uses the new vegetation water potential variables to advance the physical basis for representing the SPAC, particularly with regard to modeling vegetation water stress and root water uptake.

To demonstrate the new model dynamics, we utilized a site-level experiment testing

PHS by simulating the Caxiuanã throughfall exclusion experiment [Fisher et al., 2007]. We found that PHS improves output for both transpiration and soil moisture relative to observations as compared to the control model (see Section 1.4.1, Figures 1.2,1.3). While this is encouraging, especially given the soil moisture dependence of the SMS bias (see Section 1.4.7), the improvement is specific to the site and experiment described herein, and model skill will need to be re-evaluated in a broader context. Instead, the value of opting for a single site (in lieu of global simulations) resides in the opportunity to perform detailed analyses to elucidate the new model dynamics in order to complement this first description of PHS.

1.5.2 Stomatal conductance: soil moisture stress vs. xylem tension stress

The first of these analyses is of the response of stomatal conductance stress to environmental factors, namely: soil moisture, vapor pressure deficit, and solar radiation. The Medlyn stomatal conductance model, as implemented in the CLM, requires a notion of water stress to attenuate stomatal conductance in order to capture the effects of diminishing water supply, with various relevant implementations described in the literature (see Section 1.2.3). We tested two such approaches, which alternatively base stress on either soil water potential (SMS) or leaf water potential (PHS). The two configurations feature significantly different stress dynamics on both diurnal and seasonal timescales (Figures 1.5,1.7).

Leaf water potential is (in simplified terms) the sum of soil water potential and the gradient of water potential from soil-to-leaf ($\psi_l = \psi_s + \Delta\psi$). Therefore using ψ_l as the

driver of water stress preserves a relationship between stress and soil potential, but now also represents the effect of increasing demand for transpiration (reflected by increases in $\Delta\psi$). PHS offers a mechanistic approach to water stress, utilizing a physical justification that interprets water stress as the result of increasing xylem tension, which has previously been used as a primary [Sperry et al., 2017] or contributing [Novick et al., 2016b] factor to stomatal regulation. In the model, vegetation will (according to the specific hydraulic parameter values) limit transpiration in order to avoid overly negative leaf water potential values, which are associated with cavitation and embolism [Tyree and Sperry, 1989]. As a result, PHS stress responds to changing soil moisture, but unlike SMS, also responds to VPD and downwelling solar radiation (Figure 1.6), which modulate transpiration demand. This imparts a diurnal pattern to PHS stress, with higher stress around midday, whereas with SMS, stress is relatively constant throughout the day (Figure 1.5). The PHS stress formulation will impart an increased sensitivity of GPP to rising VPD under climate change, which could lead to a diminished terrestrial carbon sink relative to SMS projections.

Soil water potential approaches (as in SMS) lack a straightforward physical basis, but rather empirically relate stomatal conductance and/or photosynthetic parameters with soil potential (or soil moisture). However, in the case of SMS, the empirical relationship is very difficult to constrain, due to scarce observations of the stress driver, root-fraction-weighted soil potential. As a result, soil moisture stress functions have been shown to contribute significant uncertainty to the carbon cycle in Earth System Models [Trugman et al., 2018]. Leaf water potential, on the other hand, is more easily measured in situ [Boyer, 1967] and has been shown to correlate with remote sensing products [Momen et al., 2017], offering better observational constraints for PHS. Likewise, incorporating plant hydraulics may allow

for improved model representation of tree mortality [McDowell et al., 2018]. The PHS formulation represents an incremental approach to coupling stomatal conductance to leaf water potential, inheriting the established CLM stomatal conductance model [Franks et al., 2018], while adapting the water stress factor to depend on leaf water potential. This could be refined in future versions of PHS, incorporating recent work that directly incorporates leaf water potential within the stomatal optimization [Wolf et al., 2016, Sperry et al., 2017, Anderegg et al., 2018b].

1.5.3 Structural improvements in modeling root water uptake

Dynamic vegetation water potential

PHS introduces dynamic vegetation water potential (Figure 1.4), for the first time, into the default configuration of the CLM. Seasonally and diurnally dynamic leaf water potentials are observed in the field [Fisher et al., 2006], adjusting to variations in soil water supply and transpiration demand. Dynamism in the gradient of water potential from soil-to-leaf, according to the Darcy's Law approximation of vegetation water fluxes, drives RWU. This is especially important for partitioning the transpiration sink among soil layers with varying soil potential states [Jarvis, 2011]. A mechanistic representation of RWU with dynamic vegetation water potential allows for modeling a range of water use strategies, and/or testing hypotheses regarding such strategies on the ESM scale. One example is testing the effects of increasing carbon allocation to root biomass, which was not well-represented in previous versions of the CLM, because water availability depended on relative root fraction and would not respond to increase in absolute biomass. Another example is testing the effects

of iso/anisohydry, which can be diagnosed from remote sensing observations [Konings and Gentine, 2017], on leaf gas exchange and drought vulnerability. The spectrum of isohydric to anisohydric behavior, corresponding to highly regulated versus relatively unregulated leaf water potential, cannot be represented in previous versions of the model that do not model leaf water potential. Likewise, variations in hydraulic safety margin, which have been shown to correlate with drought sensitivity [Anderegg et al., 2018], can now be represented in the model due to prognostic leaf water potential.

Mechanistic hydraulic conductance, with response to drying

Likewise, PHS implements mechanistic hydraulic conductance through the SPAC, reflecting declines in conductance associated with decreasing water potential in both plant vessels and soil substrate [Tyree and Sperry, 1989]. Hydraulic theory describes soil conductance as featuring an exponential relationship with soil potential [Brooks and Corey, 1964], ranging three orders of magnitude over the range of soil potential observed in our simulations (Figure S7). This shapes the PHS response of RWU to soil drought, and is not captured by the linear loss of RWU exhibited in SMS (between the parameters: ψ_o and ψ_c, Figure S10). As a result, PHS RWU is more sensitive to drying soils, which seems to ameliorate dry biases in soil moisture observed in SMS relative to observations (Figure 1.3). At the same time, the mechanistic approach of PHS better reflects soil-root hydraulic theory [Cai et al., 2018, Warren et al., 2015].

Compensatory RWU

Utilizing a hydraulic approach (with dynamic vegetation water potential and mechanistic hydraulic conductance) enables a more flexible representation of RWU. This includes the ability to model hydraulic redistribution (next Section) and compensatory RWU. Compensatory RWU occurs when soil water extraction switches soil layers to maintain transpiration through precipitation shortfalls. For example, as surface soil layers dry, tap roots can be used to harness reserves of soil water at depth [Oliveira et al., 2005], partially compensating for reduced RWU near the surface. In an SMS-style paradigm, this process is not fully represented.

With identical rooting profiles, PHS extracts 29% of transpiration from beyond 2 meters depth under TFE (during the 2003 dry season) as compared to 13% with SMS. In PHS, as the surface soil layers dry out, conductance decreases rapidly, leading to reduced near-surface RWU. In response, the vegetation 'pulls' harder, as ψ_{root} becomes more negative, creating a larger gradient to the deeper soil layers, yielding increased RWU in those still-moist layers. SMS lacks the flexibility to achieve this type of compensatory RWU, because it models RWU fluxes based on a constant soil wilting potential (ψ_c) and does not explicitly impose a loss of hydraulic conductance as soils dry. As a result, PHS maintains higher levels of transpiration and photosynthesis than SMS during the dry season under both ambient and TFE conditions (Figures S3,1.7). This process may be especially important for modeling evapotranspiration in semi-arid ecosystems [Jarvis, 2011] and in Amazonia, where water contributions of deep roots are often important [Nepstad et al., 1994].

Hydraulic redistribution

PHS simulates substantial HR at our test site, both upwards and downwards (Figure 1.10, Figure S8), which conforms with field observations [Burgess et al., 1998, Oliveira et al., 2005]. Modeled HR is weighted towards downward transfers, moving near-surface water from rain events deeper into the soil column. This may serve to save excess water for when it is most needed, such as during the dry season, and would seem to convey an advantage to deep-rooted individuals, banking water for later use out of reach of shallow-rooted competitors. HR can offer significant water subsidies during dry periods [Jackson et al., 2000] and has been highlighted as an important missing feature in CLM [Lee et al., 2005, Tang et al., 2015]. However, we should note that observations of HR are extremely difficult and rare, and the degree to which HR actually occurs in real-world systems remains unclear. Unequivocal detection of HR involves the observation of reverse flow along transport roots, typically at rates close to the detection threshold of sap flow monitoring systems [Oliveira et al., 2005].

Installing a representation of HR was not a primary objective in the development of PHS. Rather it was the natural consequence of our simplified Darcy's Law implementation for root water uptake. However, it remains to be seen whether HR, as modeled in this implementation, is a feature or a liability. One challenge we faced was that in an initial implementation of PHS, HR seemed to oversupply the top layer of the soil column (spanning 0 to 2 cm below the ground surface) and thus significantly degraded modeled soil evaporation (not shown). To remedy this problem, we set the hydraulic conductance to zero in the uppermost soil layer, disallowing any root water uptake there.

PHS may overestimate HR, given the simplified root system architecture [Bouda and

Saiers, 2017] and the lack of an explicit representation of fine-root cavitation [Kotowska et al., 2015]. In our simulations, HR increases annual total root water uptake by up to 52% relative to transpiration alone (2003, TFE). Other models, similar to the SMS paradigm, disallow HR by constraining root water uptake to be positive [Xu et al., 2016]. We view the PHS implementation of HR into the default versions of the CLM as a 'null' hypothesis for the functioning of this process, and as a platform to allow further refinement from the plant hydraulics community. Isotopologues of water could be used as a tool to further constrain this redistribution in the CLM in the future.

1.5.4 The influence of soil moisture on transpiration

The stress effects of declining soil water potential seems to bias SMS predictions of transpiration relative to sap flux observations (Figure 1.11a,b). Under ambient conditions, soil water shows little relationship with sap flux observations with either model configuration (Figure S12b,f), however SMS modeled transpiration decreases strongly in response to soil drying (Figure S12a). This creates a bias where SMS underestimates transpiration during the drier soil conditions, which is in line with Bonan et al. [2014], where the water stress factor was found to impose too much attenuation of transpiration (in CLM4.5).

With PHS the transpiration bias does not seem to strongly depend on soil potential, while also featuring less bias overall (Figure 1.11c,d). Likewise PHS yields a stronger relationship than SMS between soil potential and sap flux observations during TFE (Figure S12d,h). While improvements in modeled transpiration were expected with PHS (more parameters), it seems promising that the gains are associated with the reduction of a soil moisture induced

bias. This could indicate that PHS better models the relationship between soil potential and water stress or the dynamics of soil potential itself (or a combination thereof). The reduction in bias introduced by the water stress function (especially as it depends on soil potential) represents a major development, given repeated calls to improve vegetation water stress in the next generation of terrestrial biosphere models [Powell et al., 2013, Rogers et al., 2017, Trugman et al., 2018].

1.5.5 Benefits and limitations of PHS

Benefits

1. Advances the physical basis of the CLM
    - Mechanistic xylem tension stress replaces empirical soil moisture stress
    - Root water uptake reflects established hydraulic theory
    - More appropriate response of water availability to root abundance
2. Improves modeled vegetation hydrodynamics
    - Better match to observations of soil moisture and transpiration (higher correlation, lower RMSE)
    - Importantly, the improvements modeling transpiration are achieved by removing a bias associated with soil water status
    - Permits representation of compensatory root water uptake and hydraulic redistribution
    - Avoids excessive soil layer drying observed with SMS
3. Creates an interface to new observational constraints

- Parameters are better represented in trait databases (e.g. k_{max}, p_{50}).
- New state variables modeling vegetation water potential are introduced, which are measured in situ and have been shown to correlate with remote sensing products [Momen et al., 2017].
- And given that vegetation water potential is downstream of soil water potential, this may actually provide an important constraint on root-zone soil moisture.

4. Enables a platform for testing various hydraulics-oriented hypotheses within the ESM context
    - What are the relative contributions to water stress of VPD vs. soil moisture?
    - Does the spectrum of isohydric vs. anisohydric regulation of vegetation water potential explain patterns in the terrestrial carbon and hydrological cycles?
    - Are certain regions of the concatenated hydraulic-parameter / climate space particularly vulnerable to climate change?

Limitations

1. Plant hydraulics are highly simplified
    - Does not model vegetation tissue water storage (capacitance)
    - Loss of conductance (vulnerability) not integrated across vegetation tissue or soil matrix (based on lower terminus)
    - Stem-to-leaf resistance is not fully deployed
    - Simplified root system architecture
    - These simplifications create a null hypothesis for further testing by the hydraulic

community and yield a relatively light-weight model

2. Uncertainty regarding the parameterization of water stress

    - PHS models water stress (f_w) as a sigmoidal function of leaf water potential, which is used to attenuate V_{cmax}
    - Stress attenuation of V_{cmax} was also utilized in CLM4.5/SMS, which allowed for easier comparison between model versions
    - However, significant uncertainty exists in coupling the PHS water stress factor to the Medlyn stomatal conductance model, which could be resolved in future versions by recent work that directly incorporates hydraulic limitations within the stomatal optimization [Wolf et al., 2016, Sperry et al., 2017, Anderegg et al., 2018b].

3. Increased model complexity

    - Can potentially be mitigated by hydraulic trait coordination, improved parameter priors, and observational constraints on vegetation water potential
    - However, the spatial scale of the CLM does not match to the experiments associated with reported parameter values in trait database

4. We do not provide a definitive assessment on model skill

    - We saw broad improvements in modeled transpiration and soil moisture, when comparing PHS to SMS. However, like SMS, PHS overestimates transpiration during the wet season under TFE, effectively underestimating the effect of reduced precipitation throughfall.

- This report is not meant to be a definitive assessment of model skill, as it presents a single site with results specific to experimental setup and parameter values
- The single site framework was utilized to allow for more detailed analysis of the model dynamics to supplement the model description

1.6 Conclusion

The PHS configuration of the CLM5 within the Community Earth System Model (CESM2) is, to our knowledge, the first land-surface model within an ESM with a representation of vegetation water potential running in its default configuration. In this paper, we have described the model implementation, and illustrated a comparison of the model dynamics for a tropical rainforest site subjected to water limitation, given that prediction of rainforest responses to drought is one of the key uncertainties in the ESM predictions [Huntingford et al., 2013].

Overall, the new model behavior differs from the default configuration in ways that are expected, given its structural properties, and in many cases, provides better correspondence with observations than the default structure. Modeling vegetation water potential allows for new parameterizations for the model representations of root water uptake and vegetation water stress, which better conform to established plant hydraulic theory. PHS root water uptake, driven by dynamic vegetation water potential, allows representation of compensatory root water uptake and hydraulic redistribution. As a result, PHS utilizes more of the soil column to buffer precipitation shortfalls, which, in both the ambient and TFE simulations, reduces dry season biases in transpiration and root-zone soil moisture. PHS water stress

requires vegetation to avoid extreme values of leaf water potential, associated with excessive xylem tension and hydraulic failure. This incorporates a dependence of the CLM water stress factor on transpiration demand, which was previously not represented. As a result, photosynthesis is more sensitive to VPD with PHS.

The new model structure will likely have significant implications on climate feedbacks, given the changes in precipitation and VPD sensitivity introduced by PHS. In this paper, however, we have not aimed at undertaking a comprehensive assessment of which model structure performs better, given the substantial parametric uncertainty in both models, and the dependence on numerous other features of the CLM external to water stress representation that contribute to model-observation divergences, such as, in this case, the overestimation of wet season transpiration under TFE.

In lieu of this type of assessment, we propose that the new PHS model structure 1) is more closely aligned with known plant hydraulics theory, 2) provides significantly improved connections to real-world observational data streams (of leaf and stem water status, sap flow, percent loss conductance) and 3) represents known features of ecohydrological function that the control model cannot capture, including hydraulic redistribution, changes in the depth of water uptake with drought stress, plant embolism impacts on gas exchange, and responses of water uptake to changes in root abundance.

Chapter 2

Plant hydraulics increase soil moisture memory and carbon cycle variability in the dry tropics

2.1 Introduction

The terrestrial carbon sink has provided a valuable ecosystem service, removing up to one third of anthropogenic carbon emissions from the atmosphere [Keenan and Williams, 2018]. However the fate of the terrestrial carbon sink under climate change is highly uncertain in Earth System Models (ESMs) and is a major source of disagreement among climate projections [Friedlingstein et al., 2014]. Terrestrial carbon dynamics are complex and highly variable, responding to (among others): temperature, light, precipitation, humidity, and nutrient availability, subject to potentially non-linear and hysteretic behavior [Keenan et al., 2012, Keenan and Williams, 2018]. Understanding how the carbon cycle has responded to past environmental variability can be used as an emergent constraint on the sensitivity of future carbon dynamics to climate change [Cox et al., 2013].

Recent work has demonstrated the large influence of soil moisture on the global carbon cycle across the full spectrum of analytical tools: including ESM simulations [Green et al., 2019], eddy covariance observations [Stocker et al., 2018], and satellite remote sensing retrievals [Humphrey et al., 2018]. Great progress has been made improving model vegeta-

tion processes and soil moisture dynamics using satellite and eddy covariance data [Bonan et al., 2011, Swenson and Lawrence, 2015]. However, models are not able to reproduce observed correlations between global water availability and carbon exchange [Humphrey et al., 2018] or certain aspects of observed vegetation functionality [Lee et al., 2005, Javaux et al., 2013]. In particular, the parameterization of soil moisture stress on photosynthesis has been identified as a major driver of carbon cycle uncertainty in ESMs [Trugman et al., 2018].

ESMs generally use an empirical water stress factor to attenuate transpiration and photosynthesis as a linear function of soil moisture (or soil water potential), averaged over the soil column, weighted by root density [Verhoef and Egea, 2014, Oleson et al., 2013]. Such functions are very difficult to constrain empirically due to the scarcity of root-zone soil moisture measurements [Trugman et al., 2018], and have difficulty reproducing observed drought effects on photosynthesis and transpiration [Powell et al., 2013, Kennedy et al., 2019]. Furthermore, a related formulation is generally used to model root water uptake, partitioning the total transpiration sink among vertically discretized soil layers as a linear function of soil moisture (or soil potential) and root fraction, which contradicts current theory in soil and plant hydraulics [Javaux et al., 2013]. This has led to a call for hydraulically-enabled parameterizations of water stress and root water uptake [Trugman et al., 2018], of which there are multiple examples in the most recent generation of dynamic global vegetation models [Christoffersen et al., 2016, Xu et al., 2016, Kennedy et al., 2019].

We recently installed a simplified plant hydraulics model in the Community Land Model (CLM), the land component of the Community Earth System Model. This hydraulics subcomponent is called Plant Hydraulic Stress (PHS) and is responsible for calculating root water uptake and drought limitations to photosynthesis and transpiration. PHS is the de-

fault configuration for vegetation hydrodynamics for version 5 of CLM, and by extension, version 2 of CESM. This was the first implementation of plant hydraulics within the default version of a coupled ESM to our knowledge. A complete model description is provided in Kennedy et al. [2019], along with point simulations of a tropical forest site subject to precipitation throughfall exclusion, which highlight improvements in transpiration and soil moisture dynamics with PHS.

In this study we extended our analysis of PHS to the global scale, with a $\approx 1^{\circ}$ resolution simulation over the historical period (1850-2013), using CLM5. For comparison we carried out an identical simulation without plant hydraulics, instead swapping in the CLM4.5 parameterizations of soil moisture stress and root water uptake [Oleson et al., 2013]. In particular we were interested in testing the effects of hydraulic root water uptake on soil moisture memory and carbon cycle variability. Our analyses are focused on semi-arid regions, which play an outsized role in the trend and variability of terrestrial carbon exchange [Poulter et al., 2014, Ahlström et al., 2015] and feature longer soil moisture memory [Rahman et al., 2015]. We found that plant hydraulics contribute to longer soil moisture memory and larger interannual variations in photosynthesis in semi-arid regions, which may partly explain why the previous generation of land models tend to underestimate the correlation between water availability and carbon exchange observed in remote sensing data [Humphrey et al., 2018]. The representation of vegetation water dynamics and stress are especially important due to increases in precipitation variability [Pendergrass et al., 2017] and atmospheric dryness [Ficklin and Novick, 2017, Zhou et al., 2019a] expected with climate change.

2.2 Experiment description

We performed two global simulations from 1850-2013 at a resolution of 0.94° latitude by 1.25° longitude. The simulations used the 'offline' mode, with the model forced by a data atmosphere using the GSWP3v1 climate reconstruction (see Bonan et al. [2019] for description of the forcing data and its uncertainty). Likewise we used the satellite phenology mode, which prescribes leaf area index derived from remote sensing observations [Oleson et al., 2013]. Eschewing an interactive atmosphere model and prognostic biogeochemistry omits certain land-atmosphere interactions, but allows for an easier comparison of the first-order effects of implementing plant hydraulics. CLM5 source code is open access, with supporting documentation available at https://escomp.github.io/ctsm-docs.

CLM5 uses PHS as the default representation of vegetation hydrodynamics. Implementations of plant hydraulics and/or hydraulic root water uptake have been tested previously in the CLM showing positive results [Bonan et al., 2014, Lee et al., 2005, Tang et al., 2015], but none were incorporated into the various supported versions of the model (e.g. CLM2-CLM4.5). To test the effects of PHS, we compare with the non-hydraulic hydrodynamics scheme of the previous CLM versions, which we refer to as Soil Moisture Stress (SMS, described further in the next section).

- Case 1 (PHS): running the default CLM5, which features PHS
- Case 2 (SMS): CLM5, but with SMS switched in for PHS

Because many other changes were implemented in the model development process between version 4.5 and 5 of the CLM [Lawrence et al., 2019], we use CLM5 for both simulations. This isolates the effects of plant hydraulics by only swapping in SMS for PHS in Case

2, which can be achieved using a plant hydaulics on/off switch we included in the source code. The two cases utilize identical forcing data and leaf area, and share the same parameterizations for root distribution, soil characteristics, and photosynthetic parameters. They only differ in the calculation of root water uptake and the prognosis of water stress, which serves to attenuate photosynthesis and transpiration. All analyses are based on the last 50 years of the simulations (1964-2013), which allows for soil moisture to spin up from initial conditions. Full details on the various analyses presented here are included in Appendix B.1.

2.3 Model description

A full model description and detailed analyses at a single site comparing PHS and SMS can be found in Kennedy et al. [2019]. Instead, we limit our focus here to the effects of hydraulic root water uptake on soil moisture memory and carbon cycle variability. In this section we describe the SMS and PHS parameterizations of root water uptake, and examine the implications for how soil moisture near the surface is coupled to soil moisture deeper in the soil column.

Root density decreases exponentially with depth [Jackson et al., 1996], such that root water uptake fluxes (per unit depth) are generally higher near the surface with both model configurations. Likewise direct evaporation from the soil surface disproportionately affects the upper soil layers. As a result, exposing a well-watered soil column to drought conditions would cause the upper soil layers to dry at a faster rate, creating a gradient in soil water potential, increasing with depth. Multiple processes act in the direction of restoring equilibrium to the vertical profile of soil water potential, including capillary rise following

Darcy's Law and a shift in the vertical distribution of root water uptake. The size of these restoring fluxes, relative to the size and frequency of perturbations to the surface soil layers, determines the degree of coupling between deep and surface soil moisture.

For example, if the so-called restoring fluxes are very small relative to perturbations in surface soil moisture, the timescale of communication between the surface and deep soil reservoirs may be longer than the period between rain events. As such, the drought perturbation could be erased by infiltration before it is communicated to the deeper soil layers. While the parameterizations of soil evaporation, drainage, and Darcy flow are all identical in the two cases considered here, the models differ in their representations of root water uptake. We therefore expect potential differences in the strength of the coupling between soil moisture in the surface and deep soil layers.

SMS root water uptake (Equation 2.1) utilizes a transpiration partitioning heuristic derived from its empirical soil moisture stress definition. Stress is calculated for each soil layer (e.g. soil layer i) with a piecewise linear function of the layer soil water potential ($\psi_{s,i}$), declining from 1 (unstressed) starting at p_o until it reaches 0 (fully stressed) at p_c, where p_o and p_c are PFT-dependent parameters representing the soil water potentials with stomates fully open and closed, respectively. Root water uptake (q_i) is determined by multiplying the stress term by transpiration (T) and the layer root fraction (r_i), subject to normalization by β_t, the root-weighted average stress across all soil layers, guaranteeing that root water uptake matches transpiration.

SMS root water uptake parameterization:

$$q_i = \frac{T \cdot r_i}{\beta_t} \cdot \frac{\psi_{s,i} - p_c}{p_o - p_c} = \begin{cases} \dfrac{T \cdot r_i}{\beta_t} & \text{for } \psi_{s,i} > p_o \\ \\ 0 & \text{for } \psi_{s,i} < p_c \end{cases} \tag{2.1}$$

With PHS, we used the principles of plant hydraulics and gradient-based flow to represent root water uptake. Root water uptake in a given soil layer is proportional to the gradient between $\psi_{s,i}$ and the root water potential (ψ_{root}) after accounting for the effects of gravity based on the soil layer depth (z_i). That gradient is multiplied by the soil-to-root hydraulic conductance (k_i), which accounts for conductances of the soil matrix and then root vessels in series. Following hydraulic theory, k_i is a function of $\psi_{s,i}$, subject to parameters related to the soil and xylem properties as well as the root distribution. Unlike p_c, ψ_{root} is a dynamic variable, adjusted each timestep to balance root water uptake with transpiration in response to evolving environmental conditions, including soil water potential, vapor pressure deficit, and solar radiation.

PHS root water uptake parameterization:

$$\begin{aligned} q_i &= k_i \left(\psi_{s,i} - \psi_{\text{root}} - \rho g z_i\right) \\ k_i &= f\left(\psi_{s,i}\,, \text{soil properties}\,, \text{root xylem properties}\,, \text{root distribution}\right) \end{aligned} \tag{2.2}$$

To better understand how the vertical distribution of root water uptake responds to drydown, we can examine the ratio of root water uptake occurring at 100 versus 10 cm ($q_{100\text{cm}}/q_{10\text{cm}}$), corresponding to depth and near-surface, respectively. Starting with SMS,

we use Equation 2.1 to generate an expression for $q_{100\text{cm}}/q_{10\text{cm}}$ (Equation 2.3). When looking at the ratio, multiple terms in Equation 2.1 cancel, leaving the ratio of root densities and the gradients between the soil water potentials and the parameter, p_c.

SMS:

$$\frac{q_{100\text{cm}}}{q_{10\text{cm}}} = \frac{r_{100\text{cm}}}{r_{10\text{cm}}} \cdot \frac{\psi_{s,100\text{cm}} - p_c}{\psi_{s,10\text{cm}} - p_c} \tag{2.3}$$

When both soil layers are well-watered ($\psi_s \geq p_o$), $q_{100\text{cm}}/q_{10\text{cm}}$ will equal $r_{100\text{cm}}/r_{10\text{cm}}$. If we assume that $\psi_{s,100\text{cm}}$ remains $\geq p_o$ and plug in some typical parameter values, this equation can be used to gauge how the vertical distribution of root water uptake might shift during a drydown. The CLM5 values for p_o and p_c are -0.5 and -2.5 MPa, respectively, for broadleaf evergreen tropical trees. Should $\psi_{s,10\text{cm}}$ decrease to -1MPa during drought, the ratio in root water uptake would increase to $1.33 r_{100\text{cm}}/r_{10\text{cm}}$, or a 33% increase relative to the well-watered ratio.

The ratio in the PHS configuration looks quite similar (Equation 2.4), except that instead of the ratios of root density, we use the ratios of hydraulic conductance, and instead of measuring gradient relative to ψ_c we use the prognostic ψ_{root}. PHS likewise accounts for the effects of gravity, but these are quite small relative to the expected soil potential dynamics.

PHS:

$$\frac{q_{100\text{cm}}}{q_{10\text{cm}}} = \frac{k_{100\text{cm}}}{k_{10\text{cm}}} \cdot \frac{\psi_{s,100\text{cm}} - \psi_{\text{root}} - 0.01\text{MPa}}{\psi_{s,10\text{cm}} - \psi_{\text{root}} - 0.001\text{MPa}} \tag{2.4}$$

However, whereas $r_{100\text{cm}}/r_{10\text{cm}}$ is static, k is a function of soil potential. Our previous work showed that k can decline more than 2 orders of magnitude from $\psi_s \approx 0$ to -1MPa [Kennedy et al., 2019]. This would be multiplied by the effects due to changes in the gradient ratio, which we would also expect to be larger with PHS, as ψ_{root} tends to be less negative

than p_c. As such we could expect an increase to more than 100 times the well-watered ratio of $q_{100\text{cm}}$ to $q_{10\text{cm}}$. To some extent this will be offset by the fact that the well-watered ratio of $k_{100\text{cm}}/k_{10\text{cm}}$ is smaller than $r_{100\text{cm}}/r_{10\text{cm}}$, due to a larger dependence on root density and the length-scaling of root conductance. Still we expect the net effect to result in increased communication between the deep and shallow soil moisture with PHS, including higher correlations between soil moisture values and stronger coupling coefficients.

2.4 Results and discussion

An important implication of the coupling between surface and deep soil moisture is its influence on photosynthesis. Root zone soil water dynamics are an important driver of photosynthesis, and the parameterization of soil moisture's influence on photosynthesis has been identified as a major driver of carbon cycle uncertainty in Earth System Models [Trugman et al., 2018]. Earth system models may underestimate the relative contribution of low frequency modes of soil moisture variability and generally do not capture the interannual correlation observed between observations of total water storage and the global carbon cycle [Humphrey et al., 2018]. As such, an important benchmark for the effects of PHS is the change in the carbon cycle interannuallly as compared to SMS.

Gross primary productivity (GPP) measures ecosystem photosynthesis, and is a critical driver of the carbon cycle, along with fire and respiration. Globally, GPP interannual variability (IAV, calculated as the standard deviation of annual GPP) is higher with PHS at 4.15 PgC/yr as compared to 3.99 PgC/yr with SMS. The two models are in strongest disagreement in the tropics (Figure 2.1b), with a high density of relatively large values of ΔIAV, both positive and negative. Correspondingly, the interquartile range of ΔIAV is largest in the tropics (Figure 2.1a). IAV tends to be higher with PHS (as compared to SMS) in dry areas of the tropics and lower in wet areas, with an apparent threshold around 1200 mm/yr of mean annual precipitation (Figure 2.1c). But overall, aggregate IAV in the tropics is higher with PHS as compared to SMS (3.09 PgC/yr vs. 2.94 PgC/yr), indicating that the effect in dry areas outweighs that in wet.

Semi-arid regions are of particular interest due to their outsized role in both the trend and

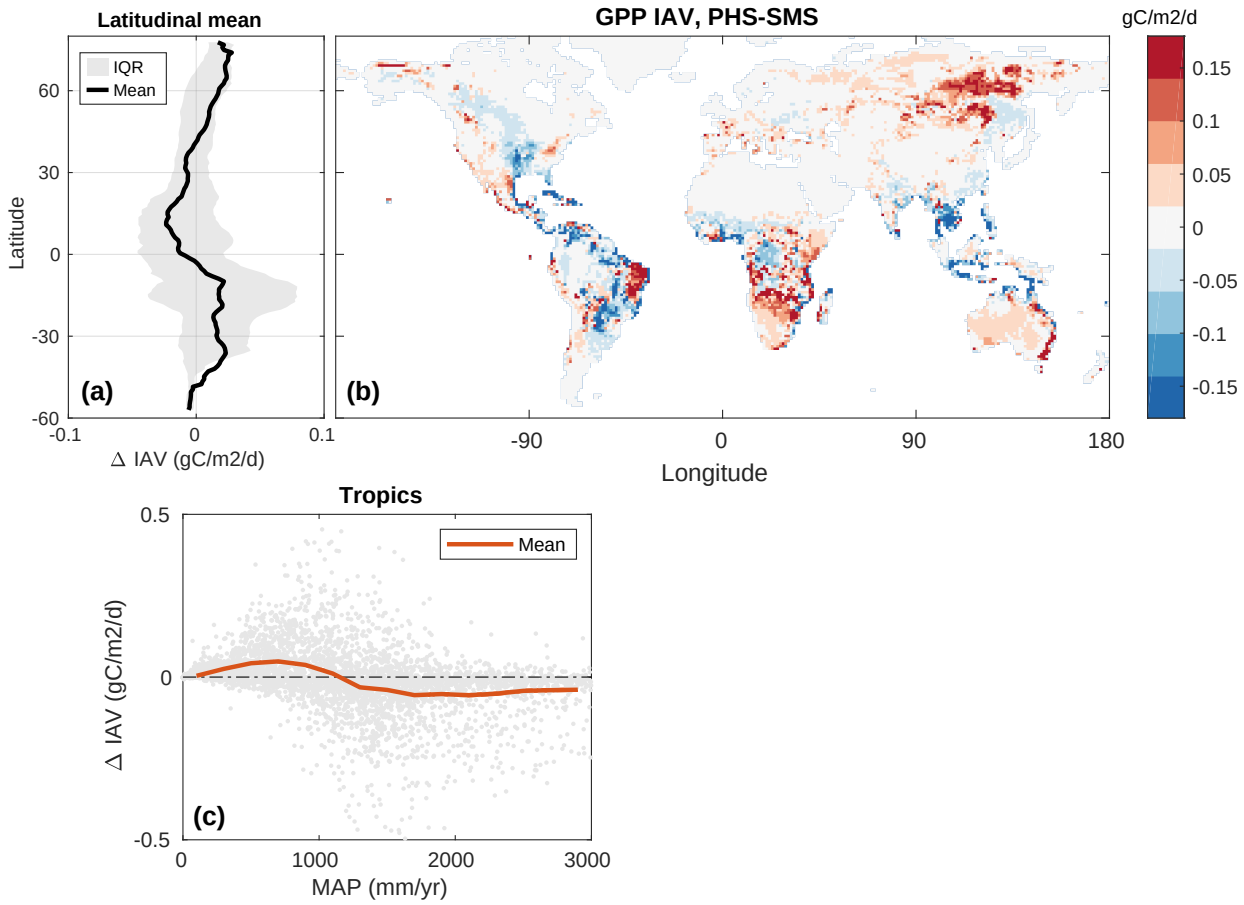

Figure 2.1: The change in the interannual variability of GPP between two configurations of CLM5: PHS, the default mode, which represents plant hydraulics, and SMS, which does not. Top right, the map of ΔIAV across 1964-2013. Top left, the mean and interquartile range compiled latitudinally with a 10°moving window for smoothing. Bottom left, scatter plot of ΔIAV versus mean annual precipitation for gridcells between 30°S and 30°N, along with a binned average drawn in red. Bottom right, the PHS model schematic. In each case ΔIAV is calculated as PHS-SMS, such that positive values indicate more variability with PHS and negative values indicate more variability with SMS.

variability of the land carbon sink [Poulter et al., 2014, Ahlström et al., 2015]. Furthermore, because soil moisture limitations are stronger, and soil moisture memory longer [Rahman et al., 2015], we expect the influence of the PHS root water uptake parameterization to have the largest effect in semi-arid regions. As a result we have focused our analysis in tropical semi-arid regions, using a threshold of annual precipitation less than 1200 mm/yr. To better

understand the difference between the models we focused on gridcells with mean GPP greater than 0.5 $gC/m^2/d$ for subsequent analyses, which filters out areas with negligible vegetation activity. This eliminates 38% of land area in the tropical semi-arid domain (such as the Sahara Desert), but only 1.9% of aggregate GPP. We likewise removed gridcells with mean annual temperature less than 14°C, which eliminates another 3.7% of land area, primarily in the Andes and Himalayas.

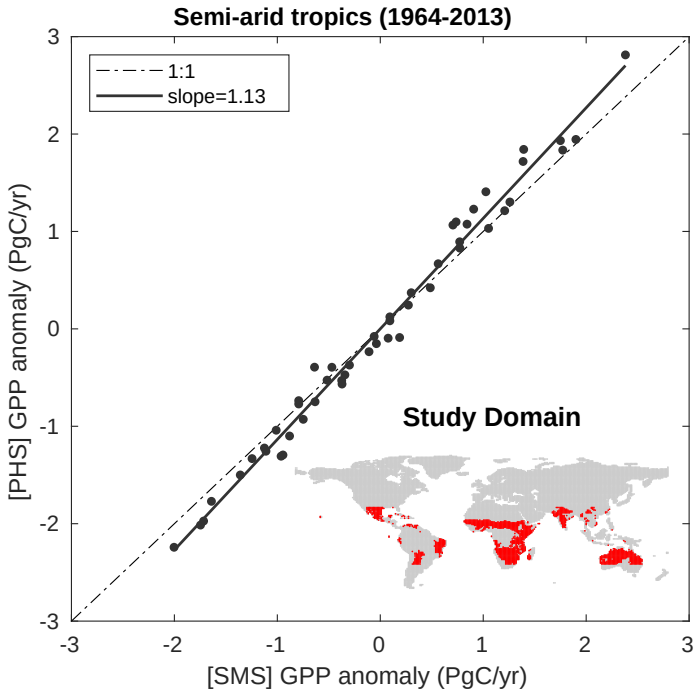

Figure 2.2: Model vs. model comparison of annual GPP anomalies across a semi-arid tropical domain. Anomalies are calculated relative to the respective model means over 1964-2013. The model-model slope does not match the 1:1 line, but rather PHS anomalies are on average 13% larger in magnitude than SMS.

GPP IAV across this domain is 1.21 PgC/yr with PHS and 1.06 PgC/yr with SMS. Interannual anomalies in aggregate GPP are highly correlated between the two models (Figure 2.2, R^2=0.99), but with a slope that is significantly greater than 1 (T=6.8, $p \ll 0.01$). Given the calculated slope of 1.13, interannual GPP anomalies with PHS are on average 13% larger

than with SMS in aggregate across the study domain. This change can be attributed to the vegetation hydrodynamics, because all else was held constant across the two simulations. However it remains to be seen to what extent the increased GPP interannual variability with PHS results from our hypothesis of increased communication between the surface and deep soil layers.

Composite annual average soil water content in the top 10cm of the soil column (SWC10cm) shows a strong relationship with GPP in both models (Figure 2.3). GPP is both larger and more variable with PHS as compared to SMS. However the slopes between GPP and SWC10cm are very similar in both models (Supp Figure B.1). This suggests that PHS GPP is more variable not because it is more sensitive to changes in soil moisture, but instead because it samples a larger range in soil moisture. The range in composite average SWC10cm is 16% larger with PHS than with SMS, which is comparable to the 17% increased range in composite average GPP.

We showed that PHS has more flexibility to switch root water uptake to deep soil layers (see Equations 2.3 and 2.4), whereby deep root water uptake can be used to avoid excessively dry soil moisture near the surface. This is confirmed by the mean seasonal cycles of soil water potential across the study domain (Figure 2.4a). PHS soil water potential at 10cm in depth (near surface) is consistently wetter than with SMS, especially in the drier portion of the year (JAS). Correspondingly, soil water potential at 100cm (deep soil) is drier with PHS and features a more pronounced seasonal cycle. By using more water from the deep soil layers, PHS can limit the amount of drying in the upper layers.

In both models, there is a strong interannual relationship between 10cm and 100cm soil water potential (Figure 2.4b, Supp Figure B.4). In September, the driest month of our

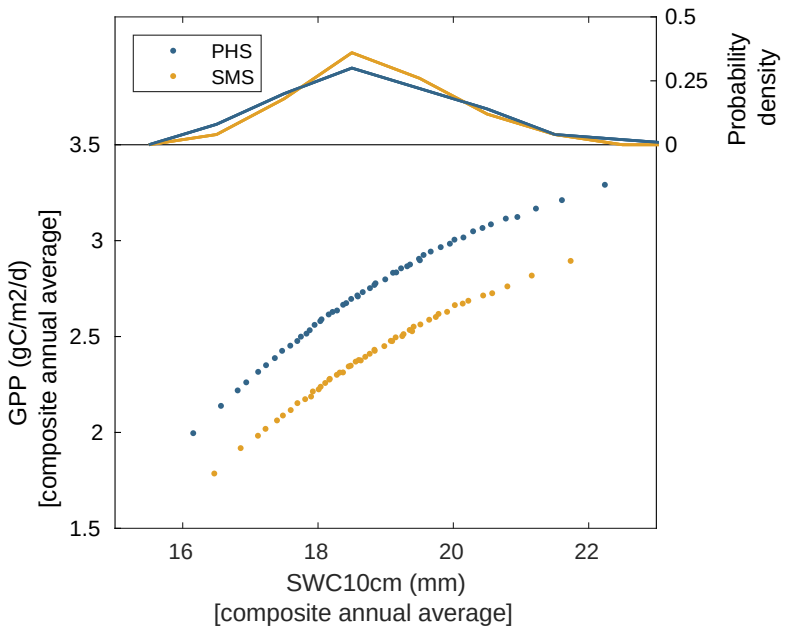

Figure 2.3: The relationship between composite annual average GPP and SWC10cm for PHS and SMS. GPP is uniformly higher with PHS. While the average soil moisture is comparable between the two models (mean SWC10cm = 18.84 and 18.83mm for PHS and SMS, respectively), the composite annual average shows larger variability with PHS, as seen in the probability density subplot. To create the composite average, we first sorted the annual timeseries for each pixel by dryness before aggregating across the study domain. As a result, the leftmost data point does not correspond to a specific calendar year, but rather to the driest year diagnosed separately for each gridcell in the domain. See Appendix B.1 for complete analysis details.

composite timeseries, PHS shows larger interannual ranges in both 10cm and 100cm soil water potentials. Though SMS can achieve just as large a slope in the relationship between the surface and deep soil water potential, it seems to require surface soil potential to reach a drier threshold before the deep soils begin to dry appreciably. As a result, September 10cm soil water potential is wetter than -2MPa in just 4 out of the 50 years with SMS, whereas PHS remains above -2MPa more than half the time (28 out of 50 years).

This is consistent with our discussion of Equations 2.3 and 2.4 (see Section 2.3), which showed that PHS is expected to more rapidly shift root water uptake to deep soil layers

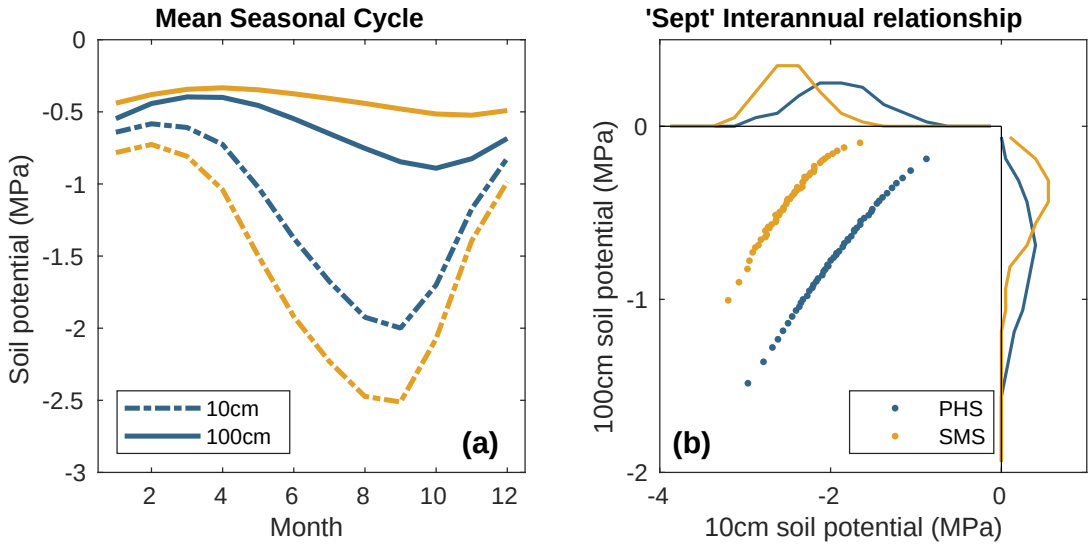

Figure 2.4: Soil potential seasonal cycles at depths of 10 and 100cm (a) and the interannual relationship between them (b). The average seasonal cycles were produced by re-indexing gridcells in the semi-arid domain to align the three month period with the lowest average precipitation. The most common dry season was JJA (Supp Figure B.3), so we plotted the seasonal cycles in (a) to align with that. PHS features a smaller seasonal cycle in 10cm soil potential and a larger seasonal cycle in 100cm soil potential. The composite interannual relationship is shown for 'composite' September (b), along with point density information. Both 10cm and 100cm soil water potential show a larger interannual range with PHS. Interannual relationships for all twelve months are shown in Supp Fig B.4.

during drydown. PHS utilizes well-established soil and plant hydraulic theory to model root water uptake, calculating fluxes proportional to gradients in water potential, subject to variable hydraulic conductances across the soil matrix and through the plant tissue. SMS utilizes an empirical transpiration partitioning heuristic without factoring in the soil or xylem conductances. Soil hydraulic conductance decreases exponentially as a function of soil water potential [Brooks and Corey, 1964], leading PHS to switch to deeper root water extraction earlier than SMS, despite identical root profiles.

Because PHS can more flexibly access deep soil water reserves, it diagnoses less soil moisture stress for each level of surface soil moisture (Figure 2.3). In turn, PHS produces

higher levels of transpiration (by 3.3% on average across the study domain, Supp Figure B.5), requiring more root water uptake overall, which may partially contribute to the larger seasonal range in 100 cm soil moisture. However, as found with GPP, interannual ET shows comparable sensitivity to SWC10cm in PHS and SMS (Supp Figure B.5), such that the increased interannual variability in soil moisture seen in PHS is more likely due to an altered coupling between deep and shallow soil moisture than to the higher levels of transpiration.

The increase in GPP IAV observed with PHS seems to be related to longer timescales of precipitation influence, rather than higher sensitivity to precipitation anomalies. GPP anomalies with PHS are 10% larger than with SMS integrated over the year following large negative precipitation anomalies and 22% larger following large positive anomalies (Figure 2.5b). However the initial response in GPP after both wet and dry anomalies is smaller for PHS than SMS. Instead the increased integrated response is due to longer lags in the response of GPP. Lag periods were likewise longer with PHS in the observed responses of SWC10cm, but to a lesser extent than observed with GPP.

The longer timescales of GPP response likely involve storage and access of water below 10cm. An alternative variable measuring water availability is total water storage (TWS), which tracks total surface and soil column water, comparable to observations from the GRACE satellites. We found a pronounced shift towards higher correlation coefficients in the relationship between surface soil moisture and TWS with PHS as compared to SMS (Figure 2.6a). Likewise GPP shows higher correlations to TWS with PHS than with SMS (Figure 2.6b). Recent work showed that an ensemble of dynamic global vegetation models (TRENDYv3, Sitch et al. [2015]) underestimate the observed correlation between GRACE observations and global net carbon exchange, and likely underweight low frequency modes

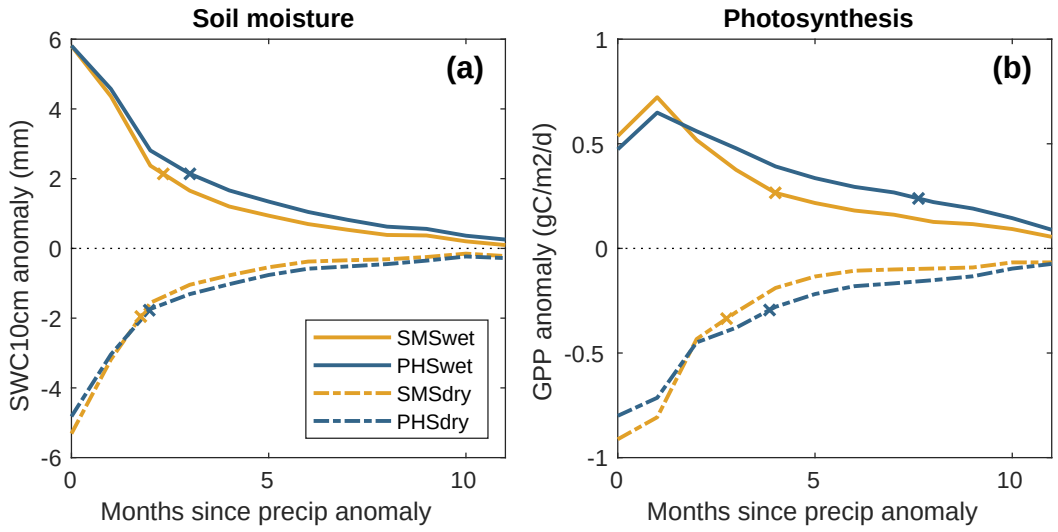

Figure 2.5: The lag periods of surface soil moisture and GPP anomalies after large positive and negative precipitation anomalies. We identified the ten largest positive and negative precipitation anomalies in each gridcell and extracted the timeseries of GPP and SWC10cm anomalies for the following year, composited across the semi-arid tropics regime via a land-area-weighted average. The x symbols are used to denote the e-folding period, marking the time it takes for anomalies to fall to $1/e$ times the maximum anomaly. Lag periods are longer and integrated effects larger for PHS as compared to SMS.

of soil moisture variability [Humphrey et al., 2018]. Our results show that representing plant hydraulics may be an important step in correcting these model biases.

Well-established hydraulic theory finds that soil conductances respond exponentially to soil water potential [Brooks and Corey, 1964]. This requires PHS to switch root water uptake from drying upper soil layers to deeper, still-wet layers much sooner than with SMS, resulting in increased communication between the surface and deep soil moisture. Our results confirm this behavior, with PHS featuring larger ranges in deep soil moisture and increased correlation between SWC10cm and TWS in semi-arid regions. To our knowledge, most (if not all) of the models in the TRENDYv3 intercomparison (including CLM4) utilize non-hydraulic root water uptake parameterizations. This may partly explain why models

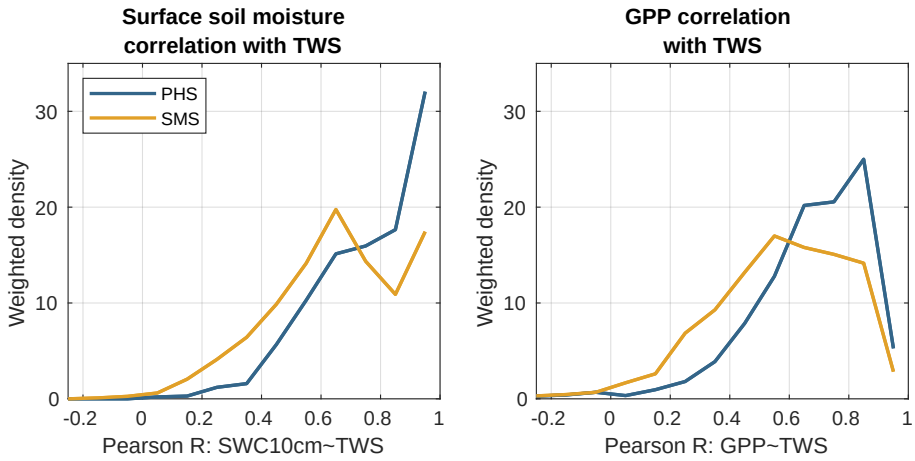

Figure 2.6: Probability distributions of surface soil moisture (left) and GPP (right) with TWS across the dry tropics domain. PHS shifts both distributions to higher correlation values relative to SMS. Correlations were assessed based on annual average values across 1964-2013. Weighted density was plotted for bin widths of 0.1 units. Probability density was weighted by GPP, such that the density value for each bin represents the percentage of total GPP corresponding to the given range in correlation coefficient. For example, with PHS, 25% of the total GPP across dry tropics derives from gridcells where the correlation coefficient between GPP and TWS is between 0.8 and 0.9.

were found to underestimate the correlation between GRACE observations and the global carbon cycle [Humphrey et al., 2018]. Furthermore, results from the CMIP5 intercomparison, which likewise generally lack hydraulic representation, showed that ESMs project further decoupling of surface and total soil moisture in the future, with surface soil moisture drying faster than deep soil moisture under global warming [Berg et al., 2017]. This trend may be reduced or nullified in a hydraulically-enabled model, because the more flexible root water uptake would act to oppose vertical gradients in soil water potential imposed by the increased atmospheric aridity [Ficklin and Novick, 2017, Zhou et al., 2019a] and/or the increased precipitation variability [Pendergrass et al., 2017] expected with further warming.

2.5 Conclusion

The question posed by Berg et al. [2017] is an important one: how will soils respond to the increased aridity projected under global warming? Our results indicate that model predictions are sensitive to the parameterization of root water uptake. The two models considered here (SMS/PHS) disagree over the level of communication between surface and deep soil moisture, with the strongest effects in semi-arid regions, which showed increased soil moisture memory and interannual variability of photosynthesis with PHS. We argue that the seasonal and interannual dynamics of root water uptake in SMS are in conflict with fundamental precepts of soil and plant hydraulic theory. This could have significant implications for vegetation function under climate change, and by extension the global water and carbon cycles, given the large influence of soil moisture on carbon cycle projections [Green et al., 2019]. While significant structural and parametric uncertainties remain in the continued development of plant hydraulic models on the ESM scale [Verhoef and Egea, 2014, Mencuccini et al., 2019], gradient flow for root water uptake has a strong physical basis in well-established hydraulic theory.

Chapter 3

Pitfalls in isohydricity and their corrections

3.1 Introduction

Water is critical for vegetation growth and maintenance, but it is often a limited resource, with a large influence on terrestrial biosphere productivity [Green et al., 2019, Humphrey et al., 2018, Anderegg et al., 2018]. Determining how to acquire, store, and utilize water to live and reproduce effectively defines a plant's water-use strategy (WS). The emergent WS of a given plant should maximize in the given environment, while managing the risks associated with water shortage. Different species may present divergent WS's in the same climate, possibly to take advantage of unique ecological niches, or due to different degrees of risk tolerance. Because the vegetation xylem network is often the path of least resistance for water to travel from soil-to-atmosphere, the WS can have significant control over local hydrology [Porporato et al., 2001]. While much progress has been made at the leaf and tree levels, scaling such information to the landscape level is a significant challenge [Mencuccini et al., 2019]. Limitations in our understanding of vegetation WS on the ecosystem scale has been identified as a major driver of carbon cycle uncertainty [Trugman et al., 2018].

Observations indicate a diversity of vegetation WS's, with evidence of trait coordination and tradeoffs [Mencuccini et al., 2015, Fu and Meinzer, 2018, Liu et al., 2019]. As an example:

in dry environments, where open stomates will quickly lose water, plants may reduce leaf area to limit transpiration, while investing more nutrient resources per unit leaf area to increase photosynthetic yield [Wright et al., 2002]. WS depends on many components, including (among others): rooting depth, leaf area, and hydraulic architecture, but also more dynamic factors, such as leaf orientation and stomatal aperture [Mencuccini et al., 2019]. Stomatal optimality theory suggests that WS aims at optimizing leaf gas exchange, by regulating stomatal conductance to maximize carbon uptake relative to water lost to transpiration [Cowan and Farquhar, 1977]. Understanding the spectrum of water-use strategies, and how they respond to environmental variation, is critical for projecting how vegetation may be affected by climate change and for understanding the land-atmosphere feedbacks to the global water and carbon cycles.

Quantitative metrics are critical for comparing WS across sites, species, and/or climates [Ratzmann et al., 2019]. This could include plant morphological traits measured in laboratory assays (such as leaf turgor loss point) or empirical descriptions developed from transient observations of ecological response variables (such as transpiration or photosynthesis). Iso/anisohydry provides one such description of WS, classifying vegetation according to the dynamics of leaf water potential (Ψ_L), which reflects stomatal regulation as well as the vulnerability of xylem to cavitation. Various (at times conflicting) definitions of iso/anisohydry exist, as documented in multiple recent reports, such as the variation of Ψ_L to soil versus atmospheric drying [Martínez-Vilalta and Garcia-Forner, 2017, Hochberg et al., 2018, Novick et al., 2019, Li et al., 2019, Feng et al., 2019]. Broadly speaking, an isohydric plant will have small variations in Ψ_L compared to an anisohydric plant (iso- for near constant Ψ_L). Formerly described as a dichotomy [Tardieu and Simonneau, 1998], recent studies have

developed quantitative metrics to organize vegetation within a spectrum of iso/anisohydry [Martínez-Vilalta et al., 2014, Klein and Niu, 2014, Skelton et al., 2015, Meinzer et al., 2016]. However, the framework of iso/anisohydry, especially when defined according to Ψ_L regulation, has been criticized [Martínez-Vilalta and Garcia-Forner, 2017, Feng et al., 2019], including a call to abandon the terminology [Hochberg et al., 2018].

Despite these challenges, the iso/anisohydric framework has proven to be highly popular and widely-used [Hochberg et al., 2018, Novick et al., 2019]. This likely reflects the eco-physiological community's interest in identifying metrics that can generalize WS strategies across large landscapes (i.e. at policy- and management-relevant scales). Isohydricity is a particularly attractive method, notwithstanding its flaws, because it relies on a relatively minimal set of observations (i.e. primarily leaf water potential data). Moreover, this framework is also particularly attractive due to the fact that information about the regulation of leaf water potential can be detected from remote-sensing observations [Konings and Gentine, 2017]. Thus, rather than abandon the framework entirely, the goal of this study is to better understand the relationship between isohydricity metrics and vegetation WS.

We use a set of soil-plant-atmosphere models, ranging in complexity, to investigate the underlying meaning of isohydricity retrievals (as pertains to WS) and identify potential classification errors. The model-based approach allows us to derive analytical expressions of the underlying trait retrievals offered by various isohydricity metrics and to more methodically sample both environmental space and trait space to generate idealized experiments to test the fidelity of the resulting WS classifications. We consider two established metrics, isohydricity slope (σ, Martínez-Vilalta et al. [2014]) and hydroscape area (HA, Meinzer et al. [2016]) in comparison to a third metric, relative isoshydricity, defined herein. We describe

classification challenges resulting from trait coordination and environmental variability, suggest practical recommendations for metric retrieval, and discuss the value and limitations of isohydricity and the broader pursuit of response-based metrics of vegetation WS. We show that many of the pitfalls of isohydricity can be corrected with the relative isohydricity methods described here.

3.2 Water-use strategy and iso/anisohydry

Isohydricity metrics are formulated on the assumption that the emergent response of Ψ_L to transient environmental conditions captures meaningful facets of WS. Testing this assumption benefits from a clear mathematical framework of WS. As such, we define WS as the relationship between environmental forcing and ecological response (Figure 3.1). Depending on the specific application, some variables (such as Ψ_{soil}) could alternatively appear as a forcing, internal, and/or response variable. The broadest definition (as pictured) will designate any variables under significant vegetation control as model internal variables, such as Ψ_{soil} and leaf area. Metrics of WS should measure the influence of vegetation in a way that consistently reproduces the relationship between forcing and response.

If WS metrics capture internal model processes, we can define a 'response indicator' (RI) as the result of a certain WS given certain forcing conditions (F), such that WS(F)=RI. Both WS metrics and response indicators are of interest, but have different purposes. WS provides a generic description of plant function meant to apply across environmental conditions, whereas a response indicator can offer a better sense of a plant's vulnerability to a particular set of environmental conditions. Given a model of plant function and observa-

tions of environmental conditions, one can convert between WS and RI as needed. Carrying out such a conversion should be considered in lieu of comparing WS metrics with response indicators. The distinction between WS metrics and response indicators, may partly explain why σ, a WS metric, was not correlated with minimum Ψ_L or the seasonal range in Ψ_L [Martínez-Vilalta and Garcia-Forner, 2017], which are instead response indicators.

The isohydricity slope, σ is defined in Martínez-Vilalta et al. [2014] as the slope of the relationship between midday Ψ_L and soil water potential, Ψ_s (Equation 3.1).

$$\sigma = \frac{d\Psi_L}{d\Psi_s} \tag{3.1}$$

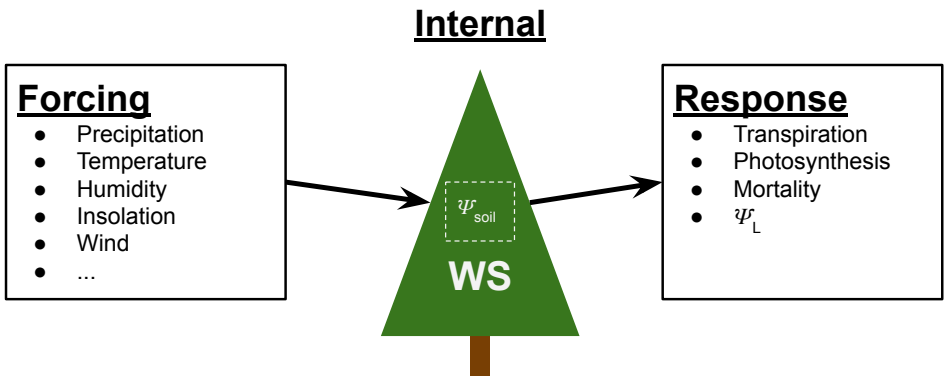

Figure 3.1: Water-use strategy (WS) can be conceptualized as the transfer function between meteorological forcing and ecological response. Depending on the framework definition, some variables (such as Ψ_{soil}) could appear as any of forcing, internal, or response variables.

If our interest were solely predicting Ψ_L, we could expect that a satisfactory isohydricity metric would perform well. However, when it comes to assessing WS metrics, we are typically more interested in the changes in transpiration, photosynthesis, and/or mortality in response to environmental drivers (e.g. drought or heat wave) than in Ψ_L, itself. As such, the burden of proof for isohydricity metrics exceeds simply modeling Ψ_L, but also that the information

distilled from the dynamics in Ψ_L plays an important part in determining transpiration, photosynthesis, mortality, or some combination thereof. Plant hydraulic theory suggests that Ψ_L is indeed a unifying variable coordinating transpiration supply and loss [Sperry and Love, 2015] and governing the risk of highly damaging xylem cavitation that can lead to mortality [Delzon and Cochard, 2014]. Likewise plant water potential has been shown to improve empirical stomatal models [Novick et al., 2016b, Anderegg et al., 2017], establishing a basis for isohydricity metrics.

The appeal of σ is that it reduces the complexity of soil-plant-atmosphere relations to a single variable, which can be used to compare across different climates and/or species. This allows for organizing species and/or individuals in a digestible way that should capture how plants respond to drying soils. The common interpretation is that more isohydric plants (lower σ) are hydraulic-risk-averse, closing stomates earlier into a drought to prevent hydraulic failure associated with overly negative Ψ_L, whereas more anisohydric plants (higher σ) operate further into drought or heat wave in favor of continued carbon assimilation. The metric can be computed from field-measured transient Ψ_L data, using predawn Ψ_L as a proxy for Ψ_s, but has also been estimated at the landscape-scale utilizing microwave remote sensing data [Li et al., 2017, Konings and Gentine, 2017]. Recent applications include using σ to investigate how ecosystems respond to variations in precipitation and vapor pressure deficit in grasslands [Konings et al., 2017] and tropical forests [Giardina et al., 2018].

However, multiple studies have pointed to some limits of the σ metric [Feng et al., 2019, Hochberg et al., 2018], including a common garden experiment where σ retrievals were not in line with the varying hydraulic function of 10 eucalypt species [Li et al., 2019]. Moreover the risk-tolerant/risk-averse interpretations of anisohydric versus isohydric behavior do not

always align with empirical findings [Garcia-Forner et al., 2017, Hochberg et al., 2018, Li et al., 2019]. Finally, the functional space describing the diversity of WS's likely exceeds the single dimension implied by the σ metric [Feng et al., 2018]. This leads to our driving question: is σ actually capturing a meaningful and predictive facet of vegetation WS?

3.3 Isohydricity pitfalls and their corrections

3.3.1 Theoretical derivation of isohydricity

Throughout this study, we use a suite of soil-plant-atmosphere models, of increasing complexity to investigate σ and identify potential classification errors. Operating from a modeling perspective allows us to supplement and advance recent work oriented from an empirical perspective [Hochberg et al., 2018, Feng et al., 2019, Li et al., 2019]. Specifically, such analytical work allows quantifying potential limits in the isohydric metric and where/if the pitfalls could be resolved. Using models, we can methodically sample the vegetation trait space and hydrologic conditions in a way that is not possible in the field. Likewise, the model output provides high-resolution output of all the pertinent outcome variables (Ψ_L, stomatal conductance, transpiration, and photosynthesis), which will be used to assess the metric retrievals. Subject to model assumptions, we know the "truth" so that we can directly assess the meaningfulness of isohydricity in the absence of measurement errors and biases.

We can also use the modeling framework to develop analytical definitions of various relevant WS metrics. In other words, what trait or combination of traits are driving the relationship embedded in the σ retrieval? To answer this, we start by inspecting the soil-

plant-atmosphere continuum (SPAC) model used in Martínez-Vilalta et al. [2014] (Equations 3.2-3.4). This is a simplified, steady-state, SPAC model with transpiration (T) set to match sap flux (J), neglecting hydraulic segmentation, plant water storage, the leaf boundary layer, and gravitational effects.

$$T = g_L \cdot A_L \cdot D_L = -k_s \cdot A_s \cdot (\Psi_L - \Psi_s) = J \tag{3.2}$$

Stomatal conductance (g_L) and whole-plant hydraulic conductance (k_s) are estimated by multiplying a maximum conductance parameter ($g_{L,\max}$, $k_{s,\max}$) by an attenuation function that declines from 1 to 0 as soils dry (f_g and f_k,(Equations 3.3,3.4), respectively). We make a small correction to Martínez-Vilalta et al. [2014], emphasizing that transpiration depends on leaf-level vapor pressure deficit, which we will refer to as D_L, and not on air vapor pressure deficit [Lin et al., 2018]. Both f_g and f_k are defined as functions of only Ψ_s, neglecting the effects of insolation, vapor pressure deficit, and CO_2 concentration that have been observed in the literature [Medlyn et al., 2011, Sperry et al., 1998].

$$g_L = g_{L,\max} \cdot f_g(\Psi_s) \tag{3.3}$$

$$k_s = k_{s,\max} \cdot f_k(\Psi_s) \tag{3.4}$$

Our goal is to derive an expression for σ in terms of the vegetation traits it serves to measure. To do so we need only find the expression for Ψ_L and then diffentiate with respect to Ψ_s, recalling that $\sigma = \dfrac{d\Psi_L}{d\Psi_s}$. Equations 3.2-3.4 can be combined and rearranged to yield

the following expression for Ψ_L:

$$\Psi_L = \Psi_s - D_L \cdot \frac{g_{L,\max} \cdot A_L}{k_{s,\max} \cdot A_s} \cdot \frac{f_g}{f_k} \tag{3.5}$$

which, when differentiated with respect to Ψ_s yields:

$$\sigma = 1 - \frac{d}{d\Psi_s}\left(D_L \cdot \frac{g_{L,\max} \cdot A_L}{k_{s,\max} \cdot A_s} \cdot \frac{f_g}{f_k}\right) \tag{3.6}$$

As defined, $g_{L,\max}$ and $k_{s,\max}$ do not depend on Ψ_s and can be pulled outside the differentiation operator via the product rule. Conversely f_g and f_k must remain inside the derivative. D_L is not independent of soil water potential, but instead is strongly correlated with Ψ_s through land-atmosphere feedbacks [Seneviratne et al., 2010, Zhou et al., 2019a,b], such that we opt to leave it inside the derivative (Equation 3.7). For brevity, we neglect any correlation between $\frac{A_L}{A_s}$ and Ψ_s, which tends to have relatively small effects on leaf water potential dynamics when compared to the effects of D_L [Novick et al., 2019].

$$\sigma = 1 - \left(\frac{g_{L,\max} \cdot A_L}{k_{s,\max} \cdot A_s}\right) \cdot \frac{d}{d\Psi_s}\left(D_L \cdot \frac{f_g}{f_k}\right) \tag{3.7}$$

Equation 3.7, previously unreported to our knowledge, specifically identifies the combination of traits retrieved by σ, as suggested by the simplified SPAC model described in Martínez-Vilalta et al. [2014]. Whereas σ is typically described in terms of stomatal regulation, Equation 3.7 demonstrates that the metric instead depends on the ratio of stomatal to xylem conductance, via $(g_{L,\max}/k_{s,\max})$ and (f_g/f_k). In addition to standard plant traits such as $g_{L,\max}$ and $k_{s,\max}$, the expression shows that σ depends on D_L, which is largely under

environmental control. Because σ does not control for D_L, it is not strictly a measure of vegetation WS and will not consistently reproduce the relationship between meteorological forcing and ecological response.

3.3.2 Correcting isohydricity: a new metric

Our goal was to adapt the σ metric in a way that allows reliable comparison across sites, species, and climates. There were two major constraints for this process: first that we must be able to compute this new metric with a similar set of observational data, and second that it still has its basis in the concept of iso/anisohydry. As such, our new metric still involves a regression against Ψ_s, but will no longer use Ψ_L as the independent variable, as with σ. Our approach was to reverse-engineer the process, starting with the specific combination of traits we seek to measure. To achieve a narrower trait retrieval and removes the effect of D_L, we chose to measure the variations of f_g/f_k in response to changes in Ψ_s, which maintains a basis in the concept of iso/anisohydry.

Therefore the first step in engineering our new regression is to derive an expression for f_g/f_k, which can be achieved by rearranging Equation 3.5 to yield:

$$\frac{f_g}{f_k} = -\frac{\Psi_L - \Psi_s}{D_L \cdot \dfrac{g_{L,\max} \cdot A_L}{k_{s,\max} \cdot A_s}} \tag{3.8}$$

As a result, if instead of using Ψ_L as the independent variable for our regression, we use the right side of 3.8, we will be measuring the variations in f_g/f_k. This is a much narrower trait definition than provided by σ (Equation 3.7). Likewise in rearranging Equation 3.5 to arrive at Equation 3.8, we divided by D_L, which served to remove the effects of D_L from

our regression. To simplify Equation 3.8 further, we introduce the isohydricity intercept parameter (Λ), defined in Martínez-Vilalta et al. [2014].

$$\Lambda = -D_{L,0} \cdot \frac{g_{L,\max} \cdot A_L}{k_{s,\max} \cdot A_s} \tag{3.9}$$

Λ is the value of Ψ_L when $\Psi_s \approx 0$, which likewise measures the soil-to-leaf water potential gradient at $\Psi_s \approx 0$. This can be used to simplify our expression for f_g/f_k, given that Λ is very similar to the denominator in 3.8. A major advantage of using this substitution is that it allows the new metric to be calculated with similar data to the standard σ retrieval [Martínez-Vilalta et al., 2014]. However, we emphasize that Λ depends not on generic D_L, but rather on $D_{L,0}$, the value of D_L when $\Psi_s \approx 0$. Due to the correlation between D_L and Ψ_s through land-atmosphere feedbacks [Seneviratne et al., 2010, Zhou et al., 2019a,b], we cannot assume that $D_{L,0} = D_L$.

Our new expression after substitution is:

$$\frac{f_g}{f_k} = \frac{D_{L,0}}{D_L} \cdot \frac{\Psi_L - \Psi_s}{\Lambda} \tag{3.10}$$

The final step in the metric derivation is to differentiate with respect to Ψ_s. Whereas the standard σ retrieval utilizes the total derivative notation [Martínez-Vilalta et al., 2014], this can alias to Ψ_s what are actually D_L effects [Novick et al., 2019]. So instead we utilize the partial derivative with respect to Ψ_s, emphasizing that we are tracking variations of f_g/f_k

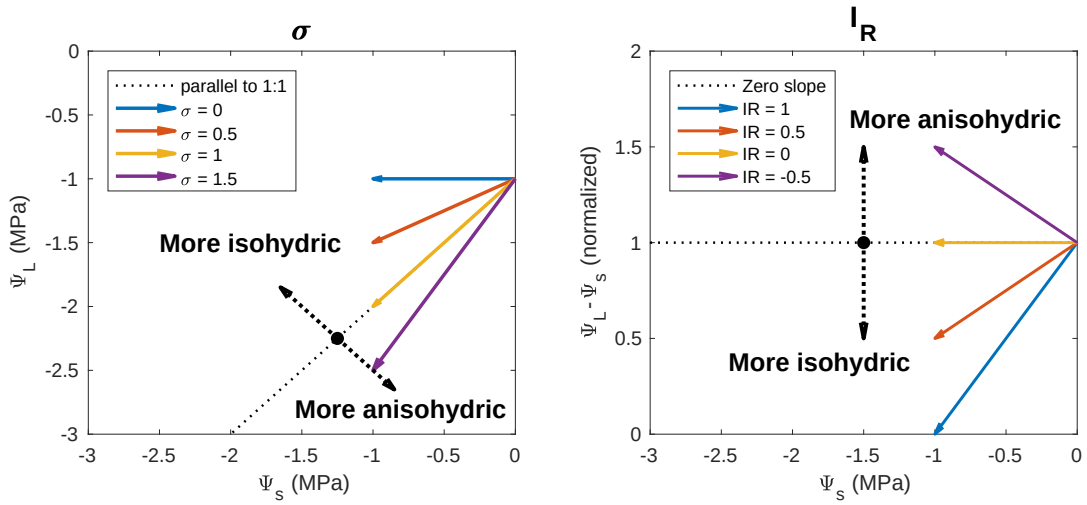

Figure 3.2: Comparing metric regressions for σ and I_R. While both metrics involve regression against Ψ_s, I_R tracks variations in the normalized soil-to-leaf water potential gradient (see Equation 3.12), whereas σ tracks Ψ_L directly.

only in response to Ψ_s variations, and not due to the correlated variations in D_L.

$$\frac{\partial}{\partial \Psi_s}\left(\frac{f_g}{f_k}\right) = \frac{\partial}{\partial \Psi_s}\left(\frac{D_{L,0}}{D_L}^{1} \cdot \frac{\Psi_L - \Psi_s}{\Lambda}\right) \tag{3.11}$$

We can simplify this expression further by noting that the derivatives of Ψ_L and Ψ_s with respect to Ψ_s, are by definition σ and 1, respectively. We utilize the σ_{Ψ_s} notation defined in Novick et al. [2019], which emphasizes that we are referring to σ resulting from the effects of only Ψ_s on Ψ_L, and not the effects of D_L. Λ is by definition a constant, and is expected to be negative. To remove any ambiguity due to sign conventions, we use the absolute value of Λ (multiplying by -1, accordingly). As a result we reach the simplified expression for an alternative isohydricity metric:

$$I_R = \frac{\partial}{\partial \Psi_s}\left(\frac{f_g}{f_k}\right) = \frac{1 - \sigma_{\Psi_s}}{|\Lambda|} \tag{3.12}$$

We refer to this new metric as relative isohydricity (I_R), which refers to the normalization by Λ. Instead of tracking the dynamics of Ψ_L with respect to Ψ_s (as in σ), this new metric tracks the dynamics of $\Psi_L - \Psi_s$, which is the gradient in water potential from soil to leaf ($\Delta\Psi$). Dividing by Λ serves to normalize by the initial potential gradient $\Delta\Psi$, and has the effect of normalizing for $D_{L,0}$. Due to this normalization, I_R relates to an/isohydric effects relative to well-watered conditions and does not capture variability across species in maximum transpiration or maximum photosynthesis. Furthermore I_R 'forces' with Ψ_s, such that aspects of WS that affect the evolution of Ψ_s from one day to the next are not explicitly captured. In this way the I_R metric captures just one dimension of WS. Follow up work could consider the extent to which I_R is correlated (or not) with complementary metrics designed to describe these other aspects of WS.

Whereas σ is the regression slope of Ψ_L versus Ψ_s, we can diagnose I_R by plotting $(\Psi_L - \Psi_s)/|\Lambda|$ versus Ψ_s (taking care to control for covarying D_L, discussed further in Section 3.4.3). When plotting Ψ_L (as in σ), two modes of variability are combined: Ψ_s dynamics and $\Delta\Psi$ dynamics. With Ψ_s as the dependent variable the Ψ_s dynamics are immutably 1:1. This has led to the historical convention defining plants as being isohydric when $\sigma < 1$ and anisohydric when $\sigma \geq 1$, which requires discerning whether the slope of the σ regression is greater than or less than 1 (Figure 3.2a). With I_R, Ψ_s is removed, and instead a normalized version of $\Delta\Psi$ is used as the independent variable. Plants are classified as isohydric if the soil-to-leaf potential gradient decreases as soils dry ($I_R > 0$), or anisohydric if the gradient increases as soils dry ($I_R \geq 0$). This leads to an easier visual interpretation, simply discerning whether the data are trending up or down (Figure 3.2b). Note that the two metrics function in opposite directions: a higher value of σ means more anisohydric, while a higher value of

I_R means more isohydric. As such, we would say that σ is an anisohydricity metric, whereas I_R is an isohydricity metric.

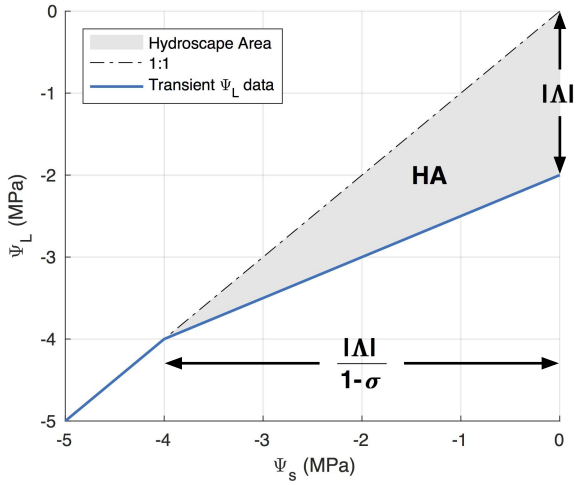

Figure 3.3: Schematic representation of the hydroscape area as defined in Meinzer et al. [2016]. HA is defined as the area of the triangle (shaded above) bounded by the σ regression (drawn in blue), the 1:1 line (dashed), and the y-axis. Larger HA is associated with more anisohydric behavior.

Meinzer et al. [2016] suggested an alternative isohydricity metric, the hydroscape area (HA), defined as the area bounded by the σ regression, the 1:1 line, and the y-axis, when plotting Ψ_L versus Ψ_s (Figure 3.3). Larger HA is associated with more anisohydric behavior, such that, like σ, HA is an anisohydricity metric. Meinzer et al. [2016] showed that HA was strongly correlated with leaf osmotic potential at full and zero turgor. Follow-up work found that HA showed stronger correlations than σ to the functional traits of 10 hydraulically diverse eucalypt species in a common garden experiment [Li et al., 2019]. The base of the HA triangle has length $|\Lambda|/(1-\sigma)$, and the height is Λ, such that:

$$\text{HA} = \frac{1}{2}\frac{\Lambda^2}{1-\sigma} \tag{3.13}$$

HA is similar in form to I_R, because the base of its triangle is the inverse of I_R. As such we expect a strong (albeit inverse) relationship between HA and I_R. The fact that HA measures anisohydricity and I_R, isohydricity, explains the inverse relationship. However, HA uses σ and not σ_{Ψ_s}, which could lead to inconsistent classifications due to contributions of covarying D_L. Furthermore, the height of the HA triangle is $|\Lambda|$, which introduces an additional dependence on $D_{L,0}$. Equation 3.14 presents the HA trait retrieval relative to the simplified SPAC model of Equations 3.2-3.4. While HA may function well in common-garden experiments, it may feature classification errors when compared across climates. We propose that I_R may feature some of the benefits attributed to HA, while reducing environmental dependence.

$$\mathrm{HA} = \frac{1}{2} \frac{\dfrac{g_{L,\max} \cdot A_L}{k_{s,\max} \cdot A_s} \cdot D_{L,0}^2}{\dfrac{d}{d\Psi_s}\left(\dfrac{f_g}{f_k} \cdot D_L\right)} \tag{3.14}$$

3.4 Four idealized test cases

Section 3.3 used a simplified SPAC model to analytically identify the pitfalls of the conventional isohydricity metric (σ) and to introduce a more appropriate relative isohydricity metic, I_R (Equation 3.12). This section presents four idealized cases to test whether I_R, and former σ, accurately reflect the underlying vegetation WS. In each of the first three experiments, the vegetation traits were defined to impose identical stomatal regulation ($df_g/d\Psi_s$) in the control and variant cases. Consequently, we would expect equivalent metric diagnoses for the control and variant cases. These experiments were designed to reveal potential WS misclassifications using either σ, I_R, or both. The fourth experiment imposes more complex

trait parameterizations to demonstrate the challenges of nonlinear isohydricity response. Brief descriptions of each experiment are provided below, with detailed summaries of the model and experimental setup provided in Appendices C.1 and C.2.

3.4.1 Experiment 1: absolute versus relative isohydricity

In our first experiment, we utilized the same simplified SPAC model (Equations 3.2-3.4) to consider two co-located species with distinct values of σ.

$$\begin{array}{ll} \text{Species 1:} & \text{Species 2:} \\ \sigma_1 = 0.75 & \sigma_2 = 0.5 \\ \Lambda_1 = -1\text{MPa} & \Lambda_2 = -2\text{MPa} \end{array} \tag{3.15}$$

We defined Species 1 to have a larger value of σ, indicating more anisohydric behavaior compared to Species 2 (Figure 3.4a). Positive correlation between the σ and Λ parameters has been observed in the field and in remote sensing data [Martínez-Vilalta et al., 2014, Konings and Gentine, 2017], and both parameters show correlations with forest height [Konings and Gentine, 2017]. According to these findings, we set Λ_2 to be more negative than Λ_1. This indicates that Species 2 has a larger initial water potential gradient from soil-to-leaf.

We now consider a hypothetical soil drydown, assuming that there are no noticeable changes in k_s or D_L. Because k_s and D_L are held constant, $T_{\text{dry}}/T_{\text{wet}}$ will be equal to the ratio of soil-to-leaf water potential gradient at the end of the drydown versus the beginning ($\Delta\Psi_{\text{dry}}/\Delta\Psi_{\text{wet}}$). Species 2 is more isohydric, losing 0.5MPa of gradient per 1MPa of soil

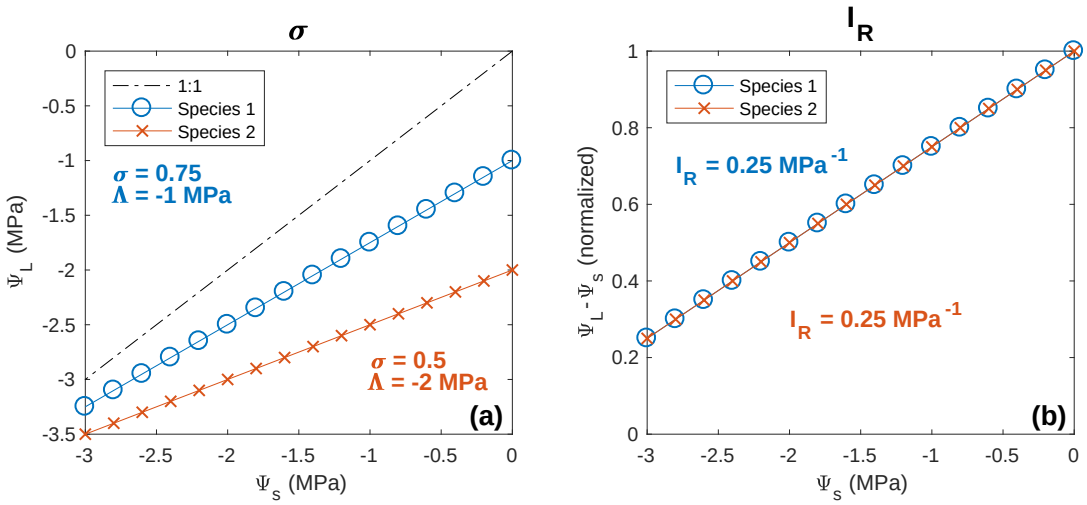

Figure 3.4: Despite equivalent stomatal regulation Experiment 1, absolute versus relative isohydricity. Two distinct species were defined such that coordination between σ and Λ results in identical stomatal regulation. The absolute isohydricity metric, σ, diagnoses distinct WS's (a), whereas the relative isohydricity metric, I_R, diagnoses identical WS's (b).

drydown, while Species 1 loses only 0.25MPa per 1MPa (gradient losses are defined by 1-σ). However, because Species 2 likewise has a larger initial gradient (-2MPa vs. -1MPa for Species 1), the relative loss of gradient is equivalent, with both species losing 25% of their initial gradients per 1MPa of drying. As a result, transpiration losses will likewise be equivalent, with reductions of 25% of the initial transpiration for each 1MPa of soil drying.

In this example, both species impose equivalent stomatal regulation in response to soil drying, however Species 2 is classified as more isohydric by σ (Figure 3.4a). As such, the σ retrieval is inconsistent with the observed WS on transpiration. Likewise HA would feature distinct retrievals for the two species, however with Species 2 classified as less isohydric. This inconsistency is resolved using the I_R framework (Figure 3.4b), which diagnoses identical values for both species: I_R=0.25 MPa^{-1}, consistent with the calculation of transpiration reduction above. I_R takes into account not just the rate at which a plant loses water

potential gradient from soil-to-leaf (1-σ), but also how much it started with, $|\Lambda|$. In an absolute sense, Species 2 loses more gradient during a given drydown, but the amount of transpiration regulation is the same, because Species 2 had more gradient initially. The coordination of σ and Λ may partly explain the counter-intuitive finding that taller forests across Amazonia, with lower σ, were less sensitive to precipitation variability than shorter forests [Giardina et al., 2018]. When accounting for coordinated effects on Λ, we might find that the taller forests would present as *less* isohydric than shorter forests, as measured by I_R .

3.4.2 Experiment 2: altering atmospheric demand via mean D_L

Whereas our first experiment utilized a common garden experiment, the second tests for stable classification across climates. To test this we must use an alternative plant hydraulics model (described in Appendix C.1) that better represents the influence of D_L. We generated two simulations using identical traits and identical meteorological forcing, except that one simulation takes place with D_L=1kPa, while the other has D_L=3kPa. Again we disallow covariation between D_L and define k_s to be constant (these simplifications are removed in Experiments 3 and 4, respectively).

The resulting values for σ were 0.7 and 0.56 under low and high D_L, respectively, incorrectly inferring distinct WS's despite identical traits. With higher D_L, the same plant is observed to be more isohydric, according to σ, further emphasizing that σ does not translate into plant traits but is rather dependent on the environment [Feng et al., 2019, Novick et al., 2019]. HA would likewise result in two distinct classifications, although with the higher D_L

case classified as less isohydric.The difference in classification follows from the dependence of the σ and HA metrics on D_L, as shown in Equations 3.7 and 3.14. Using the I_R framework, which removes the effect of $D_{L,0}$ through the normalization by Λ (Equation 3.10), the regression retrieves I_R=0.33 MPa^{-1} for both simulations and thus largely resolves the confounding interaction of environment and plant traits in the other two metrics.

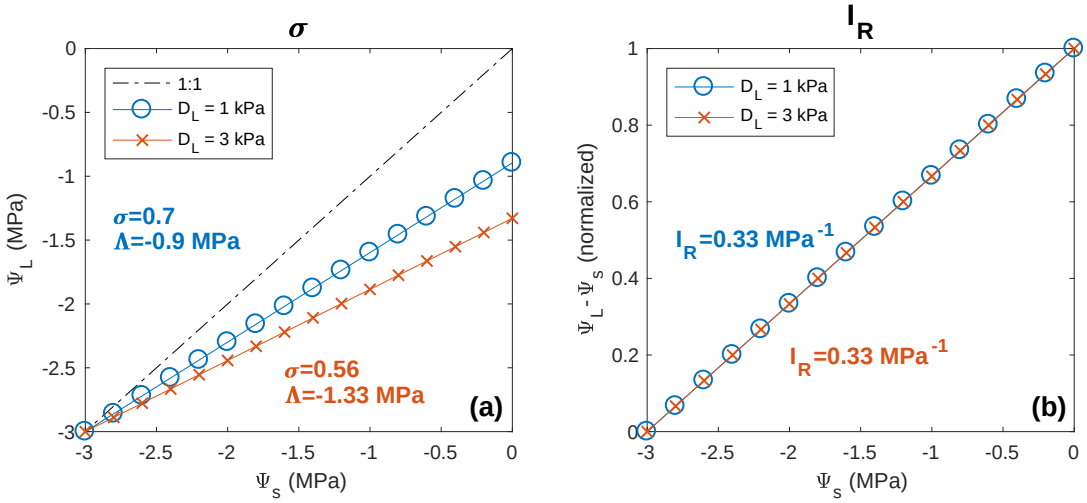

Figure 3.5: Experiment 2, altering mean D_L. Simulations with identical vegetation traits were performed with D_L=1kPa (blue curves) and 3kPa (red). (a) Resulting water potential data plotted in the σ framework. (b) Resulting water potential data plotted in the I_R framework. The I_R regression yields the same value in both cases, whereas σ depends on the climate state.

3.4.3 Experiment 3: D_L covaries with Ψ_s

Given the coupling between D_L and Ψ_s through land-atmosphere interactions [Seneviratne et al., 2010, Zhou et al., 2019a], we perform a similar test for covarying D_L with Ψ_s (Figure 3.6). We varied D_L on a linear ramp from 0.5 kPa to 3.5 kPa (red lines), as the soil dries from 0 to -3 MPa, with a control simulation where D_L is held constant at 0.5 kPa (blue lines).

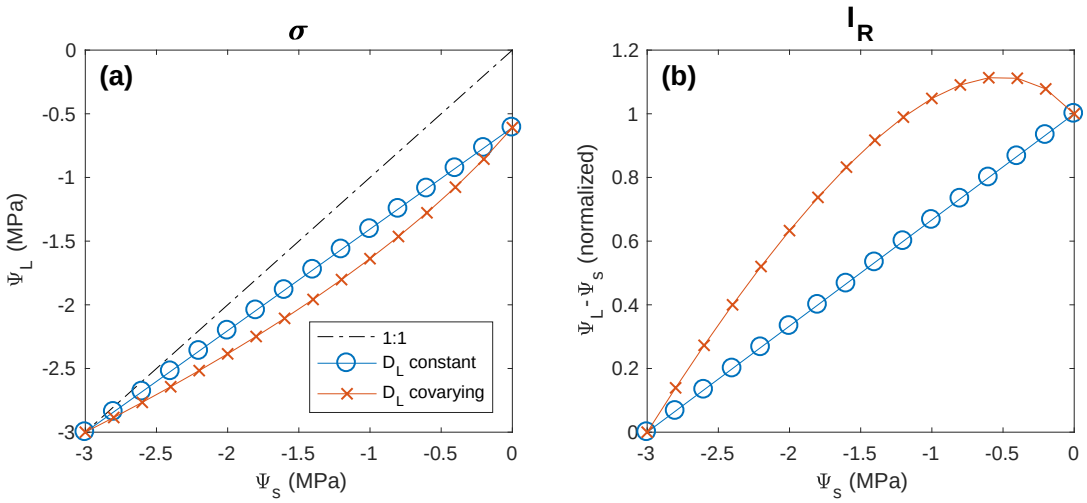

Figure 3.6: Experiment 3, the effect of covarying D_L. Simulations with identical vegetation traits were performed with constant (blue curves) and covarying (red) D_L. Neither σ nor I_R can achieve a stable retrieval when using the slope as measured by the total derivative. We suggest a suitable correction for I_R in Figure 3.7.

Despite identical vegetation traits used in the two simulations, both metrics are affected by D_L covarying with Ψ_s (Figure 3.6). Whereas in previous cases, the normalization process yielded identical retrievals for identical traits, in this case I_R (as plotted) indicates distinct WS's in the two simulations. With D_L constant, the plant reduces the normalized gradient at a constant rate of 0.33 per MPa. With D_L covarying, gradient first increases due to rising D_L, and then declines at a faster rate beyond Ψ_s=-1MPa. The distinct WS's result from the fact that we have not appropriately controlled for the effects of D_L as required by the derivation in Section 3.3.2.

To measure the effects of D_L, we carried out a supplementary experiment, where Ψ_s is set constant, while D_L is varied over the 0.5 kPa to 3.5 kPa (Figure 3.7a). This SPAC model has four distinct mechanisms by which D_L can influence the normalized water potential gradient.

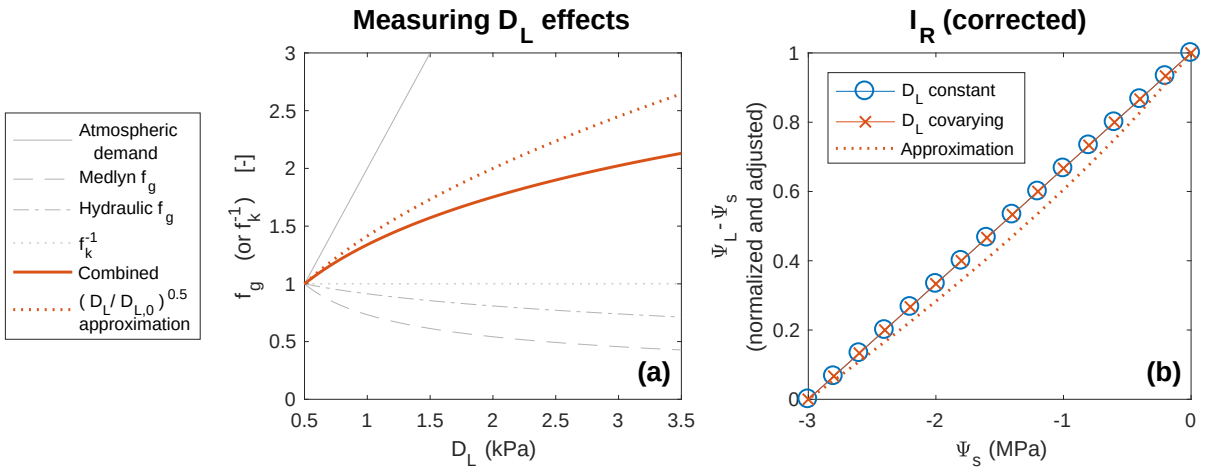

Figure 3.7: Removing the effect of covarying D_L. We can diagnose and remove the effects of covarying D_L using a control simulation where Ψ_s is constant and D_L varies. Panel (a) shows the various effects of covarying D_L, the combination of those effects, and a suitable approximation. Panel (b) shows the I_R regression under constant D_L (blue) and with covarying D_L after adjusting for the measured and approximated D_L effects.

1. Atmospheric demand: higher D_L leads to larger atmospheric demand with a positive effect on $\Delta\Psi$
2. Stomatal optimization (Medlyn f_g): with higher D_L, the Medlyn model reduces stomatal conductance, yielding a negative effect on $\Delta\Psi$.
3. Hydraulic stress (hydraulic f_g): the model includes a stress term proportional to Ψ_L, with higher D_L, Ψ_L is typically reduced, with a negative effect on $\Delta\Psi$.
4. Loss of hydraulic conductance (f_k^{-1}): whole plant hydraulic conductance will tend to decrease with higher D_L due to lower Ψ_L, with a positive effect on $\Delta\Psi$. By using the inverse (f_k^{-1}), the combined effect is the product of the four constituent factors.

We can observe each of these effects separately in the model simulation, recording the factor by which each multiplies $\Delta\Psi$ (Figure 3.7a). Increased atmospheric demand has the largest effect, countered by reductions from hydraulic stress and the Medlyn model. In this

experiment k_s is held constant, such that $f_k^{-1} = 1$. The combined effect (heavy red line) on $\Delta\Psi$ is positive. When the combined D_L effect is removed from Figure 3.6, we achieve a stable retrieval with I_R=0.33MPa^{-1} under both constant and covarying D_L (Figure 3.7b).

In this case, we can use the control simulation to separately estimate the effects resulting from variations in D_L. With transient observations, this can be estimated utilizing the framework of [Novick et al., 2019] to disentangle Ψ_s and D_L effects. While D_L and Ψ_s are strongly related on seasonal timescales [Seneviratne et al., 2010, Zhou et al., 2019a,b], daily or sub-daily observations could be used to independently sample D_L [Novick et al., 2016a, Stocker et al., 2018].

A rough approximation can be achieved by multiplying the observed $\Delta\Psi$ data by $(D_L/D_{L,0})^{-0.5}$, in order to estimate the effects of atmospheric demand and the Medlyn-induced stomatal closure (Figure 3.7, dotted red lines). Accounting for D_L effects on hydraulic f_g and f_k^{-1} would require information on the shapes of these curves which is not available a priori. However these two effects will be opposing, and we expect the net effect to be smaller than the atmospheric demand and Medlyn effects.

3.4.4 Experiment 4: dynamic hydraulic conductivity k_s

Our fourth experiment is designed to introduce two final complications:

1. Hydraulic conductivity (k_s) is allowed to vary.
2. Non-linear functions are used for f_k and f_g.

None of experiments 1-3 featured dynamic k_s, and the stomatal parameters were defined in such a way that f_g was a linear function of Ψ_s. Martínez-Vilalta et al. [2014] found that

a linear fit to Ψ_L was appropriate in the σ framework based on empirical data, but ensuing work has questioned the compatibility of linearity assumptions and current hydraulic theory [Hochberg et al., 2018].

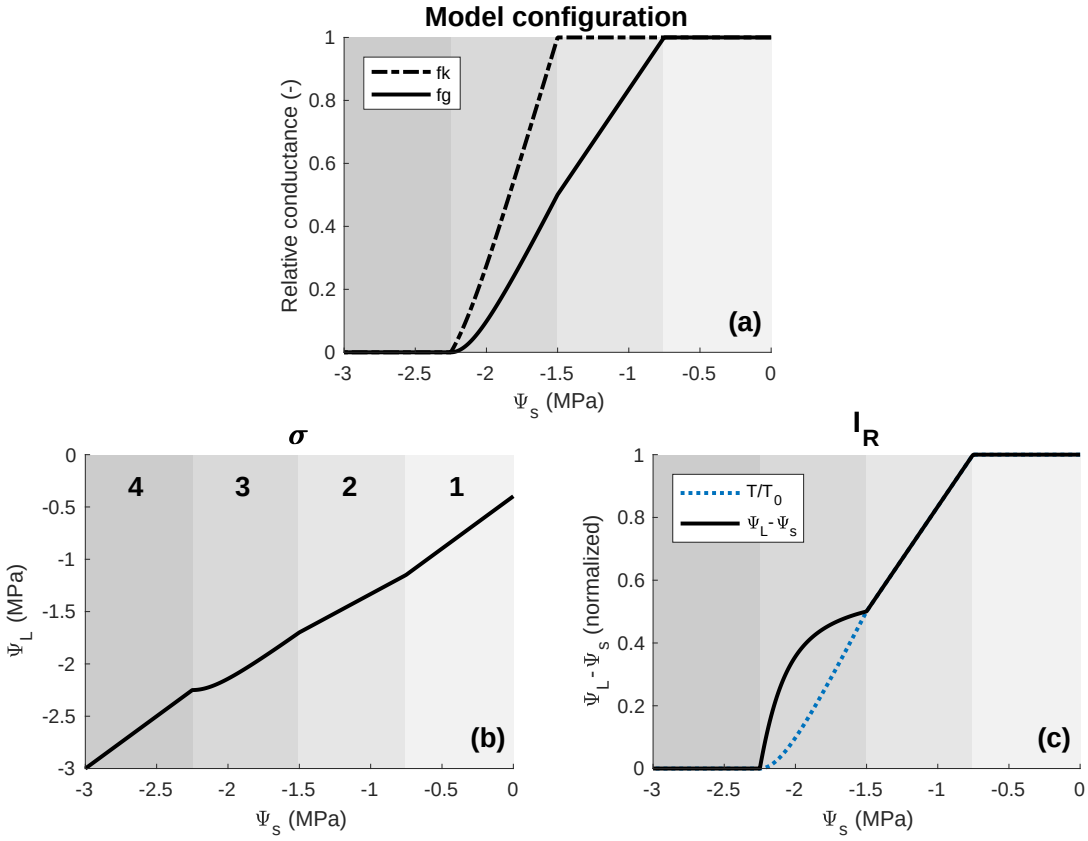

Figure 3.8: Experiment 4, non-linear vulnerability parameterizations lead to non-linear isohydricity curves. (a) Visual depiction of the model parameterizations for hydraulic vulnerability (f_k) and stomatal regulation (f_g). (b) Resulting water potential data plotted in the σ framework. (c) Resulting water potential data plotted in the I_R framework alongside relative transpiration. Plotting the same underlying data, the I_R framework more clearly identifies the four distinct regimes.

For Experiment 4, we defined non-linear parameterizations of hydraulic vulnerability and stomatal regulation using piecewise linear functions (Figure 3.8a, see Appendix C.1 for the full model description). These are idealized formulations of the conductances, but do conform with findings that relative stomatal closure tends to lead loss of hydraulic conductance

[Bartlett et al., 2016]. In this case, we revert to forcing with constant D_L=1kPa.

The resulting hydraulic behavior can be separated into 4 distinct regimes:

1. No stomatal regulation, no hydraulic vulnerability: σ=1, I_R=0 MPa^{-1}.
2. Stomatal regulation only: σ=0.73, I_R=0.67 MPa^{-1}.
3. Stomatal regulation and loss of hydraulic conductance: σ=0.95→0.02, I_R=0.12→2.5 MPa^{-1}.
4. Zero transpiration: σ=1, I_R=0 MPa^{-1}.

The two metrics utilize different scales but are fundamentally in agreement on the observed WS. The distinct behavior among Regimes 1, 2, and 3 occurs in response to the sequencing of onset of stomatal closure versus onset of hydraulic vulnerability. Stomatal closure does not begin until Ψ_s=-0.75MPa, creating Regime 1, which features the pure anisohydry of constant $\Delta\Psi$. Regime 2 features stress-induced isohydry, where the normalized gradient shrinks due to stomatal closure. Regime 3 can be identified by the decoupling of $\Delta\Psi$ and T. $\Delta\Psi$ responds to the ratio of stomatal to hydraulic conductance, while T remains proportional to stomatal conductance, leading to a decoupling effect while hydraulic conductance declines. Regime 4 is marked by the cessation of transpiration. Data from Regime 4 should generally be excluded from metric retrievals, given the limited effect of WS absent transpiration. However, time spent in Regime 4 may be of interest for diagnosing drought-induced mortality [Gentine et al., 2016, McDowell et al., 2018].

The non-linearity of Experiment 4 presents a challenge to scalar metric retrieval, in both the σ and I_R frameworks. In such cases, a single parameter value will be inadequate to describe a plant's isohydricity. Describing WS in Regimes 1 and 2 could be achieved with

two parameters: the soil water potential at stress onset and then an I_R value to be applied thereafter, but only up to the threshold of Regime 3. Though the inferred WS in this case would be a function of Ψ_s, we are still in effect controlling for environmental conditions.

Describing WS in Regime 3 is significantly more challenging. The standard interpretation of iso/anisohydry would characterize the more anisohydric behavior at the beginning of Regime 3 as evidence of *reduced* stomatal regulation. However the rate of stomatal regulation is slightly increased (Figure 3.8b), and the apparent anisohydry actually results from hydraulic vulnerability. If in response to drydown, a plant applies a 50% reduction in stomatal conductance, but also experiences a 50% loss of hydraulic conductance, the opposing effects would yield constant Ψ_L. Said plant looks identical (according to I_R, σ, and HA) to a plant that applies no reduction in stomatal conductance and experiences no loss of hydraulic conductance (which would likewise result in constant Ψ_L). However these two plants clearly have differing WS, as the first would experience an $\sim$50% reduction in transpiration/photosynthesis, while we would expect the second to maintain maximal values. This mismatch is a fundamental issue that must be resolved in order to correctly interpret I_R or other such isohydricity metrics (discussed in Section 3.5.2).

3.5 Discussion

3.5.1 Advantages of the I_R metric

In Section 3.3.2, we define relative isohydricity (I_R), which tracks variations in the soil-to-leaf water potential gradient ($\Delta\Psi$) in response to changes in Ψ_s. This metric effectively

normalizes the traditional isohydric metric by the well-watered leaf water potential (i.e. Λ), and in doing so reduces noise and the confounding influence in environment-trait interactions which have challenged the application of the isohydricity concept over coarse spatial scales. Our new metric, however, retains many of the feautures that made σ attractive in the first place, including minimal data requirements, and clear tractability with WS strategies that has clear consequences for both carbon uptake (through stomatal closure) and the risk of drought-driven mortality (by describing the likelihood of excessively low Ψ_L that can lead to cavitation.

Tracking $\Delta\Psi$ instead of Ψ_L (as in σ) enables easier (visual) interpretation of the isohydricity curves (Figure 3.2) and introduces I_R as a new isohydricity metric, where larger values are associated with more isohydric behavior. I_R offers a narrower trait retrieval, measuring the relative changes in the ratio of stomatal to hydraulic conductance in response to soil drying (Equation 3.12). I_R normalizes $\Delta\Psi$ by Λ (Equation 3.11), which is the value of Ψ_L when $\Psi_s = 0$ and the well-watered value of $\Delta\Psi$. This normalization posits that the rate of change of $\Delta\Psi$ should be measured against the amount of $\Delta\Psi$ originally available (Λ). Furthermore, accounting for Λ serves to remove any dependence on $D_{L,0}$. As a result, two distinct classification errors that occur using σ are easily avoided with I_R.

1. Two species with equivalent stomatal regulation resulting from coordination between σ and Λ are classified by σ as having distinct WS, whereas I_R yields the same value for both cases (Figure 3.4).
2. A single species with static hydraulic traits features a stable retrieval with I_R when mean D_L is varied, but two distinct values for σ (Figure 3.5). Because σ does not

control for D_L it cannot consistently reproduce the effects of vegetation WS.

Extending beyond σ, we can compare I_R with an alternative isohydricity metric described in Meinzer et al. [2016], the hydroscape area (HA, Figure 3.3). HA was shown to correlate well with leaf osmotic potential at full and zero turgor [Meinzer et al., 2016], and showed stronger correlations than σ to several hydraulic traits in a common garden experiment featuring ten eucalpyt species [Li et al., 2019]. The length of the base of the HA triangle is $|\Lambda|/(1\text{-}\sigma)$, which is the inverse of I_R (when D_L is constant). As such we expect a strong relationship between HA and I_R. However, like σ, HA depends on D_L (Equation 3.14), which could cause misclassification when comparing across climates. For example in Figure 3.5, two species with identical traits would diverge in HA, which classifies the high D_L case as more anisohydric (whereas σ classifies the high D_L case as *less* anisohydric, and I_R provides equivalent metric retrievals for the high and low D_L cases). We propose that I_R may feature some of the benefits attributed to HA, while reducing potential environmental dependence.

3.5.2 Practical considerations

Isohydricity metrics are typically defined to measure the vegetation response to variations in Ψ_s [Hochberg et al., 2018]. However, due to the land-atmosphere feedbacks that couple D_L to Ψ_s [Seneviratne et al., 2010, Zhou et al., 2019b], a total derivative with respect to Ψ_s can alias what are actually D_L effects [Novick et al., 2019]. While this may be acceptable for common garden experiments, it presents a challenge for comparing across climates. As a result, neither I_R nor σ yielded a stable retrieval for a single species under constant vs. covarying D_L when a total derivative approach was utilized (Figure 3.6). However, to the extent

that it is possible to separately estimate Ψ_s vs. D_L effects (Figure 3.7) a stable retrieval can be achieved with I_R, by correcting for D_L effects (comparable to a partial derivative approach). In the case of covarying D_L, we would recommend applying the framework of Novick et al. [2019] to retrieve $I_{R_{\Psi_s}}$ and $I_{R_{D_L}}$ in analogy to their definitions of σ_{Ψ_s} and σ_{D_L}. Other variables subject to land-atmosphere feedbacks should also be inspected for possible covariation with Ψ_s, including A_L.

We further recommend testing linearity assumptions in practice and avoiding extrapolation of I_R outside the bounds of the Ψ_s observing conditions. While Martínez-Vilalta et al. [2014] justified a linear fit between Ψ_L and Ψ_s empirically, linearity is not guaranteed by plant hydraulic theory [Hochberg et al., 2018]. We examined three potential regimes of isohydric behavior (Figure 3.8) corresponding to: (1) free evolution of Ψ_L before stress onset (pure anisohydry), (2) stomatal regulation before tangible hydraulic losses (coupled regulation), and (3) stomatal regulation coincident with hydraulic vulnerability (decoupled regulation). We would recommend that I_R be fit only to data where $T > 0$, eschewing Regime 4 (in agreement with Meinzer et al. [2016]). Defining regimes and/or the use of multiple parameters may be required to effectively characterize the an/isohydric behavior in cases of pronounced non-linearity. Our results indicate that I_R shows promise for characterizing vegetation WS in the proposed Regimes 1 and 2, correcting potential misclassifications resulting from the σ and HA metrics. The extent to which such characterizations are useful will depend on the amount of time vegetation spends in Regimes 1 and 2, which will need to be investigated with observational data. A dependence of I_R on Ψ_s is not contrary to our goal of limiting the environmental dependence of our metric retrieval, because the procedure outlined here explicitly controls for Ψ_s and should result in the same empirical fit across

environments. The same cannot be said of σ, where changing mean D_L was shown to alter the metric retrieval despite identical hydraulic traits (Figure 3.5).

Interpreting isohydricity data in the case of varying k_s still represents a significant challenge. In our first three experiments we set k_s to remain constant, but allowed it to vary in Experiment 4 (Figure 3.8, Regime 3). While an/isohydry is typically discussed in terms of stomatal regulation, variations in $\Delta\Psi$ (and Ψ_L) instead respond to the ratio of stomatal to hydraulic conductance. In that way, isohydricity metrics (including I_R) do not track stomatal regulation per se, but the combined (opposing) effects of stomatal regulation and xylem vulnerability. The comparability of I_R retrievals in Regime 3, especially across species, will therefore depend on the extent to which the f_g/f_k ratio evolves in a consistent/orderly manner. There is empirical support for broadly consistent sequencing of various hydraulic traits [Bartlett et al., 2016], but the extent to which I_R captures a meaningful facet of WS in Regime 3 must be tested further with observations. If applying the an/isohydry concept through Regime 3 proves infeasible, alternative techniques might be developed that utilize Ψ_L data together with concurrent transpiration and/or photosynthesis observations, to disentangle the effects of stomatal regulation and hydraulic vulnerability.

3.6 Conclusion

While the framework of an/isohydry has been criticized in the recent literature [Martínez-Vilalta and Garcia-Forner, 2017, Hochberg et al., 2018, Feng et al., 2019], we found that several of the major flaws could be addressed by an alternative regression, which we call relative isohydricity. In our four idealized experiments, we showed that the I_R metric could

avoid the pitfalls of σ and HA, providing a meaningful description of WS that can be compared across species and climates. Response-based metrics are a valuable tool for generating insights about vegetation water-use strategy across large landscapes, which is the typical Earth System modeling scale as well as an important policy- and management-relevant scale. Observations of leaf water potential contain valuable information encoding both stomatal regulation as well as xylem vulnerability. Developing techniques to leverage these observations could provide new insights into vegetation water-use strategy and its effects on the global carbon and water cycles. Thus, rather than abandon the framework of an/isohydry entirely, the goal of this study is to better understand the relationship between isohydricity metrics and vegetation WS. We assert that WS metrics should explicitly identify the traits they measure. As such, we provide trait definitions for the three metrics discussed herein (Equations 3.7, 3.12, and 3.14) and conclude that I_R offers significant improvements over σ and HA.

Conclusions

Understanding how vegetation might respond to climate change is a critically important question, especially given the feedbacks from vegetation onto climate through adjustments to surface energy partitioning and potential changes in the terrestrial carbon sink. Models must be constructed with the non-stationary nature of our climate in mind. In light of this, we replaced a poorly-constrained empirical representation of vegetation hydrodynamics with a more mechanistic model that implements a simplified framework distilled from well-established plant and soil hydraulic theory. This work extends recent advances in describing plant hydraulic function and stomatal regulation to represent vegetation in an Earth System Model (ESM).

Considerable structural and parametric uncertainty remains in the ongoing development of plant hydraulic models on the ESM scale. In particular, we still lack a robust understanding of emerging vegetation function on these larger spatial scales. Traditional plant physiological research is conducted on a leaf-level or individual tree basis, with considerable uncertainty in the process of scaling up the stand or landscape scales. Understanding emergent vegetation water-use strategy is a critical road block to confidently modeling the global carbon and water cycles, both historically and under climate change.

We developed new techniques to better leverage leaf water potential data to infer water-

use strategy. Specifically, we derived a new metric of hydraulic regulation in response to soil drying, called relative isohydricity. Continued development of vegetation models will benefit from the expanded capacity to observe plant function at the landscape scale in response to environmental variability, using the stream of data from a constellation of Earth-observing satellites and the various site-level observation networks, including NEON and Fluxnet, among others. This includes testing the importance of relative isohydricity for describing drought-induced productivity losses and other hypotheses about vegetation water-use strategies.

Our results indicate that implementing plant hydraulics will have significant impacts on the global carbon and water cycles through increased sensitivity to vapor pressure deficit and a more flexible root water uptake paradigm. Our work simultaneously brings the CLM into better agreement with prevailing stomatal and hydraulic theory, while also enabling a new facet of benchmarking with leaf water potential observations. The next step in this process will be to test how implementing plant hydraulics influences projections of vegetation function under future climate change. Because PHS has been adopted as the default representation of vegetation hydrodynamics in CLM5/CESM2, we will have many opportunities do just that in the suite of experiments underway for the Climate Model Intercomparison Project, phase 6 (CMIP6).

Bibliography

A. Ahlström, M. R. Raupach, G. Schurgers, B. Smith, A. Arneth, M. Jung, M. Reichstein, J. G. Canadell, P. Friedlingstein, A. K. Jain, E. Kato, B. Poulter, S. Sitch, B. D. Stocker, N. Viovy, Y. P. Wang, A. Wiltshire, S. Zaehle, and N. Zeng. The dominant role of semi-arid ecosystems in the trend and variability of the land CO_2 sink. *Science*, 348(6237): 895–899, 2015. ISSN 0036-8075. doi: 10.1126/science.aaa1668.

C. D. Allen, A. K. Macalady, H. Chenchouni, D. Bachelet, N. McDowell, M. Vennetier, T. Kitzberger, A. Rigling, D. D. Breshears, E. T. Hogg, P. Gonzalez, R. Fensham, Z. Zhang, J. Castro, N. Demidova, J.-H. Lim, G. Allard, S. W. Running, A. Semerci, and N. Cobb. A global overview of drought and heat-induced tree mortality reveals emerging climate change risks for forests. *Forest Ecology and Management*, 259(4):660 – 684, 2010. ISSN 0378-1127. doi: https://doi.org/10.1016/j.foreco.2009.09.001. URL `http://www.sciencedirect.com/science/article/pii/S037811270900615X`.

W. R. L. Anderegg. Spatial and temporal variation in plant hydraulic traits and their relevance for climate change impacts on vegetation. *New Phytologist*, 205(3):1008–1014, 2015a. ISSN 1469-8137. doi: 10.1111/nph.12907.

W. R. L. Anderegg, J. M. Kane, and L. D. L. Anderegg. Consequences of widespread tree mortality triggered by drought and temperature stress. *Nature Climate Change*, 3(1): 30–36, 01 2013.

W. R. L. Anderegg, C. Schwalm, F. Biondi, J. J. Camarero, G. Koch, M. Litvak, K. Ogle, J. D. Shaw, E. Shevliakova, A. P. Williams, A. Wolf, E. Ziaco, and S. Pacala. Pervasive drought legacies in forest ecosystems and their implications for carbon cycle models. *Science*, 349(6247):528–532, 2015b. ISSN 0036-8075. doi: 10.1126/science.aab1833. URL `http://science.sciencemag.org/content/349/6247/528`.

W. R. L. Anderegg, A. Wolf, A. Arango-Velez, B. Choat, D. J. Chmura, S. Jansen, T. Kolb, S. Li, F. Meinzer, P. Pita, V. Resco de Dios, J. S. Sperry, B. T. Wolfe, and S. Pacala. Plant water potential improves prediction of empirical stomatal models. *PLOS ONE*, 12(10):1–17, 10 2017. doi: 10.1371/journal.pone.0185481. URL `https://doi.org/10.1371/journal.pone.0185481`.

W. R. L. Anderegg, A. G. Konings, A. T. Trugman, K. Yu, D. R. Bowling, R. Gabbitas, D. S. Karp, S. Pacala, J. S. Sperry, B. N. Sulman, and N. Zenes. Hydraulic diversity of forests regulates ecosystem resilience during drought. *Nature*, 561:538–541, 2018. doi: 10.1038/s41586-018-0539-7.

W. R. L. Anderegg, A. Wolf, A. Arango-Velez, B. Choat, D. J. Chmura, S. Jansen, T. Kolb, S. Li, F. C. Meinzer, P. Pita, V. Resco de Dios, J. S. Sperry, B. T. Wolfe, and S. Pacala. Woody plants optimise stomatal behaviour relative to hydraulic risk. *Ecology Letters*, 21 (7):968–977, 2018b. doi: 10.1111/ele.12962. URL https://onlinelibrary.wiley.com/doi/abs/10.1111/ele.12962.

R. Avissar, P. L. Silva Dias, M. A. F. Silva Dias, and C. Nobre. The large-scale biosphere-atmosphere experiment in Amazonia (LBA): Insights and future research needs. *Journal of Geophysical Research: Atmospheres*, 107(D20):LBA 54–1–LBA 54–6, 2002. doi: 10.1029/2002JD002704. URL https://agupubs.onlinelibrary.wiley.com/doi/abs/10.1029/2002JD002704.

D. Baldocchi, E. Falge, L. Gu, R. Olson, D. Hollinger, S. Running, P. Anthoni, C. Bernhofer, K. Davis, R. Evans, J. Fuentes, A. Goldstein, G. Katul, B. Law, X. Lee, Y. Malhi, T. Meyers, W. Munger, W. Oechel, K. T. Paw U, K. Pilegaard, H. P. Schmid, R. Valentini, S. Verma, T. Vesala, K. Wilson, and S. Wofsy. FLUXNET: A new tool to study the temporal and spatial variability of ecosystem-scale carbon dioxide, water vapor, and energy flux densities. *Bulletin of the American Meteorological Society*, 82(11):2415–2434, 2001. doi: 10.1175/1520-0477(2001)082⟨2415:FANTTS⟩2.3.CO;2. URL https://doi.org/10.1175/1520-0477(2001)082<2415:FANTTS>2.3.CO;2.

J. T. Ball, W. I. E, and B. J. A. A model predicting stomatal conductance and its contribution to the control of photosynthesis under different environmental conditions. In J. Biggins, editor, *Progress in Photosynthesis Research*, page 221224. Springer, Dordrecht, 1987.

M. K. Bartlett, T. Klein, S. Jansen, B. Choat, and L. Sack. The correlations and sequence of plant stomatal, hydraulic, and wilting responses to drought. *Proceedings of the National Academy of Sciences*, 113(46):13098–13103, 2016. doi: 10.1073/pnas.1604088113. URL http://www.pnas.org/content/113/46/13098.

A. Berg, J. Sheffield, and P. C. D. Milly. Divergent surface and total soil moisture projections under global warming. *Geophysical Research Letters*, 44(1):236–244, 2017. doi: 10.1002/2016GL071921.

G. Bohrer, H. Mourad, T. A. Laursen, D. Drewry, R. Avissar, D. Poggi, R. Oren, and G. G. Katul. Finite element tree crown hydrodynamics model (FETCH) using porous media flow within branching elements: A new representation of tree hydrodynamics. *Water Resources Research*, 41(11), 2005. doi: 10.1029/2005WR004181. URL https://agupubs.onlinelibrary.wiley.com/doi/abs/10.1029/2005WR004181.

G. B. Bonan. Forests and climate change: Forcings, feedbacks, and the climate benefits of forests. *Science*, 320(5882):1444–1449, 2008. ISSN 0036-8075. doi: 10.1126/science.1155121. URL http://science.sciencemag.org/content/320/5882/1444.

G. B. Bonan, P. J. Lawrence, K. W. Oleson, S. Levis, M. Jung, M. Reichstein, D. M. Lawrence, and S. C. Swenson. Improving canopy processes in the Community Land

Model version 4 (CLM4) using global flux fields empirically inferred from FLUXNET data. *Journal of Geophysical Research*, 116, 2011. doi: 10.1029/2010JG001593. URL http://dx.doi.org/10.1029/2010JG001593.

G. B. Bonan, M. Williams, R. A. Fisher, and K. W. Oleson. Modeling stomatal conductance in the earth system: linking leaf water-use efficiency and water transport along the soil-plant-atmosphere continuum. *Geoscientific Model Development*, 7(5):2193–2222, 2014. doi: 10.5194/gmd-7-2193-2014. URL https://www.geosci-model-dev.net/7/2193/2014/.

G. B. Bonan, D. L. Lombardozzi, W. R. Wieder, K. W. Oleson, D. M. Lawrence, F. M. Hoffman, and N. Collier. Model structure and climate data uncertainty in historical simulations of the terrestrial carbon cycle (18502014). *Global Biogeochemical Cycles*, 0 (ja), 2019. doi: 10.1029/2019GB006175. URL https://agupubs.onlinelibrary.wiley.com/doi/abs/10.1029/2019GB006175.

M. Bouda and J. E. Saiers. Dynamic effects of root system architecture improve root water uptake in 1-d process-based soil-root hydrodynamics. *Advances in Water Resources*, 110: 319 – 334, 2017. ISSN 0309-1708. doi: https://doi.org/10.1016/j.advwatres.2017.10.018. URL http://www.sciencedirect.com/science/article/pii/S0309170817304402.

J. S. Boyer. Leaf water potentials measured with a pressure chamber. *Plant Physiology*, 42(1):133–137, 1967. ISSN 0032-0889. doi: 10.1104/pp.42.1.133. URL http://www.plantphysiol.org/content/42/1/133.

T. J. Brodribb, N. M. Holbrook, E. J. Edwards, and M. V. Gutiérrez. Relations between stomatal closure, leaf turgor and xylem vulnerability in eight tropical dry forest trees. *Plant, Cell & Environment*, 26(3):443–450, 2003. doi: 10.1046/j.1365-3040.2003.00975.x. URL https://onlinelibrary.wiley.com/doi/abs/10.1046/j.1365-3040.2003.00975.x.

J. R. Brooks, F. C. Meinzer, J. M. Warren, J.-C. Domec, and R. Coulombe. Hydraulic redistribution in a Douglas-fir forest: lessons from system manipulations. *Plant, Cell & Environment*, 29(1):138–150, 2006. ISSN 1365-3040. doi: 10.1111/j.1365-3040.2005.01409.x. URL http://dx.doi.org/10.1111/j.1365-3040.2005.01409.x.

R. Brooks and A. Corey. *Hydraulic Properties of Porous Media*. Colorado State University Hydrology Papers. Colorado State University, 1964. URL https://books.google.com/books?id=F_1HOgAACAAJ.

S. S. O. Burgess, M. A. Adams, N. C. Turner, and C. K. Ong. The redistribution of soil water by tree root systems. *Oecologia*, 115(3):306–311, Jul 1998. ISSN 1432-1939. doi: 10.1007/s004420050521. URL https://doi.org/10.1007/s004420050521.

G. Cai, J. Vanderborght, M. Langensiepen, A. Schnepf, H. Hüging, and H. Vereecken. Root growth, water uptake, and sap flow of winter wheat in response to different soil water conditions. *Hydrology and Earth System Sciences*, 22(4):2449–2470, 2018. doi: 10.5194/hess-22-2449-2018. URL https://www.hydrol-earth-syst-sci.net/22/2449/2018/.

M. A. Celia, E. T. Bouloutas, and R. L. Zarba. A general mass-conservative numerical solution for the unsaturated flow equation. *Water Resources Research*, 26(7):1483–1496, 1990. ISSN 1944-7973. doi: 10.1029/WR026i007p01483.

B. Choat, S. Jansen, T. J. Brodribb, H. Cochard, S. Delzon, R. Bhaskar, S. J. Bucci, T. S. Feild, S. M. Gleason, U. G. Hacke, A. L. Jacobsen, F. Lens, H. Maherali, J. Martínez-Vilalta, S. Mayr, M. Mencuccini, P. J. Mitchell, A. Nardini, J. Pittermann, R. B. Pratt, J. S. Sperry, M. Westoby, I. J. Wright, and A. E. Zanne. Global convergence in the vulnerability of forests to drought. *Nature*, 491(7426):752–5, Nov 29 2012.

B. O. Christoffersen, M. Gloor, S. Fauset, N. M. Fyllas, D. R. Galbraith, T. R. Baker, B. Kruijt, L. Rowland, R. A. Fisher, O. J. Binks, S. Sevanto, C. Xu, S. Jansen, B. Choat, M. Mencuccini, N. G. McDowell, and P. Meir. Linking hydraulic traits to tropical forest function in a size-structured and trait-driven model (TFS v.1-Hydro). *Geoscientific Model Development*, 9(11):4227–4255, 2016. doi: 10.5194/gmd-9-4227-2016. URL `http://www.geosci-model-dev.net/9/4227/2016/`.

R. B. Clapp and G. M. Hornberger. Empirical equations for some soil hydraulic properties. *Water Resources Research*, 14(4):601–604, 1978. ISSN 1944-7973. doi: 10.1029/WR014i004p00601. URL `http://dx.doi.org/10.1029/WR014i004p00601`.

G. Collatz, J. Ball, C. Grivet, and J. A. Berry. Physiological and environmental regulation of stomatal conductance, photosynthesis and transpiration: a model that includes a laminar boundary layer. *Agricultural and Forest Meteorology*, 54(2):107 – 136, 1991. ISSN 0168-1923. doi: http://dx.doi.org/10.1016/0168-1923(91)90002-8. URL `http://www.sciencedirect.com/science/article/pii/0168192391900028`.

I. R. Cowan and G. Farquhar. Stomatal function in relation to leaf metabolism and environment. *Symposia of the Society for Experimental Biology*, 31:471–505, 02 1977.

P. M. Cox, D. Pearson, B. B. Booth, P. Friedlingstein, C. Huntingford, C. D. Jones, and C. M. Luke. Sensitivity of tropical carbon to climate change constrained by carbon dioxide variability. *Nature*, 494(7437):341–344, 2013. doi: 10.1038/nature11882.

A. C. da Costa, D. B. Metcalfe, C. E. Doughty, A. A. de Oliveira, G. F. Neto, M. C. da Costa, J. de Athaydes Silva Junior, L. E. Aragão, S. Almeida, D. R. Galbraith, L. M. Rowland, P. Meir, and Y. Malhi. Ecosystem respiration and net primary productivity after 8-10 years of experimental through-fall reduction in an eastern Amazon forest. *Plant Ecology & Diversity*, 7(1-2):7–24, 2014. doi: 10.1080/17550874.2013.798366.

A. C. L. da Costa, D. Galbraith, S. Almeida, B. Takeshi, T. Portela, M. da Costa, J. ao de Athaydes Silva Junior, A. P. Braga, P. H. L. de Gonçalves, A. A. de Oliveira, R. Fisher, O. L. Phillips, D. B. Metcalfe, P. Levy, and P. Meir. Effect of 7 yr of experimental drought on vegetation dynamics and biomass storage of an eastern Amazonian rainforest. *The New Phytologist*, 187(3):579–591, 2010. URL `http://www.jstor.org/stable/40792407`.

Y. Dai, R. E. Dickinson, and Y.-P. Wang. A two-big-leaf model for canopy temperature, photosynthesis, and stomatal conductance. *Journal of Climate*, 17(12):2281–2299, Jun 15 2004. doi: 10.1175/1520-0442(2004)017$\langle$2281:ATMFCT$\rangle$2.0.CO;2.

M. G. De Kauwe, J. Kala, Y.-S. Lin, A. J. Pitman, B. E. Medlyn, R. A. Duursma, G. Abramowitz, Y.-P. Wang, and D. G. Miralles. A test of an optimal stomatal conductance scheme within the CABLE land surface model. *Geoscientific Model Development*, 8(2):431–452, 2015. doi: 10.5194/gmd-8-431-2015. URL https://www.geosci-model-dev.net/8/431/2015/.

M. G. De Kauwe, B. E. Medlyn, J. Knauer, and C. A. Williams. Ideas and perspectives: how coupled is the vegetation to the boundary layer? *Biogeosciences*, 14(19):4435–4453, 2017. doi: 10.5194/bg-14-4435-2017. URL https://www.biogeosciences.net/14/4435/2017/.

S. Delzon and H. Cochard. Recent advances in tree hydraulics highlight the ecological significance of the hydraulic safety margin. *New Phytologist*, 203(2):355–358, 2014. doi: 10.1111/nph.12798. URL https://nph.onlinelibrary.wiley.com/doi/abs/10.1111/nph.12798.

S. Díaz and et al. The global spectrum of plant form and function. *Nature*, 529:167–171, 2015. doi: 10.1038/nature16489.

J.-C. Domec, J. S. King, A. Noormets, E. Treasure, M. J. Gavazzi, G. Sun, and S. G. McNulty. Hydraulic redistribution of soil water by roots affects whole-stand evapotranspiration and net ecosystem carbon exchange. *The New Phytologist*, 187(1):171–183, 2010. ISSN 0028646X, 14698137. doi: 10.1111/j.1469-8137.2010.03245.x. URL http://www.jstor.org/stable/40661500.

L. A. Donovan, J. H. Richards, and M. J. Linton. Magnitude and mechanisms of disequilibrium between predawn plant and soil water potentials. *Ecology*, 84(2):463–470, 2003.

J. Drake, S. Power, R. Duursma, B. Medlyn, M. Aspinwall, B. Choat, D. Creek, D. Eamus, C. Maier, S. Pfautsch, R. Smith, M. Tjoelker, and D. Tissue. Stomatal and non-stomatal limitations of photosynthesis for four tree species under drought: A comparison of model formulations. *Agricultural and Forest Meteorology*, 247:454 – 466, 2017. ISSN 0168-1923. doi: https://doi.org/10.1016/j.agrformet.2017.08.026. URL http://www.sciencedirect.com/science/article/pii/S0168192317302824.

G. Egea, A. Verhoef, and P. L. Vidale. Towards an improved and more flexible representation of water stress in coupled photosynthesis-stomatal conductance models. *Agricultural and Forest Meteorology*, 151(10):1370 – 1384, 2011. ISSN 0168-1923. doi: https://doi.org/10.1016/j.agrformet.2011.05.019. URL http://www.sciencedirect.com/science/article/pii/S0168192311001778.

J. Epila, N. J. De Baerdemaeker, L. L. Vergeynst, W. H. Maes, H. Beeckman, and K. Steppe. Capacitive water release and internal leaf water relocation delay drought-induced cavitation in African Maesopsis eminii. *Tree Physiology*, 37(4):481–490, 2017. doi: 10.1093/treephys/tpw128. URL http://dx.doi.org/10.1093/treephys/tpw128.

G. D. Farquhar, S. von Caemmerer, and J. A. Berry. A biochemical model of photosynthetic CO_2 assimilation in leaves of C_3 species. *Planta*, 149(1):78–90, 1980. ISSN 00320935, 14322048. doi: 10.1007/BF00386231. URL http://www.jstor.org/stable/23374770.

S. Fatichi, C. Pappas, and V. Y. Ivanov. Modeling plant-water interactions: an ecohydrological overview from the cell to the global scale. *Wiley Interdisciplinary Reviews: Water*, 3(3):327–368, 2016. doi: 10.1002/wat2.1125. URL https://onlinelibrary.wiley.com/doi/abs/10.1002/wat2.1125.

X. Feng, D. D. Ackerly, T. E. Dawson, S. Manzoni, R. P. Skelton, G. Vico, and S. E. Thompson. The ecohydrological context of drought and classification of plant responses. *Ecology Letters*, 21(11):1723–1736, 2018. doi: 10.1111/ele.13139. URL https://onlinelibrary.wiley.com/doi/abs/10.1111/ele.13139.

X. Feng, D. D. Ackerly, T. E. Dawson, S. Manzoni, B. McLaughlin, R. P. Skelton, G. Vico, A. P. Weitz, and S. E. Thompson. Beyond isohydricity: The role of environmental variability in determining plant drought responses. *Plant, Cell & Environment*, 42(4):1104–1111, 2019. doi: 10.1111/pce.13486. URL https://onlinelibrary.wiley.com/doi/abs/10.1111/pce.13486.

D. L. Ficklin and K. A. Novick. Historic and projected changes in vapor pressure deficit suggest a continental-scale drying of the United States atmosphere. *Journal of Geophysical Research: Atmospheres*, 122(4):2061–2079, 2017. doi: 10.1002/2016JD025855. URL https://agupubs.onlinelibrary.wiley.com/doi/abs/10.1002/2016JD025855.

R. A. Fisher, M. Williams, R. L. Do Vale, A. L. Da Costa, and P. Meir. Evidence from Amazonian forests is consistent with isohydric control of leaf water potential. *Plant, Cell & Environment*, 29(2):151–165, 2006. ISSN 1365-3040. doi: 10.1111/j.1365-3040.2005.01407.x. URL http://dx.doi.org/10.1111/j.1365-3040.2005.01407.x.

R. A. Fisher, M. Williams, A. L. D. Costa, Y. Malhi, R. F. D. Costa, S. Almeida, and P. Meir. The response of an Eastern Amazonian rain forest to drought stress: results and modelling analyses from a throughfall exclusion experiment. *Global Change Biology*, 13(11):2361–2378, 2007. doi: 10.1111/j.1365-2486.2007.01417.x. URL https://onlinelibrary.wiley.com/doi/abs/10.1111/j.1365-2486.2007.01417.x.

R. A. Fisher, M. Williams, M. de Lourdes Ruivo, A. L. de Costa, and P. Meir. Evaluating climatic and soil water controls on evapotranspiration at two Amazonian rainforest sites. *Agricultural and Forest Meteorology*, 148(6):850 – 861, 2008. ISSN 0168-1923. doi: https://doi.org/10.1016/j.agrformet.2007.12.001. URL http://www.sciencedirect.com/science/article/pii/S0168192307003036.

R. A. Fisher, W. R. Wieder, B. M. Sanderson, C. D. Koven, K. W. Oleson, C. Xu, J. B. Fisher, M. Shi, A. P. Walker, and D. M. Lawrence. Parametric controls on vegetation responses to biogeochemical forcing in the clm5. *Journal of Advances in Modeling Earth Systems*, 0(0), 2019. doi: 10.1029/2019MS001609. URL https://agupubs.onlinelibrary.wiley.com/doi/abs/10.1029/2019MS001609.

J. Flexas, J. Bota, F. Loreto, G. Cornic, and T. D. Sharkey. Diffusive and metabolic limitations to photosynthesis under drought and salinity in C3 plants. *Plant Biology*, 6(3):269–279, 2004. doi: 10.1055/s-2004-820867. URL https://onlinelibrary.wiley.com/doi/abs/10.1055/s-2004-820867.

J. Flexas, M. M. Barbour, O. Brendel, H. M. Cabrera, M. Carriquí, A. Díaz-Espejo, C. Douthe, E. Dreyer, J. P. Ferrio, J. Gago, A. Gallé, J. Galmés, N. Kodama, H. Medrano, Ü. Niinemets, J. J. Peguero-Pina, A. Pou, M. Ribas-Carbó, M. Tomás, T. Tosens, and C. R. Warren. Mesophyll diffusion conductance to CO2: An unappreciated central player in photosynthesis. *Plant Science*, 193-194:70 – 84, 2012. ISSN 0168-9452. doi: https://doi.org/10.1016/j.plantsci.2012.05.009. URL http://www.sciencedirect.com/science/article/pii/S0168945212001069.

P. J. Franks, G. B. Bonan, J. A. Berry, D. L. Lombardozzi, N. M. Holbrook, N. Herold, and K. W. Oleson. Comparing optimal and empirical stomatal conductance models for application in Earth system models. *Global Change Biology*, 24(12):5708–5723, 2018. doi: 10.1111/gcb.14445.

P. Friedlingstein, M. Meinshausen, V. K. Arora, C. D. Jones, A. Anav, S. K. Liddicoat, and R. Knutti. Uncertainties in CMIP5 climate projections due to carbon cycle feedbacks. *Journal of Climate*, 27(2):511–526, Jan 15 2014. URL http://ezproxy.cul.columbia.edu/login?url=https://search.proquest.com/docview/1495899892?accountid=10226.

R. Fu, L. Yin, W. Li, P. A. Arias, R. E. Dickinson, L. Huang, S. Chakraborty, K. Fernandes, B. Liebmann, R. Fisher, and R. B. Myneni. Increased dry-season length over southern Amazonia in recent decades and its implication for future climate projection. *Proceedings of the National Academy of Sciences of the United States of America*, 110(45):18110–18115, 2013. ISSN 00278424. URL http://www.jstor.org/stable/23754710.

X. Fu and F. C. Meinzer. Metrics and proxies for stringency of regulation of plant water status (iso/anisohydry): a global data set reveals coordination and trade-offs among water transport traits. *Tree Physiology*, 39(1):122–134, 09 2018. ISSN 1758-4469. doi: 10.1093/treephys/tpy087. URL https://doi.org/10.1093/treephys/tpy087.

N. Garcia-Forner, C. Biel, R. Sav, and J. Martnez-Vilalta. Isohydric species are not necessarily more carbon limited than anisohydric species during drought. *Tree Physiology*, 37 (4):441–455, 2017. doi: 10.1093/treephys/tpw109.

P. Gentine, D. Entekhabi, A. Chehbouni, G. Boulet, and B. Duchemin. Analysis of evaporative fraction diurnal behaviour. *Agricultural and Forest Meteorology*, 143(1):13 – 29, 2007. ISSN 0168-1923. doi: https://doi.org/10.1016/j.agrformet.2006.11.002. URL http://www.sciencedirect.com/science/article/pii/S016819230600339X.

P. Gentine, D. Entekhabi, and J. Polcher. The diurnal behavior of evaporative fraction in the soil-vegetation-atmospheric boundary layer continuum. *Journal of Hydrometeorology*, 12(6):1530–1546, 2011. doi: 10.1175/2011JHM1261.1. URL https://doi.org/10.1175/2011JHM1261.1.

P. Gentine, M. Guérin, M. Uriarte, N. G. McDowell, and W. T. Pockman. An allometry-based model of the survival strategies of hydraulic failure and carbon starvation. *Ecohydrology*, 9(3):529–546, 2016. ISSN 1936-0592. doi: 10.1002/eco.1654. URL http://dx.doi.org/10.1002/eco.1654.

F. Giardina, A. G. Konings, D. Kennedy, S. H. Alemohammad, R. S. Oliveira, M. Uriarte, and P. Gentine. Tall Amazonian forests are less sensitive to precipitation variability. *Nature Geoscience*, 11(6):405–409, 2018. doi: 10.1038/s41561-018-0133-5.

J. Grant, J.-P. Wigneron, R. D. Jeu, H. Lawrence, A. Mialon, P. Richaume, A. A. Bitar, M. Drusch, M. van Marle, and Y. Kerr. Comparison of SMOS and AMSR-E vegetation optical depth to four MODIS-based vegetation indices. *Remote Sensing of Environment*, 172:87 – 100, 2016. ISSN 0034-4257. doi: https://doi.org/10.1016/j.rse.2015.10.021. URL `http://www.sciencedirect.com/science/article/pii/S0034425715301735`.

H. D. Graven, R. F. Keeling, S. C. Piper, P. K. Patra, B. B. Stephens, S. C. Wofsy, L. R. Welp, C. Sweeney, P. P. Tans, J. J. Kelley, B. C. Daube, E. A. Kort, G. W. Santoni, and J. D. Bent. Enhanced seasonal exchange of CO_2 by northern ecosystems since 1960. *Science*, 341(6150):1085–1089, 2013. ISSN 0036-8075. doi: 10.1126/science.1239207. URL `https://science.sciencemag.org/content/341/6150/1085`.

J. K. Green, A. G. Konings, S. H. Alemohammad, J. Berry, D. Entekhabi, J. Kolassa, J.-E. Lee, and P. Gentine. Regionally strong feedbacks between the atmosphere and terrestrial biosphere. *Nature Geoscience*, 10(6):410–414, 2017. doi: 10.1038/ngeo2957.

J. K. Green, S. I. Seneviratne, A. M. Berg, K. L. Findell, S. Hagemann, D. M. Lawrence, and P. Gentine. Large influence of soil moisture on long-term terrestrial carbon uptake. *Nature*, 565(7740):476–479, 2019. doi: 10.1038/s41586-018-0848-x.

P. C. Harley, R. B. Thomas, J. F. Reynolds, and B. R. Strain. Modelling photosynthesis of cotton grown in elevated CO2. *Plant Cell Environment*, 15(3):271–282, 1992. doi: 10.1111/j.1365-3040.1992.tb00974.x.

U. Hochberg, F. E. Rockwell, N. M. Holbrook, and H. Cochard. Iso/anisohydry: A plant-environment interaction rather than a simple hydraulic trait. *Trends in Plant Science*, 23 (2):112–120, 2018. doi: 10.1016/j.tplants.2017.11.002.

N. M. Holbrook, E. T. Ahrens, M. J. Burns, and M. A. Zwieniecki. In vivo observation of cavitation and embolism repair using magnetic resonance imaging. *Plant Physiology*, 126(1):27–31, 2001. ISSN 0032-0889. doi: 10.1104/pp.126.1.27. URL `http://www.plantphysiol.org/content/126/1/27`.

V. Humphrey, J. Zscheischler, P. Ciais, L. Gudmundsson, S. Sitch, and S. I. Seneviratne. Sensitivity of atmospheric CO_2 growth rate to observed changes in terrestrial water storage. *Nature*, 560(7720):628–631, 2018. doi: 10.1038/s41586-018-0424-4.

C. Huntingford, P. Zelazowski, D. Galbraith, L. M. Mercado, S. Sitch, R. Fisher, M. Lomas, A. P. Walker, C. D. Jones, B. B. B. Booth, Y. Malhi, D. Hemming, G. Kay, P. Good, S. L. Lewis, O. L. Phillips, O. K. Atkin, J. Lloyd, E. Gloor, J. Zaragoza-castells, P. Meir, R. Betts, P. P. Harris, C. Nobre, J. Marengo, and P. M. Cox. Simulated resilience of tropical rainforests to CO2-induced climate change. *Nature Geoscience*, 6(4):268–273, 04 2013.

R. B. Jackson, J. Canadell, J. R. Ehleringer, H. A. Mooney, O. E. Sala, and E. D. Schulze. A global analysis of root distributions for terrestrial biomes. *Oecologia*, 108(3):389–411, Nov 1996. ISSN 1432-1939. doi: 10.1007/BF00333714.

R. B. Jackson, J. S. Sperry, and T. E. Dawson. Root water uptake and transport: using physiological processes in global predictions. *Trends in Plant Science*, 5(11):482 – 488, 2000. ISSN 1360-1385. doi: https://doi.org/10.1016/S1360-1385(00)01766-0. URL http://www.sciencedirect.com/science/article/pii/S1360138500017660.

N. J. Jarvis. Simple physics-based models of compensatory plant water uptake: concepts and eco-hydrological consequences. *Hydrology and Earth System Sciences*, 15(11):3431–3446, 2011. doi: 10.5194/hess-15-3431-2011. URL https://www.hydrol-earth-syst-sci.net/15/3431/2011/.

P. G. Jarvis. The interpretation of the variations in leaf water potential and stomatal conductance found in canopies in the field. *Philosophical Transactions of the Royal Society of London. Series B, Biological Sciences*, 273(927):593–610, 1976. URL http://www.jstor.org/stable/2417554.

M. Javaux, V. Couvreur, J. Vanderborght, and H. Vereecken. Root Water Uptake: From Three-Dimensional Biophysical Processes to Macroscopic Modeling Approaches. *Vadose Zone Journal*, 12(4), 11 2013. ISSN 1539-1663. doi: 10.2136/vzj2013.02.0042. URL https://doi.org/10.2136/vzj2013.02.0042. vzj2013.02.0042.

E. Joetzjer, C. Delire, H. Douville, P. Ciais, B. Decharme, R. Fisher, B. Christoffersen, J. C. Calvet, A. C. L. da Costa, L. V. Ferreira, and P. Meir. Predicting the response of the Amazon rainforest to persistent drought conditions under current and future climates: a major challenge for global land surface models. *Geoscientific Model Development*, 7(6):2933–2950, 2014. doi: 10.5194/gmd-7-2933-2014. URL https://www.geosci-model-dev.net/7/2933/2014/.

J. Kattge, S. Díaz, S. Lavorel, I. C. Prentice, and et al. TRY - a global database of plant traits. *Global Change Biology*, 17(9):2905–2935, 2011. ISSN 1365-2486. doi: 10.1111/j.1365-2486.2011.02451.x. URL http://dx.doi.org/10.1111/j.1365-2486.2011.02451.x.

C. D. Keeling. The concentration and isotopic abundances of carbon dioxide in the atmosphere. *Tellus*, 12(2):200–203, 1960. doi: 10.1111/j.2153-3490.1960.tb01300.x. URL https://onlinelibrary.wiley.com/doi/abs/10.1111/j.2153-3490.1960.tb01300.x.

T. Keenan and C. Williams. The terrestrial carbon sink. *Annual Review of Environment and Resources*, 43(1):219–243, 2018. doi: 10.1146/annurev-environ-102017-030204. URL https://doi.org/10.1146/annurev-environ-102017-030204.

T. Keenan, I. Baker, A. Barr, P. Ciais, K. Davis, M. Dietze, D. Dragoni, C. M. Gough, R. Grant, D. Hollinger, K. Hufkens, B. Poulter, H. McCaughey, B. Raczka, Y. Ryu, K. Schaefer, H. Tian, H. Verbeeck, M. Zhao, and A. D. Richardson. Terrestrial biosphere

model performance for inter-annual variability of land-atmosphere CO2 exchange. *Global Change Biology*, 18(6):1971–1987, 2012. doi: 10.1111/j.1365-2486.2012.02678.x. URL https://onlinelibrary.wiley.com/doi/abs/10.1111/j.1365-2486.2012.02678.x.

D. Kennedy, S. C. Swenson, K. W. Oleson, D. M. Lawrence, R. A. Fisher, A. C. Lola da Costa, and P. Gentine. Implementing plant hydraulics in the Community Land Model, version 5. *Journal of Advances in Modeling Earth Systems*, 11(2):485–513, 2019. doi: 10.1029/2018MS001500.

T. Klein and S. Niu. The variability of stomatal sensitivity to leaf water potential across tree species indicates a continuum between isohydric and anisohydric behaviours. *Functional Ecology*, 28(6):1313–1320, 2014. doi: 10.1111/1365-2435.12289. URL https://besjournals.onlinelibrary.wiley.com/doi/abs/10.1111/1365-2435.12289.

A. G. Konings and P. Gentine. Global variations in ecosystem-scale isohydricity. *Global Change Biology*, 23(2):891–905, 2017. ISSN 1365-2486. doi: 10.1111/gcb.13389. URL http://dx.doi.org/10.1111/gcb.13389.

A. G. Konings, M. Piles, K. Rötzer, K. A. McColl, S. K. Chan, and D. Entekhabi. Vegetation optical depth and scattering albedo retrieval using time series of dual-polarized l-band radiometer observations. *Remote Sensing of Environment*, 172:178 – 189, 2016. ISSN 0034-4257. doi: https://doi.org/10.1016/j.rse.2015.11.009. URL http://www.sciencedirect.com/science/article/pii/S003442571530198X.

A. G. Konings, A. P. Williams, and P. Gentine. Sensitivity of grassland productivity to aridity controlled by stomatal and xylem regulation. *Nature Geoscience*, 10(4):284–288, 2017. doi: 10.1038/ngeo2903.

M. M. Kotowska, D. Hertel, Y. A. Rajab, H. Barus, and B. Schuldt. Patterns in hydraulic architecture from roots to branches in six tropical tree species from cacao agroforestry and their relation to wood density and stem growth. *Frontiers in Plant Science*, 6:191, 2015. ISSN 1664-462X. doi: 10.3389/fpls.2015.00191. URL https://www.frontiersin.org/article/10.3389/fpls.2015.00191.

S. Kumar, M. Newman, Y. Wang, and B. Livneh. Potential reemergence of seasonal soil moisture anomalies in North America. *Journal of Climate*, 0(0):null, 2019. doi: 10.1175/JCLI-D-18-0540.1.

D. M. Lawrence, et al., and et al. The Community Land Model version 5: Description of new features, benchmarking, and impact of forcing uncertainty. *Journal of Advances in Modeling Earth Systems*, in press, 2019. doi: 10.1029/2018MS001583.

C. Le Quéré, R. M. Andrew, P. Friedlingstein, S. Sitch, J. Pongratz, A. C. Manning, J. I. Korsbakken, G. P. Peters, J. G. Canadell, R. B. Jackson, T. A. Boden, P. P. Tans, O. D. Andrews, V. K. Arora, D. C. E. Bakker, L. Barbero, M. Becker, R. A. Betts, L. Bopp, F. Chevallier, L. P. Chini, P. Ciais, C. E. Cosca, J. Cross, K. Currie, T. Gasser, I. Harris, J. Hauck, V. Haverd, R. A. Houghton, C. W. Hunt, G. Hurtt, T. Ilyina, A. K. Jain, E. Kato, M. Kautz, R. F. Keeling, K. Klein Goldewijk, A. Körtzinger, P. Landschützer,

N. Lefèvre, A. Lenton, S. Lienert, I. Lima, D. Lombardozzi, N. Metzl, F. Millero, P. M. S. Monteiro, D. R. Munro, J. E. M. S. Nabel, S.-I. Nakaoka, Y. Nojiri, X. A. Padin, A. Peregon, B. Pfeil, D. Pierrot, B. Poulter, G. Rehder, J. Reimer, C. Rödenbeck, J. Schwinger, R. Séférian, I. Skjelvan, B. D. Stocker, H. Tian, B. Tilbrook, F. N. Tubiello, I. T. van der Laan-Luijkx, G. R. van der Werf, S. van Heuven, N. Viovy, N. Vuichard, A. P. Walker, A. J. Watson, A. J. Wiltshire, S. Zaehle, and D. Zhu. Global carbon budget 2017. *Earth System Science Data*, 10(1):405–448, 2018. doi: 10.5194/essd-10-405-2018. URL `https://www.earth-syst-sci-data.net/10/405/2018/`.

J.-E. Lee, R. S. Oliveira, T. E. Dawson, and I. Fung. Root functioning modifies seasonal climate. *Proceedings of the National Academy of Sciences of the United States of America*, 102(49):17576–17581, 2005. ISSN 00278424. doi: 10.1073/pnas.0508785102. URL `http://www.jstor.org/stable/4152769`.

L. Lemordant, P. Gentine, A. S. Swann, B. I. Cook, and J. Scheff. Critical impact of vegetation physiology on the continental hydrologic cycle in response to increasing CO2. *Proceedings of the National Academy of Sciences*, 2018. ISSN 0027-8424. doi: 10.1073/pnas.1720712115. URL `http://www.pnas.org/content/early/2018/03/29/1720712115`.

X. Li, B. J. Chris, J. M. R. Peters, B. Choat, P. D. Rymer, B. E. Medlyn, and D. T. Tissue. More than iso/anisohydry: Hydroscapes integrate plant water-use and drought tolerance traits in ten eucalypt species from contrasting climates. *Functional Ecology*, 0(0), 2019. doi: 10.1111/1365-2435.13320.

Y. Li, K. Guan, P. Gentine, A. G. Konings, F. C. Meinzer, J. S. Kimball, X. Xu, W. R. L. Anderegg, N. G. McDowell, J. Martinez-Vilalta, D. G. Long, and S. P. Good. Estimating global ecosystem isohydry/anisohydry using active and passive microwave satellite data. *Journal of Geophysical Research: Biogeosciences*, 122(12):3306–3321, 2017. doi: 10.1002/2017JG003958.

C. Lin, P. Gentine, Y. Huang, K. Guan, H. Kimm, and S. Zhou. Diel ecosystem conductance response to vapor pressure deficit is suboptimal and independent of soil moisture. *Agricultural and Forest Meteorology*, 250-251:24 – 34, 2018. ISSN 0168-1923. doi: https://doi.org/10.1016/j.agrformet.2017.12.078. URL `http://www.sciencedirect.com/science/article/pii/S0168192317304884`.

H. Liu, S. M. Gleason, G. Hao, L. Hua, P. He, G. Goldstein, and Q. Ye. Hydraulic traits are coordinated with maximum plant height at the global scale. *Science Advances*, 5(2), 2019. doi: 10.1126/sciadv.aav1332. URL `https://advances.sciencemag.org/content/5/2/eaav1332`.

D. S. Mackay, D. E. Roberts, B. E. Ewers, J. S. Sperry, N. G. McDowell, and W. T. Pockman. Interdependence of chronic hydraulic dysfunction and canopy processes can improve integrated models of tree response to drought. *Water Resources Research*, 51(8):6156–6176, 2015. ISSN 1944-7973. doi: 10.1002/2015WR017244. URL `http://dx.doi.org/10.1002/2015WR017244`.

S. Manzoni, G. Vico, G. Katul, S. Palmroth, R. B. Jackson, and A. Porporato. Hydraulic limits on maximum plant transpiration and the emergence of the safety-efficiency trade-off. *New Phytologist*, 198(1):169–178, 2013a. ISSN 1469-8137. doi: 10.1111/nph.12126. URL http://dx.doi.org/10.1111/nph.12126.

S. Manzoni, G. Vico, S. Palmroth, A. Porporato, and G. Katul. Optimization of stomatal conductance for maximum carbon gain under dynamic soil moisture. *Advances in Water Resources*, 62:90 – 105, 2013b. ISSN 0309-1708. doi: https://doi.org/10.1016/j.advwatres.2013.09.020. URL http://www.sciencedirect.com/science/article/pii/S0309170813001814.

J. Martínez-Vilalta and N. Garcia-Forner. Water potential regulation, stomatal behaviour and hydraulic transport under drought: deconstructing the iso/anisohydric concept. *Plant, Cell & Environment*, 40(6):962–976, 2017. doi: 10.1111/pce.12846.

J. Martínez-Vilalta, R. Poyatos, D. Aguadé, J. Retana, and M. Mencuccini. A new look at water transport regulation in plants. *New Phytologist*, 204(1):105–115, 2014. doi: 10.1111/nph.12912.

N. McDowell, C. D. Allen, K. Anderson-Teixeira, P. Brando, R. Brienen, J. Chambers, B. Christoffersen, S. Davies, C. Doughty, A. Duque, F. Espirito-Santo, R. Fisher, C. G. Fontes, D. Galbraith, D. Goodsman, C. Grossiord, H. Hartmann, J. Holm, D. J. Johnson, A. R. Kassim, M. Keller, C. Koven, L. Kueppers, T. Kumagai, Y. Malhi, S. M. McMahon, M. Mencuccini, P. Meir, P. Moorcroft, M.-L. H. C., O. L. Phillips, T. Powell, C. A. Sierra, J. Sperry, J. Warren, C. Xu, and X. Xu. Drivers and mechanisms of tree mortality in moist tropical forests. *New Phytologist*, 219(3):851–869, 2018. doi: 10.1111/nph.15027. URL https://nph.onlinelibrary.wiley.com/doi/abs/10.1111/nph.15027.

N. G. McDowell and C. D. Allen. Darcy's law predicts widespread forest mortality under climate warming. *Nature Climate Change*, 5(7):669–672, 07 2015. URL http://ezproxy.cul.columbia.edu/login?url=https://search.proquest.com/docview/1766270805?accountid=10226.

N. G. McDowell, A. P. Williams, C. Xu, W. T. Pockman, L. T. Dickman, S. Sevanto, R. Pangle, J. Limousin, J. Plaut, D. S. Mackay, J. Ogee, J. C. Domec, C. D. Allen, R. A. Fisher, X. Jiang, J. D. Muss, D. D. Breshears, S. A. Rauscher, and C. Koven. Multi-scale predictions of massive conifer mortality due to chronic temperature rise. *Nature Climate Change*, 6:295–300, 2016. doi: 10.1038/nclimate2873. URL http://www.nature.com/nclimate/journal/v6/n3/abs/nclimate2873.html.

B. E. Medlyn, R. A. Duursma, D. Eamus, D. S. Ellsworth, I. C. Prentice, C. V. M. Barton, K. Y. Crous, P. De Angelis, M. Freeman, and L. Wingate. Reconciling the optimal and empirical approaches to modelling stomatal conductance. *Global Change Biology*, 17(6):2134–2144, 2011. ISSN 1365-2486. doi: 10.1111/j.1365-2486.2010.02375.x. URL http://dx.doi.org/10.1111/j.1365-2486.2010.02375.x.

F. C. Meinzer, D. M. Johnson, B. Lachenbruch, K. A. McCulloh, and D. R. Woodruff. Xylem hydraulic safety margins in woody plants: coordination of stomatal control of

xylem tension with hydraulic capacitance. *Functional Ecology*, 23(5):922–930, 2009. ISSN 1365-2435. doi: 10.1111/j.1365-2435.2009.01577.x.

F. C. Meinzer, D. R. Woodruff, D. E. Marias, D. D. Smith, K. A. McCulloh, A. R. Howard, and A. L. Magedman. Mapping 'hydroscapes' along the iso- to anisohydric continuum of stomatal regulation of plant water status. *Ecology Letters*, 19(11):1343–1352, 2016. doi: 10.1111/ele.12670. URL https://onlinelibrary.wiley.com/doi/abs/10.1111/ele.12670.

M. Mencuccini, F. Minunno, Y. Salmon, J. Martínez-Vilalta, and T. H oltt a. Coordination of physiological traits involved in drought-induced mortality of woody plants. *New Phytologist*, 208(2):396–409, 2015. doi: 10.1111/nph.13461. URL https://nph.onlinelibrary.wiley.com/doi/abs/10.1111/nph.13461.

M. Mencuccini, S. Manzoni, and B. Christoffersen. Modelling water fluxes in plants: from tissues to biosphere. *New Phytologist*, 222(3):1207–1222, 2019. doi: 10.1111/nph.15681. URL https://nph.onlinelibrary.wiley.com/doi/abs/10.1111/nph.15681.

M. Momen, J. D. Wood, K. A. Novick, R. Pangle, W. T. Pockman, N. G. McDowell, and A. G. Konings. Interacting effects of leaf water potential and biomass on vegetation optical depth. *Journal of Geophysical Research: Biogeosciences*, 122(11):3031–3046, 2017. ISSN 2169-8961. doi: 10.1002/2017JG004145. URL http://dx.doi.org/10.1002/2017JG004145.

A. Mrad. A dynamic optimality principle for water use strategies explains isohydric to anisohydric plant responses to drought. *Frontiers*, 2019.

A. Nardini and J. Luglio. Leaf hydraulic capacity and drought vulnerability: possible trade-offs and correlations with climate across three major biomes. *Functional Ecology*, 28(4):810–818, 2014. doi: 10.1111/1365-2435.12246. URL https://besjournals.onlinelibrary.wiley.com/doi/abs/10.1111/1365-2435.12246.

A. Nardini, V. Casolo, A. Dal Borgo, T. Savi, B. Stenni, P. Bertoncin, L. Zini, and N. G. McDowell. Rooting depth, water relations and non-structural carbohydrate dynamics in three woody angiosperms differentially affected by an extreme summer drought. *Plant, Cell & Environment*, 39(3):618–627, 2016. doi: 10.1111/pce.12646.

D. C. Nepstad, R. de Carvalho, Claudio, E. A. Davidson, P. H. Jipp, P. A. Lefebvre, G. H. Negreiros, E. D. da Silva, T. A. Stone, S. E. Trumbore, and S. Vieira. The role of deep roots in the hydrological and carbon cycles of Amazonian forests and pastures. *Nature*, 372 (6507):666, Dec 15 1994. URL http://ezproxy.cul.columbia.edu/login?url=https://search.proquest.com/docview/204448824?accountid=10226.

K. A. Novick, D. L. Ficklin, P. C. Stoy, C. A. Williams, G. Bohrer, A. Oishi, S. A. Papuga, P. D. Blanken, A. Noormets, B. N. Sulman, R. L. Scott, L. Wang, and R. P. Phillips. The increasing importance of atmospheric demand for ecosystem water and carbon fluxes. *Nature Climate Change*, 6(11):1023–1027, 11 2016a.

K. A. Novick, C. F. Miniat, and J. M. Vose. Drought limitations to leaf-level gas exchange: results from a model linking stomatal optimization and cohesion-tension theory. *Plant, Cell & Environment*, 39(3):583–596, 2016b. ISSN 1365-3040. doi: 10.1111/pce.12657.

K. A. Novick, A. G. Konings, and P. Gentine. Beyond soil water potential: An expanded view on isohydricity including land-atmosphere interactions and phenology. *Plant, Cell & Environment*, 0(0), 2019. doi: 10.1111/pce.13517. URL `https://onlinelibrary.wiley.com/doi/abs/10.1111/pce.13517`.

K. W. Oleson, D. M. Lawrence, G. B. Bonan, B. Drewniak, M. Huang, C. D. Koven, S. Levis, F. Li, W. J. Riley, Z. M. Subin, S. C. Swenson, P. E. Thornton, A. Bozbiyik, R. Fisher, C. L. Heald, E. Kluzek, J.-F. Lamarque, P. J. Lawrence, L. R. Leung, W. Lipscomb, S. Muszala, D. M. Ricciuto, W. Sacks, Y. Sun, J. Tang, and Z.-L. Yang. Technical description of version 4.5 of the Community Land Model (CLM), NCAR Tech. Note NCAR/TN-503+STR. *National Center for Atmospheric Research, Boulder, Colorado, 420 pp.*, 2013. doi: 10.5065/D6RR1W7M. URL `http://opensky.ucar.edu/islandora/object/technotes:515`.

R. S. Oliveira, T. E. Dawson, S. S. O. Burgess, and D. C. Nepstad. Hydraulic redistribution in three amazonian trees. *Oecologia*, 145(3):354–363, 2005. ISSN 00298549, 14321939. doi: 10.1007/s00442-005-0108-2. URL `http://www.jstor.org/stable/20062426`.

A. G. Pendergrass, R. Knutti, F. Lehner, C. Deser, and B. M. Sanderson. Precipitation variability increases in a warmer climate. *Scientific Reports*, 7:1, 2017.

A. L. Pivovaroff, V. M. Cook, and L. S. Santiago. Stomatal behaviour and stem xylem traits are coordinated for woody plant species under exceptional drought conditions. *Plant, Cell & Environment*, 41(11):2617–2626, 2018. doi: 10.1111/pce.13367. URL `https://onlinelibrary.wiley.com/doi/abs/10.1111/pce.13367`.

A. Porporato, F. Laio, L. Ridolfi, and I. Rodriguez-Iturbe. Plants in water-controlled ecosystems: active role in hydrologic processes and response to water stress: III. Vegetation water stress. *Advances in Water Resources*, 24(7):725 – 744, 2001. ISSN 0309-1708. doi: https://doi.org/10.1016/S0309-1708(01)00006-9.

B. Poulter, D. Frank, P. Ciais, R. B. Myneni, N. Andela, J. Bi, G. Broquet, J. G. Canadell, F. Chevallier, Y. Y. Liu, S. W. Running, S. Sitch, and G. R. van der Werf. Contribution of semi-arid ecosystems to interannual variability of the global carbon cycle. *Nature*, 509: 600–603, 2014. doi: 10.1038/nature13376.

T. L. Powell, D. R. Galbraith, B. O. Christoffersen, A. Harper, H. M. A. Imbuzeiro, L. Rowland, S. Almeida, P. M. Brando, A. C. L. da Costa, M. H. Costa, N. M. Levine, Y. Malhi, S. R. Saleska, E. Sotta, M. Williams, P. Meir, and P. R. Moorcroft. Confronting model predictions of carbon fluxes with measurements of amazon forests subjected to experimental drought. *New Phytologist*, 200(2):350–365, 2013. ISSN 1469-8137. doi: 10.1111/nph.12390.

T. L. Powell, W. J. K., O. A. A. R., C. A. C. Lola, S. S. R., M. Patrick, and M. P. R. Differences in xylem and leaf hydraulic traits explain differences in drought tolerance

among mature amazon rainforest trees. *Global Change Biology*, 23(10):4280–4293, 2018. doi: 10.1111/gcb.13731. URL https://onlinelibrary.wiley.com/doi/abs/10.1111/gcb.13731.

M. M. Rahman, M. Lu, and K. H. Kyi. Variability of soil moisture memory for wet and dry basins. *Journal of Hydrology*, 523:107 – 118, 2015. ISSN 0022-1694. doi: https://doi.org/10.1016/j.jhydrol.2015.01.033. URL http://www.sciencedirect.com/science/article/pii/S0022169415000505.

G. Ratzmann, F. C. Meinzer, and B. Tietjen. Iso/anisohydry: Still a useful concept. *Trends in Plant Science*, 24(3):191–194, 2019. doi: 10.1016/j.tplants.2019.01.001.

C. M. Restaino, D. L. Peterson, and J. Littell. Increased water deficit decreases Douglas fir growth throughout western US forests. *Proceedings of the National Academy of Sciences*, 113(34):9557–9562, 2016. ISSN 0027-8424. doi: 10.1073/pnas.1602384113. URL http://www.pnas.org/content/113/34/9557.

N. Restrepo-Coupe, N. M. Levine, B. O. Christoffersen, L. P. Albert, J. Wu, M. H. Costa, D. Galbraith, H. Imbuzeiro, G. Martins, A. C. da Araujo, Y. S. Malhi, X. Zeng, P. Moorcroft, and S. R. Saleska. Do dynamic global vegetation models capture the seasonality of carbon fluxes in the amazon basin? A data-model intercomparison. *Global Change Biology*, 23(1):191–208, 2017. ISSN 1365-2486. doi: 10.1111/gcb.13442.

J. S. Rice and R. E. Emanuel. Ecohydrology of interannual changes in watershed storage. *Water Resources Research*, 0(ja), 2019. doi: 10.1029/2019WR025164. URL https://agupubs.onlinelibrary.wiley.com/doi/abs/10.1029/2019WR025164.

A. Rogers, B. E. Medlyn, J. S. Dukes, G. Bonan, S. Caemmerer, M. C. Dietze, J. Kattge, A. D. B. Leakey, L. M. Mercado, Ü. Niinemets, I. C. Prentice, S. P. Serbin, S. Sitch, D. A. Way, and S. Zaehle. A roadmap for improving the representation of photosynthesis in Earth system models. *New Phytologist*, 213(1):22–42, 2017. doi: 10.1111/nph.14283. URL https://nph.onlinelibrary.wiley.com/doi/abs/10.1111/nph.14283.

L. Rowland, A. da Costa, D. R. Galbraith, R. S. Oliveira, O. J. Binks, A. A. R. Oliveira, A. M. Pullen, C. E. Doughty, D. B. Metcalfe, S. S. Vasconcelos, L. V. Ferreira, Y. Malhi, J. Grace, M. Mencuccini, and P. Meir. Death from drought in tropical forests is triggered by hydraulics not carbon starvation. *Nature*, 528(7580):119–122I, Dec 03 2015.

L. Sack, P. J. Melcher, M. A. Zwieniecki, and N. M. Holbrook. The hydraulic conductance of the angiosperm leaf lamina: a comparison of three measurement methods. *Journal of Experimental Botany*, 53(378):2177–2184, 2002. URL http://www.jstor.org/stable/23697621.

D. Schimel, F. D. Schneider, and JPL Carbon and Ecosystem Participants . Flux towers in the sky: global ecology from space. *New Phytologist*, 224(2):570–584, 2019. doi: 10.1111/nph.15934. URL https://nph.onlinelibrary.wiley.com/doi/abs/10.1111/nph.15934.

R. Seager, A. Hooks, A. P. Williams, B. Cook, J. Nakamura, and N. Henderson. Climatology, variability, and trends in the U.S. vapor pressure deficit, an important fire-related meteorological quantity. *Journal of Applied Meteorology and Climatology*, 54(6):1121–1141, 2015. doi: 10.1175/JAMC-D-14-0321.1.

P. J. Sellers, D. A. Randall, G. J. Collatz, J. A. Berry, C. B. Field, D. A. Dazlich, C. Zhang, G. D. Collelo, and L. Bounoua. a revised land surface parameterization (SiB2) for atmospheric GCMs. part I: Model formulation. *Journal of Climate*, 9(4):676–705, 1996a. doi: 10.1175/1520-0442(1996)009$⟨$0676:ARLSPF$⟩$2.0.CO;2.

P. J. Sellers, C. J. Tucker, G. J. Collatz, S. O. Los, C. O. Justice, D. A. Dazlich, and D. A. Randall. A revised land surface parameterization (SiB2) for atmospheric GCMs. part II: The generation of global fields of terrestrial biophysical parameters from satellite data. *Journal of Climate*, 9(4):706–737, 1996b. doi: {10.1175/1520-0442(1996)009$⟨$0706: ARLSPF$⟩$2.0.CO;2}.

S. I. Seneviratne, D. Lüthi, M. Litschi, and C. Schär. Land-atmosphere coupling and climate change in Europe. *Nature*, 443(7108):205–9, Sep 14 2006.

S. I. Seneviratne, T. Corti, E. L. Davin, M. Hirschi, E. B. Jaeger, I. Lehner, B. Orlowsky, and A. J. Teuling. Investigating soil moistureclimate interactions in a changing climate: A review. *Earth-Science Reviews*, 99(3):125 – 161, 2010. ISSN 0012-8252. doi: https://doi.org/10.1016/j.earscirev.2010.02.004. URL `http://www.sciencedirect.com/science/article/pii/S0012825210000139`.

K. A. Simonin, E. Burns, B. Choat, M. M. Barbour, T. E. Dawson, and P. J. Franks. Increasing leaf hydraulic conductance with transpiration rate minimizes the water potential drawdown from stem to leaf. *Journal of Experimental Botany*, 66(5):1303–1315, 2015. doi: 10.1093/jxb/eru481.

S. Sitch, P. Friedlingstein, N. Gruber, S. D. Jones, G. Murray-Tortarolo, A. Ahlström, S. C. Doney, H. Graven, C. Heinze, C. Huntingford, S. Levis, P. E. Levy, M. Lomas, B. Poulter, N. Viovy, S. Zaehle, N. Zeng, A. Arneth, G. Bonan, L. Bopp, J. G. Canadell, F. Chevallier, P. Ciais, R. Ellis, M. Gloor, P. Peylin, S. L. Piao, C. Le Quéré, B. Smith, Z. Zhu, and R. Myneni. Recent trends and drivers of regional sources and sinks of carbon dioxide. *Biogeosciences*, 12(3):653–679, 2015. doi: 10.5194/bg-12-653-2015. URL `https://www.biogeosciences.net/12/653/2015/`.

R. P. Skelton, A. G. West, and T. E. Dawson. Predicting plant vulnerability to drought in biodiverse regions using functional traits. *Proceedings of the National Academy of Sciences*, 112(18):5744–5749, 2015. doi: 10.1073/pnas.1503376112. URL `https://www.pnas.org/content/112/18/5744`.

J. S. Sperry and D. M. Love. What plant hydraulics can tell us about responses to climate-change droughts. *New Phytologist*, 207(1):14–27, 2015. ISSN 1469-8137. doi: 10.1111/nph.13354. URL `http://dx.doi.org/10.1111/nph.13354`.

J. S. Sperry, F. R. Adler, G. S. Campbell, and J. P. Comstock. Limitation of plant water use by rhizosphere and xylem conductance: results from a model. *Plant Cell Environment*, 21 (4):347–359, 1998. ISSN 1365-3040. doi: 10.1046/j.1365-3040.1998.00287.x. URL http://dx.doi.org/10.1046/j.1365-3040.1998.00287.x.

J. S. Sperry, M. D. Venturas, W. R. L. Anderegg, M. Mencuccini, D. S. Mackay, Y. Wang, and D. M. Love. Predicting stomatal responses to the environment from the optimization of photosynthetic gain and hydraulic cost. *Plant, Cell & Environment*, 40(6):816–830, 2017. ISSN 1365-3040. doi: 10.1111/pce.12852. URL http://dx.doi.org/10.1111/pce.12852. PCE-16-0541.R1.

B. D. Stocker, J. Zscheischler, T. F. Keenan, I. C. Prentice, J. Peñuelas, and S. I. Seneviratne. Quantifying soil moisture impacts on light use efficiency across biomes. *New Phytologist*, 218(4):1430–1449, 2018. doi: 10.1111/nph.15123. URL https://nph.onlinelibrary.wiley.com/doi/abs/10.1111/nph.15123.

S. C. Swenson and D. M. Lawrence. A GRACE-based assessment of interannual groundwater dynamics in the Community Land Model. *Water Resources Research*, 51(11):8817–8833, 2015. doi: 10.1002/2015WR017582.

J. Tang, W. J. Riley, and J. Niu. Incorporating root hydraulic redistribution in CLM4.5: Effects on predicted site and global evapotranspiration, soil moisture, and water storage. *Journal of Advances in Modeling Earth Systems*, 7(4):1828–1848, 2015. doi: 10.1002/2015MS000484. URL https://agupubs.onlinelibrary.wiley.com/doi/abs/10.1002/2015MS000484.

F. Tardieu and T. Simonneau. Variability among species of stomatal control under fluctuating soil water status and evaporative demand: modelling isohydric and anisohydric behaviours. *Journal of Experimental Botany*, 49:419–432, 1998. ISSN 00220957, 14602431. URL http://www.jstor.org/stable/23695975.

P. E. Thornton and N. E. Zimmermann. An improved canopy integration scheme for a land surface model with prognostic canopy structure. *Journal of Climate*, 20(15):3902–3923, 2007. doi: 10.1175/JCLI4222.1. URL https://doi.org/10.1175/JCLI4222.1.

A. T. Trugman, D. Medvigy, J. S. Mankin, and W. R. L. Anderegg. Soil moisture stress as a major driver of carbon cycle uncertainty. *Geophysical Research Letters*, 45, 2018. doi: 10.1029/2018GL078131. URL https://agupubs.onlinelibrary.wiley.com/doi/abs/10.1029/2018GL078131.

A. T. Trugman, L. D. L. Anderegg, J. S. Sperry, Y. Wang, M. Venturas, and W. R. L. Anderegg. Leveraging plant hydraulics to yield predictive and dynamic plant leaf allocation in vegetation models with climate change. *Global Change Biology*, 0(ja), 2019. doi: 10.1111/gcb.14814. URL https://onlinelibrary.wiley.com/doi/abs/10.1111/gcb.14814.

M. T. Tyree and F. W. Ewers. The hydraulic architecture of trees and other woody plants. *New Phytologist*, 119(3):345–360, 1991. doi: 10.1111/j.1469-8137.1991.tb00035.x.

URL https://nph.onlinelibrary.wiley.com/doi/abs/10.1111/j.1469-8137.1991.tb00035.x.

M. T. Tyree and J. S. Sperry. Vulnerability of xylem to cavitation and embolism. *Annual Review of Plant Physiology and Plant Molecular Biology*, 40(1):19–36, 1989. doi: 10.1146/annurev.pp.40.060189.000315.

A. M. Ukkola, M. G. D. Kauwe, A. J. Pitman, M. J. Best, G. Abramowitz, V. Haverd, M. Decker, and N. Haughton. Land surface models systematically overestimate the intensity, duration and magnitude of seasonal-scale evaporative droughts. *Environmental Research Letters*, 11(10):104012, 2016. URL http://stacks.iop.org/1748-9326/11/i=10/a=104012.

M. D. Venturas, E. D. MacKinnon, H. L. Dario, A. L. Jacobsen, R. B. Pratt, and S. D. Davis. Chaparral shrub hydraulic traits, size, and life history types relate to species mortality during california's historic drought of 2014. *PLoS ONE*, 11(7), 2016.

A. Verhoef and G. Egea. Modeling plant transpiration under limited soil water: Comparison of different plant and soil hydraulic parameterizations and preliminary implications for their use in land surface models. *Agricultural and Forest Meteorology*, 191:22–32, 2014. ISSN 0168-1923. doi: https://doi.org/10.1016/j.agrformet.2014.02.009. URL http://www.sciencedirect.com/science/article/pii/S0168192314000483.

J. M. Warren, P. J. Hanson, C. M. Iversen, J. Kumar, A. P. Walker, and S. D. Wullschleger. Root structural and functional dynamics in terrestrial biosphere models - evaluation and recommendations. *New Phytologist*, 205(1):59–78, 2015. doi: 10.1111/nph.13034. URL https://nph.onlinelibrary.wiley.com/doi/abs/10.1111/nph.13034.

W. R. Wieder, D. M. Lawrence, R. A. Fisher, G. B. Bonan, S. J. Cheng, C. L. Goodale, A. S. Grandy, C. D. Koven, D. L. Lombardozzi, K. W. Oleson, and R. Q. Thomas. Beyond static benchmarking: Using experimental manipulations to evaluate land model assumptions. *Global Biogeochemical Cycles*, 0(ja), 2019. doi: 10.1029/2018GB006141. URL https://agupubs.onlinelibrary.wiley.com/doi/abs/10.1029/2018GB006141.

A. P. Williams, C. D. Allen, A. K. Macalady, D. Griffin, C. A. Woodhouse, D. M. Meko, T. W. Swetnam, S. A. Rauscher, R. Seager, H. Grissino-Mayer, J. S. Dean, E. R. Cook, C. Gangodagamage, M. Cai, and N. G. Mcdowell. Temperature as a potent driver of regional forest drought stress and tree mortality. *Nature Climate Change*, 3(3):292–297, 03 2013. URL http://ezproxy.cul.columbia.edu/login?url=https://search.proquest.com/docview/1312498340?accountid=10226.

M. Williams, E. B. Rastetter, D. N. Fernandes, M. L. Goulden, S. C. Wofsy, G. R. Shaver, J. M. Melillo, J. W. Munger, S.-M. Fan, and K. J. Nadelhoffer. Modelling the soil-plant-atmosphere continuum in a Quercus-Acer stand at Harvard Forest: the regulation of stomatal conductance by light, nitrogen and soil/plant hydraulic properties. *Plant, Cell & Environment*, 19(8):911–927, 1996. ISSN 1365-3040. doi: 10.1111/j.1365-3040.1996.tb00456.x. URL http://dx.doi.org/10.1111/j.1365-3040.1996.tb00456.x.

M. Williams, B. E. Law, P. M. Anthoni, and M. H. Unsworth. Use of a simulation model and ecosystem flux data to examine carbon-water interactions in ponderosa pine. *Tree Physiology*, 21(5):287 – 298, 2001. ISSN 0829318X.

A. Wolf, W. R. L. Anderegg, and S. W. Pacala. Optimal stomatal behavior with competition for water and risk of hydraulic impairment. *Proceedings of the National Academy of Sciences*, 113(46):E7222–E7230, 2016. doi: 10.1073/pnas.1615144113. URL https://www.pnas.org/content/113/46/E7222.

I. J. Wright, M. Westoby, and P. B. Reich. Convergence towards higher leaf mass per area in dry and nutrient-poor habitats has different consequences for leaf life span. *Journal of Ecology*, 90(3):534–543, 2002. doi: 10.1046/j.1365-2745.2002.00689.x.

X. Xu, D. Medvigy, J. S. Powers, J. M. Becknell, and K. Guan. Diversity in plant hydraulic traits explains seasonal and inter-annual variations of vegetation dynamics in seasonally dry tropical forests. *New Phytologist*, 212(1):80–95, 2016. ISSN 1469-8137. doi: 10.1111/nph.14009. URL http://dx.doi.org/10.1111/nph.14009. 2015-20772.

K. Yi, J. T. Maxwell, M. K. Wenzel, D. T. Roman, P. E. Sauer, R. P. Phillips, and K. A. Novick. Linking variation in intrinsic water-use efficiency to isohydricity: a comparison at multiple spatiotemporal scales. *New Phytologist*, 221(1):195–208, 2019. doi: 10.1111/nph.15384.

S. Zhou, R. A. Duursma, B. E. Medlyn, J. W. Kelly, and I. C. Prentice. How should we model plant responses to drought? An analysis of stomatal and non-stomatal responses to water stress. *Agricultural and Forest Meteorology*, 182-183:204 – 214, 2013. ISSN 0168-1923. doi: https://doi.org/10.1016/j.agrformet.2013.05.009. URL http://www.sciencedirect.com/science/article/pii/S0168192313001263.

S. Zhou, A. P. Williams, A. M. Berg, B. I. Cook, Y. Zhang, S. Hagemann, R. Lorenz, S. I. Seneviratne, and P. Gentine. Land-atmosphere feedbacks exacerbate concurrent soil drought and atmospheric aridity. *Proceedings of the National Academy of Sciences*, 2019a. doi: 10.1073/pnas.1904955116. URL https://www.pnas.org/content/early/2019/08/27/1904955116.

S. Zhou, Y. Zhang, A. Park Williams, and P. Gentine. Projected increases in intensity, frequency, and terrestrial carbon costs of compound drought and aridity events. *Science Advances*, 5(1), 2019b. doi: 10.1126/sciadv.aau5740. URL http://advances.sciencemag.org/content/5/1/eaau5740.

Appendix A

Chapter 1 supplemental materials

A.1 Appendix to model description

A.1.1 Details of water supply

PHS resolves flow across four different segments, soil-to-root, root-to-stem, stem-to-leaf, and leaf-to-transpiration.

Stem-to-leaf. The area bases are sunlit and shaded leaf area, respectively. Note that gravity is assumed negligible here. Likewise there is no length scaling applied to maximum conductance. Therefore the input parameter for $k_{leaf,\max}$ should be a conductance (s^{-1}).

$$\begin{aligned} q_{sun} &= k_{sun} \cdot \text{LAI-sun} \cdot (\psi_{\text{stem}} - \psi_{\text{sun-leaf}}) \\ q_{shade} &= k_{shade} \cdot \text{LAI-shade} \cdot (\psi_{\text{stem}} - \psi_{\text{shade-leaf}}) \end{aligned} \tag{A.1}$$

$$k_{sun} = k_{shade} = k_{leaf,\max} \cdot f(\psi_{\text{stem}}) \tag{A.2}$$

$$f(\psi) = 2^{-\left(\frac{\psi}{p_{50}}\right)^{c_k}} \tag{A.3}$$

Root-to-stem. The area basis is stem area index. The input parameter is maximum stem xylem conductivity ($K_{stem,\max}$). Stem conductance (k_{stem}) is the result of scaling maximum conductivity by the tree height (h) and applying loss relative to maximum conductance via the vulnerability curve $f(\psi_{\text{root}})$.

$$q_{stem} = k_{stem} \cdot \text{SAI} \cdot (\psi_{\text{root}} - \psi_{\text{stem}} - \rho g h) \tag{A.4}$$

$$k_{stem} = \frac{K_{stem,\max}}{h} \cdot f(\psi_{\text{root}}) \tag{A.5}$$

Soil-to-root. Area basis is RAI in soil layer i, which is based on the layer root fraction times the total root area. Total root area is calculated as the sum of stem and leaf area indices multiplied by a relative root area parameter (f_{root}). The vertical root distribution is defined by the layer root fraction (r_i), which follows a one-parameter (by PFT) power law decay following Jackson et al. [1996].

$$q_{sr,i} = k_{sr,i} \cdot \text{RAI}_i \cdot (\psi_{\text{soil,i}} - \psi_{\text{root}} - \rho g z_i) \tag{A.6}$$

$$\text{RAI}_i = f_{\text{root}} \cdot (\text{SAI} + \text{LAI}) \cdot r_i \tag{A.7}$$

$$k_{sr,i} = \frac{k_{r,i} + k_{s,i}}{k_{r,i} \cdot k_{s,i}} \tag{A.8}$$

$$k_{r,i} = \frac{K_{r,\max}}{l_i} f\left(\psi_{\text{soil,i}}\right) \tag{A.9}$$

$$l_i = z_i + x \tag{A.10}$$

$$k_{s,i} = \frac{K_{s,i}}{d} \tag{A.11}$$

The soil-and-root conductance $k_{sr,i}$ reflects two resistors in series, from soil-to-root ($k_{s,i}$) and through the root tissue ($k_{r,i}$). The root tissue conductance is attenuated via the vulnerability curve framework. The input parameter is maximum root xylem conductivity, on the basis of RAI as defined above. The root conductivity is scaled by the conducting length, which is estimated as the sum of soil layer depth (z_i) and average lateral extent (x, static parameter). The soil conductivity $K_{s,i}$ is calculated from the layer soil matric potential ($\psi_{soil,i}$) and soil properties as described in Oleson et al. [2013] utilizing typical soil hydraulic theory [Brooks and Corey, 1964, Clapp and Hornberger, 1978]. The soil conductance ($k_{s,i}$) is the result of scaling the conductivity by d, the distance between roots estimated following Williams et al. [1996] and Bonan et al. [2014]

A.1.2 Details of water demand

The CLM5 implementation utilizes the Medlyn stomatal conductance model [Medlyn et al., 2011], while also applying water stress through V_{cmax}. Transpiration is calculated reflecting contributions from both stomatal conductance and leaf boundary layer conductance (g_b).

$$V_{\text{cmax}} = f_w \, V_{\text{cmax,ww}} \tag{A.12}$$

$$g_s = g_0 + \left(1 + \frac{g_1}{\sqrt{D}}\right) \frac{A}{C_a} \tag{A.13}$$

$$\begin{aligned} E_{sun} &= g_{s,sun} * \rho * \text{VPD} * lai_{sun} * \left(1 + \frac{g_{s,sun}}{g_b}\right)^{-1} \\ E_{shade} &= g_{s,shade} * \rho * \text{VPD} * lai_{shade} * \left(1 + \frac{g_{s,shade}}{g_b}\right)^{-1} \end{aligned} \tag{A.14}$$

At the beginning of a set of PHS iterations, we solve for $E_{\text{sun,max}}$ and $E_{\text{shade,max}}$, by running the stomatal conductance scheme with f_w set to 1 (no stress). Within each PHS iteration, we do not resolve the full stomatal conductance scheme, but instead consider only the linear attenuation of stomatal conductance by f_w. Transpiration is attenuated relative to the maximal values according to leaf water potential.

$$
\begin{aligned}
E_{\text{sun}} &= E_{\text{sun,max}} * 2^{-\left(\frac{\psi_{\text{leaf}}}{\psi_{50}}\right)^{c_k}} \\
E_{\text{shade}} &= E_{\text{shade,max}} * 2^{-\left(\frac{\psi_{\text{leaf}}}{\psi_{50}}\right)^{c_k}}
\end{aligned}
\tag{A.15}
$$

We define f_w as the ratio of attenuated stomatal conductance ($g_{s,sun}$, $g_{s,shade}$) to maximal stomatal conductance ($g_{s,sun,max}$, $g_{s,shade,max}$), where $g_{s,sun,max}$ and $g_{s,shade,max}$ are the stomatal conductance values associated with $E_{\text{sun,max}}$ and $E_{\text{shade,max}}$. As such, the definition in the main text (Equation 1.14), represents a linear simplification between f_w, stomatal conductance, and transpiration.

$$
\begin{aligned}
f_{w,sun} &= \frac{g_{s,sun}}{g_{s,sun,max}} \\
f_{w,shade} &= \frac{g_{s,shade}}{g_{s,shade,max}}
\end{aligned}
\tag{A.16}
$$

After each PHS iteration, we compute $g_{s,sun}$ and $g_{s,shade}$ via Equations A.12 and A.12 (which involves iterating for intercellular CO_2 concentration). We then update $g_{s,sun,max}$ and $g_{s,shade,max}$ to achieve consistency between equations (A.14) and (A.15). At this point $g_{s,sun,max}$ and $g_{s,shade,max}$ no longer refer to the values associated with $f_w = 1$, but rather also incorporate the non-linearity between g_s and f_w. The PHS iteration continues to convergence of f_w (see Figure A.1). The numerics have proven to be stable in practice, but future versions may aim to better integrate PHS within the stomatal conductance scheme to improve the coherence of Equations 1.14 and A.16.

$$
\begin{aligned}
g_{s,sun,max} &= \frac{g_{s,sun}}{f_{w,sun}} \\
g_{s,shade,max} &= \frac{g_{s,shade}}{f_{w,shade}}
\end{aligned}
\tag{A.17}
$$

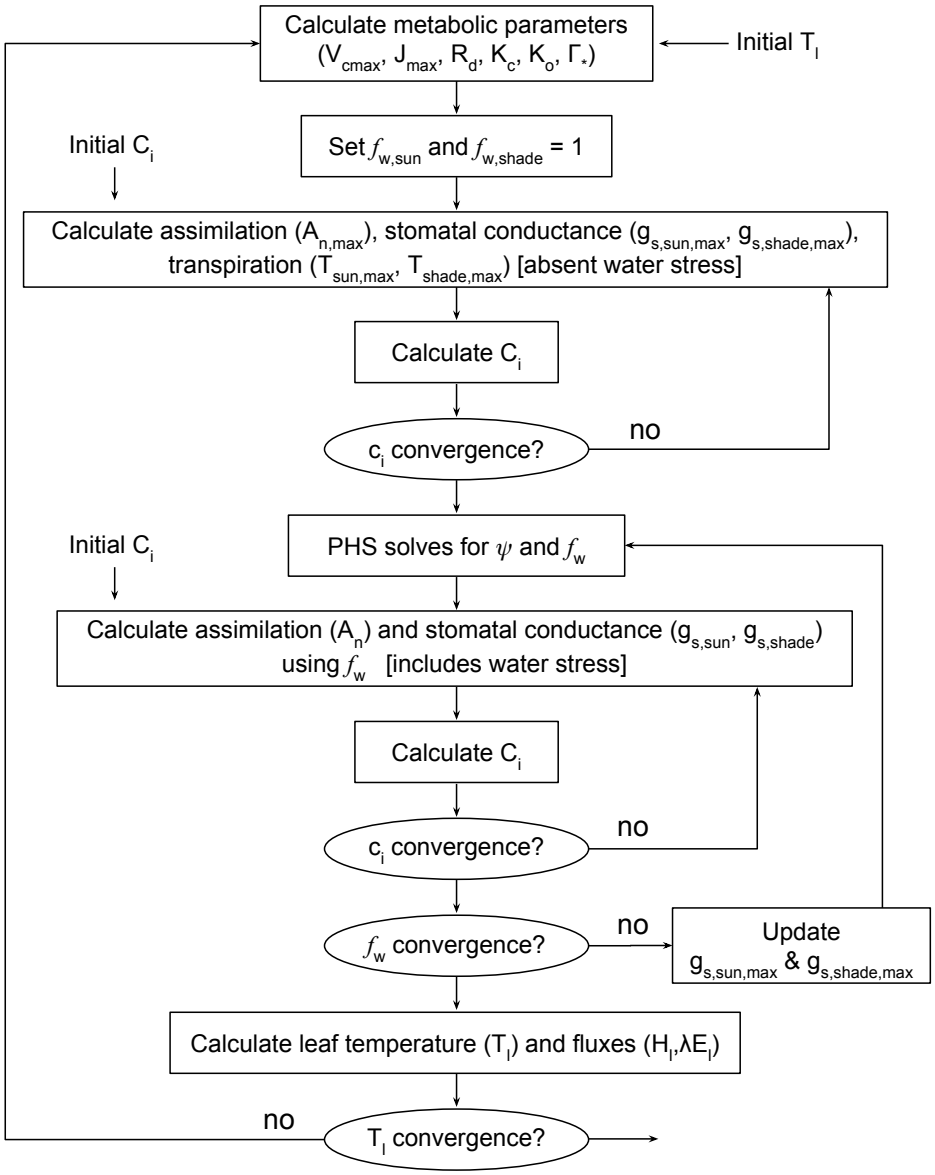

Figure A.1: Flow chart of PHS iterative solution

A.1.3 Details of water potential solution

The continuity of water flow through the system yields four equations

$$\begin{aligned} E_{sun} &= q_{sun} \\ E_{shade} &= q_{shade} \\ q_{sun} + q_{shade} &= q_{stem} \\ q_{stem} &= \sum_{i=1}^{nlevsoi} q_{sr,i} \end{aligned} \tag{A.18}$$

We seek the set of vegetation water potential values (four unknowns),

$$\psi = \begin{bmatrix} \psi_{sunleaf} \\ \psi_{shadeleaf} \\ \psi_{stem} \\ \psi_{root} \end{bmatrix} \tag{A.19}$$

that satisfies these equations, as forced by the soil moisture and atmospheric state. Each flux on the schematic can be represented in terms of the relevant water potentials. Defining the transpiration fluxes:

$$\begin{aligned} E_{sun} &= E_{sun,max} \cdot 2^{-\left(\frac{\psi_{sunleaf}}{p50}\right)^{c_k}} \\ E_{shade} &= E_{shade,max} \cdot 2^{-\left(\frac{\psi_{shadeleaf}}{p50}\right)^{c_k}} \end{aligned} \tag{A.20}$$

Defining the water supply fluxes:

$$\begin{aligned} q_{sun} &= k_{leaf,max} \cdot 2^{-\left(\frac{\psi_{stem}}{p50}\right)^{c_k}} \cdot \mathrm{LAI}_{sun} \cdot (\psi_{stem} - \psi_{sunleaf}) \\ q_{shade} &= k_{leaf,max} \cdot 2^{-\left(\frac{\psi_{stem}}{p50}\right)^{c_k}} \cdot \mathrm{LAI}_{shade} \cdot (\psi_{stem} - \psi_{shadeleaf}) \\ q_{stem} &= \frac{k_{stem,max}}{z_2} \cdot 2^{-\left(\frac{\psi_{root}}{p50}\right)^{c_k}} \cdot SAI \cdot (\psi_{root} - \psi_{stem} - \Delta\psi_z) \\ q_{root} &= \sum_{i=1}^{nlevsoi} q_{sr,i} = \sum_{i=1}^{nlevsoi} k_{sr,i} \cdot RAI \cdot (\psi_{soil,i} - \psi_{root} + \Delta\psi_{z,i}) \end{aligned} \tag{A.21}$$

In the CLM parameter file, $p50$ and c_k are allowed to vary by flux level (transpiration vs. stem flux vs. root flux), but in our experiment (and on the default CLM parameter file), a single value is used for each. PHS solves for the vector ψ that satisfying water flow continuity as forced by atmospheric state and soil moisture. Due to the model non-linearity, we use a linearized explicit approach, iterating with Newton's method. The initial guess

is the solution for ψ (vector) from the previous time step. The general framework, from iteration m to $m+1$ is:

$$\begin{aligned} q^{m+1} &= q^m + \frac{\delta q}{\delta \psi}\Delta\psi \\ \psi^{m+1} &= \psi^m + \Delta\psi \end{aligned} \tag{A.22}$$

So for our first flux balance equation, which requires sunlit leaf transpiration equal the flux of water from the main stem to the sunlit leaf, we have (at iteration $m+1$):

$$E_{sun}^{m+1} = q_{sun}^{m+1} \tag{A.23}$$

This can be linearized to:

$$E_{sun}^{m} + \frac{\delta E_{sun}}{\delta \psi}\Delta\psi = q_{sun}^{m} + \frac{\delta q_{sun}}{\delta \psi}\Delta\psi \tag{A.24}$$

And rearranged to be:

$$\frac{\delta q_{sun}}{\delta \psi}\Delta\psi - \frac{\delta E_{sun}}{\delta \psi}\Delta\psi = E_{sun}^{m} - q_{sun}^{m} \tag{A.25}$$

And for the other 3 flux balance equations:

$$\begin{aligned} \frac{\delta q_{shade}}{\delta \psi}\Delta\psi - \frac{\delta E_{sha}}{\delta \psi}\Delta\psi &= E_{sha}^{m} - q_{1b}^{m} \\ \frac{\delta q_{stem}}{\delta \psi}\Delta\psi - \frac{\delta q_{sun}}{\delta \psi}\Delta\psi - \frac{\delta q_{shade}}{\delta \psi}\Delta\psi &= q_{sun}^{m} + q_{shade}^{m} - q_{stem}^{m} \\ \frac{\delta q_{soil}}{\delta \psi}\Delta\psi - \frac{\delta q_{stem}}{\delta \psi}\Delta\psi &= q_{stem}^{m} - q_{soil}^{m} \end{aligned} \tag{A.26}$$

Putting all four together in matrix form:

$$\begin{bmatrix} \frac{\delta q_{1a}}{\delta \psi} - \frac{\delta E_{sun}}{\delta \psi} \\ \frac{\delta q_{1b}}{\delta \psi} - \frac{\delta E_{sha}}{\delta \psi} \\ \frac{\delta q_{2}}{\delta \psi} - \frac{\delta q_{1a}}{\delta \psi} - \frac{\delta q_{1b}}{\delta \psi} \\ \frac{\delta q_{soil}}{\delta \psi} - \frac{\delta q_{2}}{\delta \psi} \end{bmatrix} \Delta\psi = \begin{bmatrix} E_{sun}^{m} - q_{1a}^{m} \\ E_{sha}^{m} - q_{1b}^{m} \\ q_{1a}^{m} + q_{1b}^{m} - q_{2}^{m} \\ q_{2}^{m} - q_{soil}^{m} \end{bmatrix} \tag{A.27}$$

Now to expand the left-hand side, from vector ψ to the four distinct plant water potential nodes, noting that many derivatives are zero (e.g. $\frac{\delta E_{sun}}{\delta \psi_{sha}} = 0$)

Introducing the notation: $A\Delta\psi = b$

$$\Delta\psi = \begin{bmatrix} \Delta\psi_{sunleaf} \\ \Delta\psi_{shadeleaf} \\ \Delta\psi_{stem} \\ \Delta\psi_{root} \end{bmatrix} \tag{A.28}$$

$$A = \begin{bmatrix} \frac{\delta q_{1a}}{\delta\psi_{sun}} - \frac{\delta E_{sun}}{\delta\psi_{sun}} & 0 & \frac{\delta q_{1a}}{\delta\psi_{stem}} & 0 \\ 0 & \frac{\delta q_{1b}}{\delta\psi_{sha}} - \frac{\delta E_{sha}}{\delta\psi_{sha}} & \frac{\delta q_{1b}}{\delta\psi_{stem}} & 0 \\ -\frac{\delta q_{1a}}{\delta\psi_{sun}} & -\frac{\delta q_{1b}}{\delta\psi_{sha}} & \frac{\delta q_2}{\delta\psi_{stem}} - \frac{\delta q_{1a}}{\delta\psi_{stem}} - \frac{\delta q_{1b}}{\delta\psi_{stem}} - \frac{\delta q_2}{\delta\psi_{stem}} & \frac{\delta q_2}{\delta\psi_{root}} \\ 0 & 0 & \frac{\delta q_{soil}}{\delta\psi_{root}} - \frac{\delta q_2}{\delta\psi_{root}} & \end{bmatrix} \tag{A.29}$$

$$b = \begin{bmatrix} E^m_{sun} - q^m_{b1} \\ E^m_{sha} - q^m_{b2} \\ q^m_{b1} + q^m_{b2} - q^m_{stem} \\ q^m_{stem} - q^m_{soil} \end{bmatrix} \tag{A.30}$$

We can compute all the entries for A and b based on the soil potential and maximum transpiration forcings and can solve to find:

$$\Delta\psi = A^{-1}b \tag{A.31}$$

$$\psi_{m+1} = \psi_m + \Delta\psi \tag{A.32}$$

We iterate until $b \to 0$, signifying water flux balance through the system. The result is a final set of water potentials (ψ_{root}, ψ_{stem}, $\psi_{shadeleaf}$, $\psi_{sunleaf}$) satisfying non-divergent water flux through the system.

A.1.4 Parameter tuning exercise

We used a factorial design to create 972 ensemble members based on the parameter values below. We ran PHS simulations for each parameter vector under both AMB and TFE conditions. All simulations used the same initial conditions, which were the result of a previous simulation. We evaluated the ensemble members based on the fit to sap flux observations, selecting that which maximized $R^2_{amb} + R^2_{tfe} - RMSE_{amb} - RMSE_{tfe}$ (Figure S2).

Stem conductivity, $k_{\max}$: 2e-8, 4e-8, 8e-8 s^{-1}
Root conductivity, $k_{r,\max}$: 2e-9, 6e-8, 18e-9 s^{-1}
Root and stem vulnerability p_{50}: -1.75, -2.25, -2.75 MPa
Stomatal p_{50}: above plus either 0 or 0.5MPa
Vulnerability shape parameter, c_k: 2.95, 3.95, 5.45 (unitless)

Medlyn slope, g_1: 6, 7 kPa$^{0.5}$
Rooting depth parameter, β: 0.95, 0.98, 0.993 (unitless)

A.2 Supplementary figures

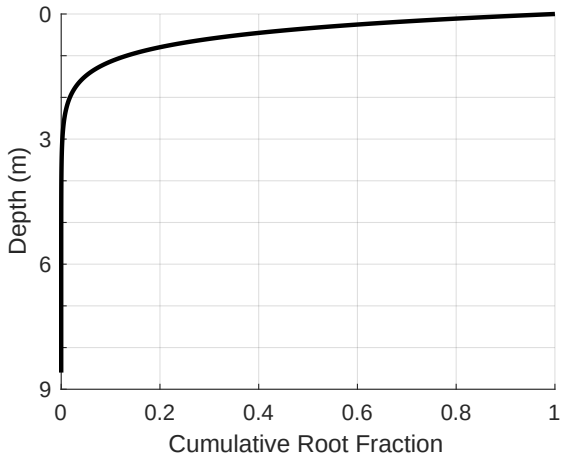

Figure A.2: Cumulative rooting distribution.

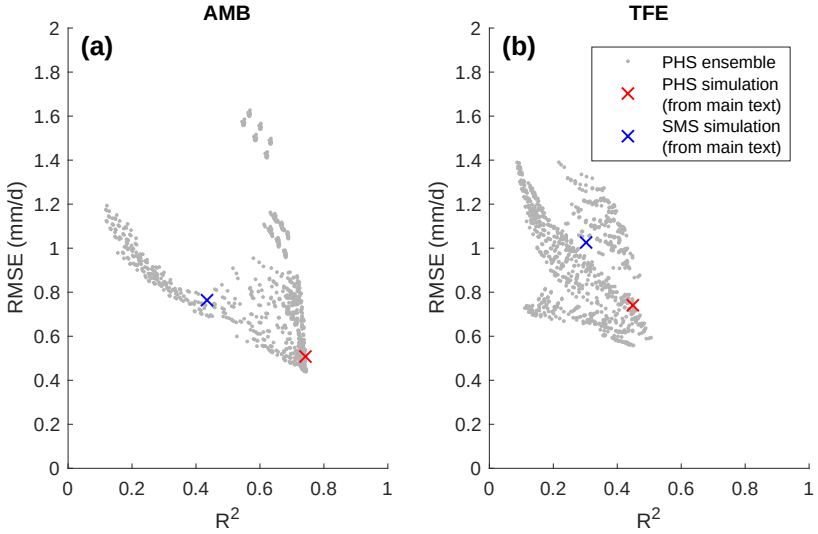

Figure A.3: Results of the PHS parameter tuning exercise. The main text PHS simulation was chosen to maximize R^2 - RMSE.

./Appendix1/figs/

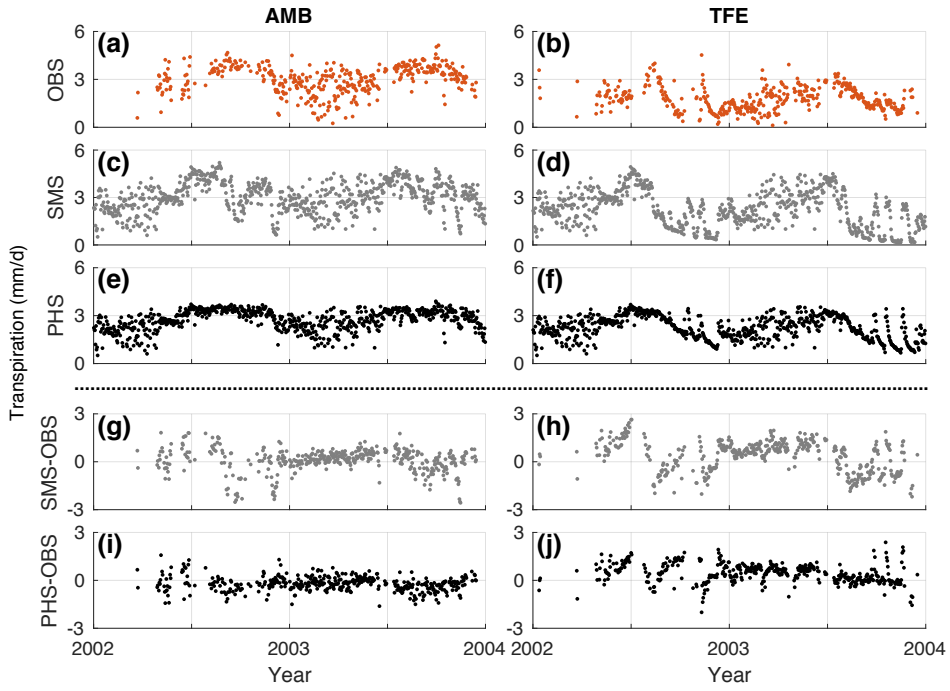

Figure A.4: (a-f) Time-series of daily total transpiration (mm/d), from (a,b) observations, (c,d) SMS model configuration, and (e,f) PHS model configuration under ambient and TFE conditions. (g-j) Difference between modeled and observed transpiration (mm/d), for (g,h) SMS and (i,j) PHS under ambient and TFE conditions.

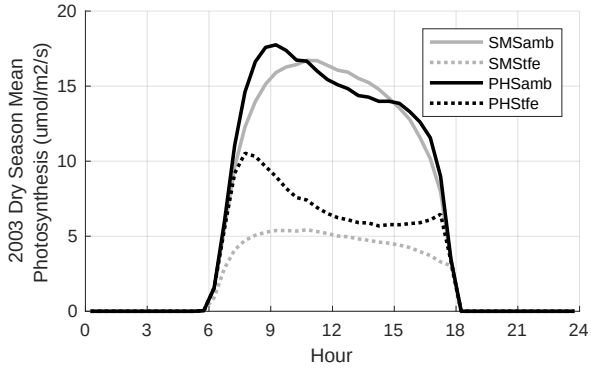

Figure A.5: 2003 dry season diurnal mean photosynthesis under ambient and TFE conditions for the two model configurations.

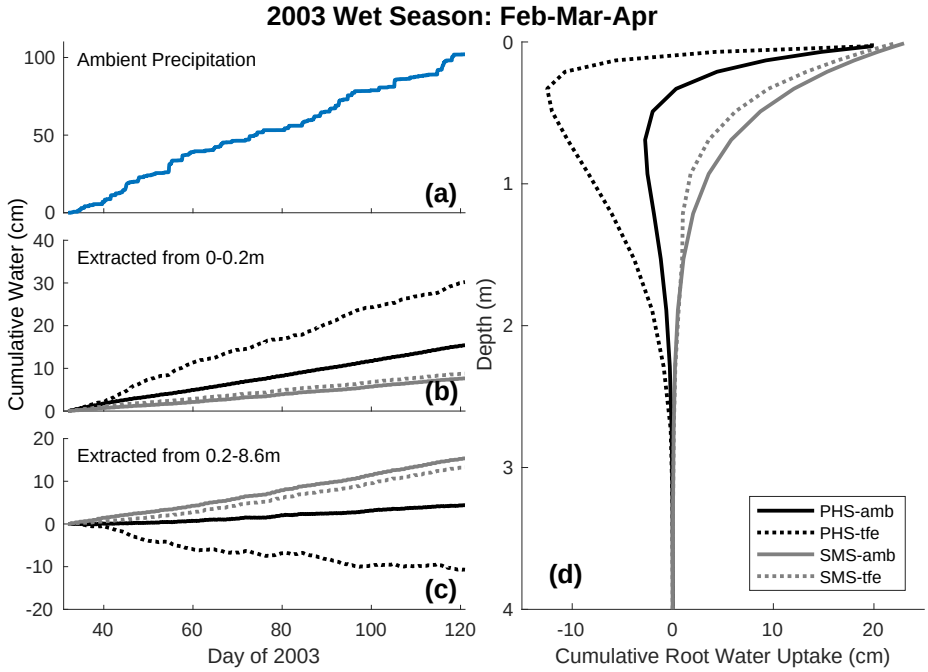

Figure A.6: 2003 wet season (FMA) cumulative root water uptake and precipitation. (a) Cumulative precipitation over time under ambient conditions (b,c) Cumulative water uptake over time from above and below 0.2m, respectively. (d) Cumulative root water uptake with depth.

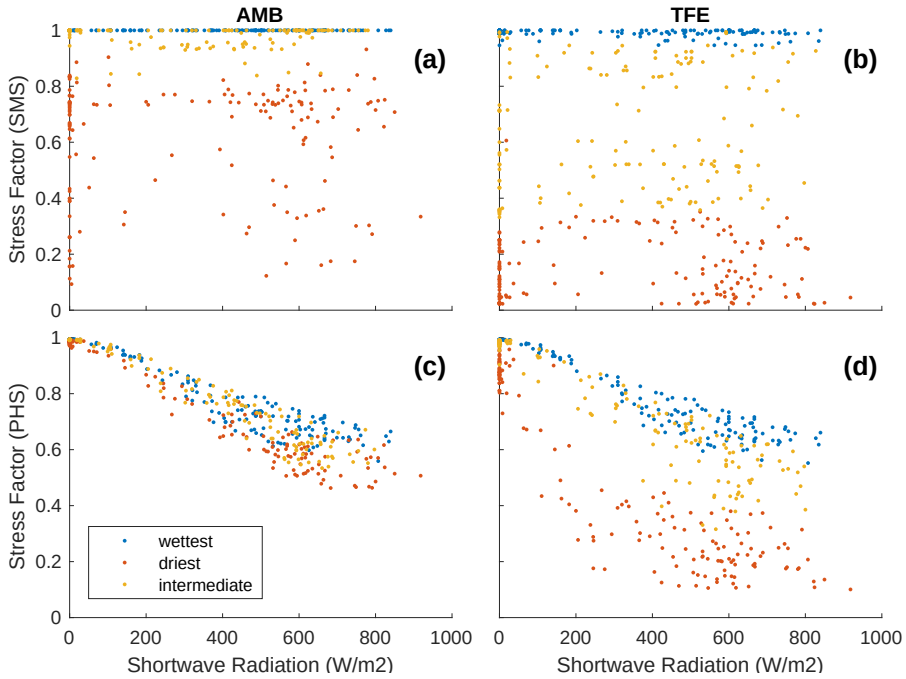

Figure A.7: Water stress factor versus downwelling shortwave radiation (2002-2003), for timesteps with VPD between 1 and 1.0559 kPa (n=470). VPD is controlled to highlight the relationship with downwelling radiation, the reverse (controlling for radiation) is shown in Figure 7. For SMS (a,b), data are subdivided based on average soil matric potential, weighted by root fraction. For PHS (c,d), data are subdivided based on predawn (5h) root water potential. Blue dots represent the wettest tercile, yellow dots represent the intermediate tercile, and red dots represent the driest tercile.

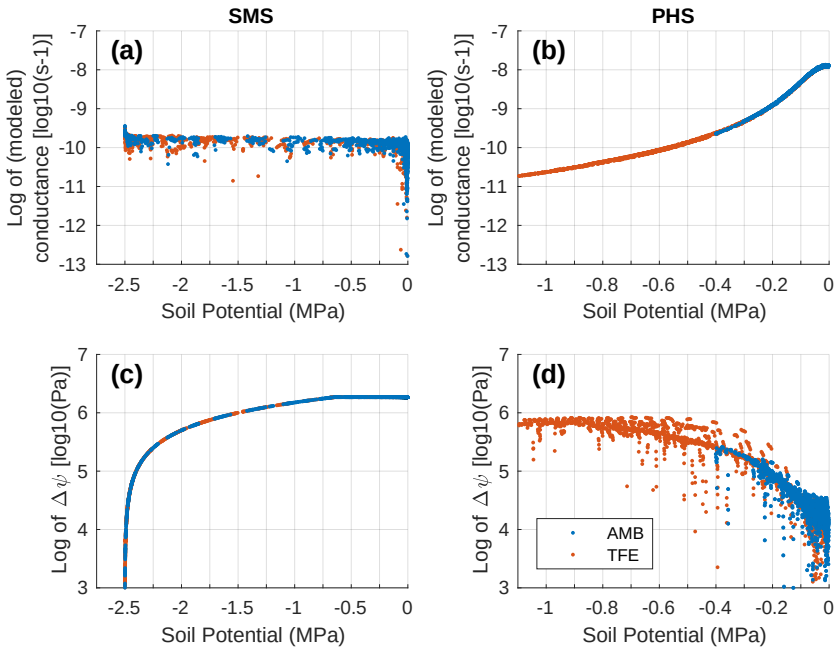

Figure A.8: (a,b) Log of conductance ($k_{s,r}$) versus soil potential for Soil Layer 5. (c,d) Log of hydraulic gradient ($\Delta\psi$) versus soil potential for Soil Layer 5. Note that the soil potential axes vary for PHS vs. SMS. Multiplied together $k_{s,r}$ and $\Delta\psi$ yield the Layer-5 root water uptake. PHS conductance decreases by almost 3 orders of magnitude between 0 and -1MPa, which leads to reduced RWU, though this is offset (by about half) due to increases in $\Delta\psi$. SMS $\Delta\psi$ decreases by less than 1 order of magnitude between 0 and -2MPa, leading to higher sensitivity to soil potential with PHS, see Figure 10. Approaching -2.5MPa, SMS $\Delta\psi$ decreases abruptly, due to the discontinuity at ψ_c. Only midday (12h-14h, 2002-2003) timesteps are shown to emphasize the relationship with soil potential. With SMS, conductance is not modeled explicitly, but rather calculated as $k{=}q/\Delta\psi$ (see Section 2.4.2). For soil potentials greater than or equal to 2.5MPa, $\Delta\psi{=}0$, and SMS implied conductance is undefined, but could probably be considered to equal 0. PHS conductance captures both root tissue and soil matrix resistances (operating in series).

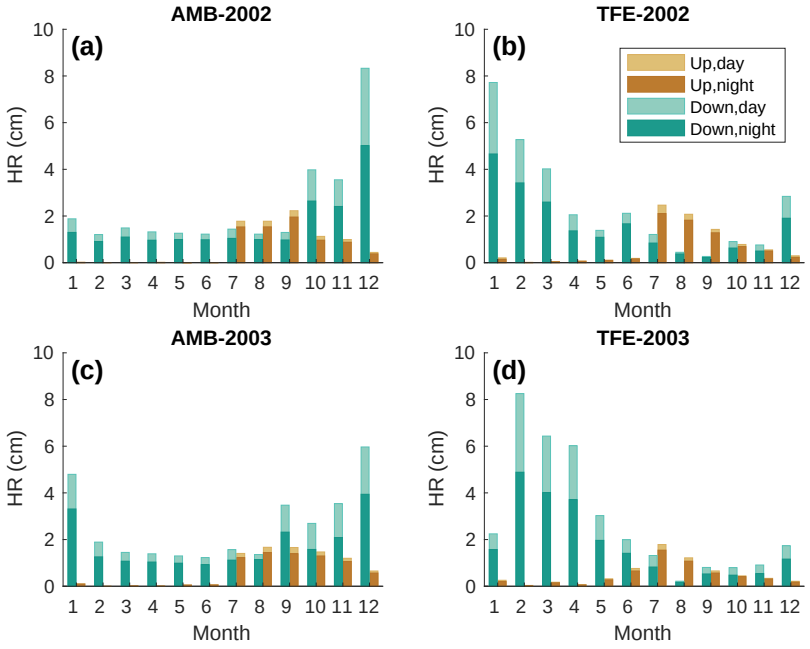

Figure A.9: PHS hydraulic distribution during 2002 and 2003, partitioning by direction and time of day.

Appendix B

Chapter 2 supplemental materials

B.1 Analysis details

Semi-arid tropics study domain:

- Latitude $\in$ [30°N, 30°S]
- Mean annual precipitation $<$ 1200 mm/yr
- Mean annual temperature $>$ 14 °C
- Mean annual GPP $>$ 0.5 gC/m2/d

For Figure 2.1a, the latitudinal mean and interquartile range were smoothed using an 11-gridcell moving window, which spans 10.4°. Both were weighted by land area. For the IQR, we therefore used the ΔIAV thresholds that exceeded the values for 25% and 75% of land area in the given moving window to compute IQR. For Figure 2.1a, we used 200mm/yr bins to produce a smooth average curve, again area-weighted.

For Figure 2.2 we used a standard area-weighted approach to calculate the average annual GPP anomalies for each model. For Figure 2.3, we used a composite approach to average across gridcells. Instead of averaging together the 1964 GPP annual means across the ≈1800 gridcells, we first sorted each gridcell's timeseries according to dryness. We then average GPP and SWC10cm values for 'year 1' across all gridcells, which corresponds to the driest year in each gridcell. This may be 1964 for some gridcells and 2005 for others. Annual average TWS was used as the dryness metric to sort the timeseries. The same compositing approach is used for Figure 2.4b and Supp Figure B.4.

For Figure 2.4a, we computed composite mean seasonal cycles for soil water potential at two depths for both models. Because the various gridcells feature differing dry seasons, it was necessary to re-index the timeseries to line up the dry seasons. We defined dry season as the contiguous 3month period with the least rain on average over the 50 year analysis period. JJA was the most common dry season (Supp Figure B.3), so we reindexed all gridcells to have JJA as their dry season before averaging. Likewise in Figure 2.4b, while we display the 'September' interannual relationship, this refers to September in the composite timeseries. This is in fact September for about 30% of gridcells, but it is also March for about 23% of gridcells. More precisely we are referring to the month immediately following the three-month dry season.

For Figure 2.5, we looked at how soil moisture and photosynthesis evolved after large precipitation anomalies, both dry and wet. Across the 50 year analysis period, we identified the 10 largest positive and 10 largest negative 1-month precipitation anomalies for each gridcell, disallowing repeats within +/- 3 months in order to better sample across years. Then we averaged together the soil moisture and GPP over the next 12 months for those

10 anomalies across all gridcells, weighted by land area. Because the two simulations use the same precipitation forcing, we are comparing all the same anomalies. E-folding times for the composite curves were calculated as the time-period for SWC10cm or GPP to fall to $1/e$ times the maximum anomaly, with linear extrapolation between months.

For Figure 2.6a, Pearson correlation coefficients were computed between annual average SWC10cm and TWS for each gridcell. We then summarized this data with a GPP-weighted probability distribution, calculating how much of total GPP across the domain falls in each of the correlation coefficient bins (bin width = 0.1). The full code for all the analyses in this study is available online at https://github.com/djk2120/PHSglobal.

B.2 Supplementary figures

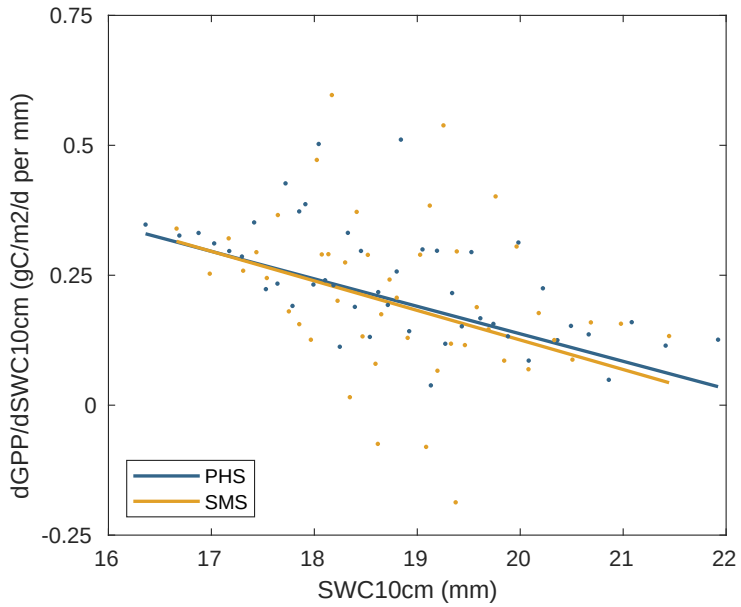

Figure B.1: Slope values relating GPP and SWC10cm. This plot complements Figure 2.3, demonstrating that the sensitivities of GPP to SWC10cm are comparable for PHS and SMS.

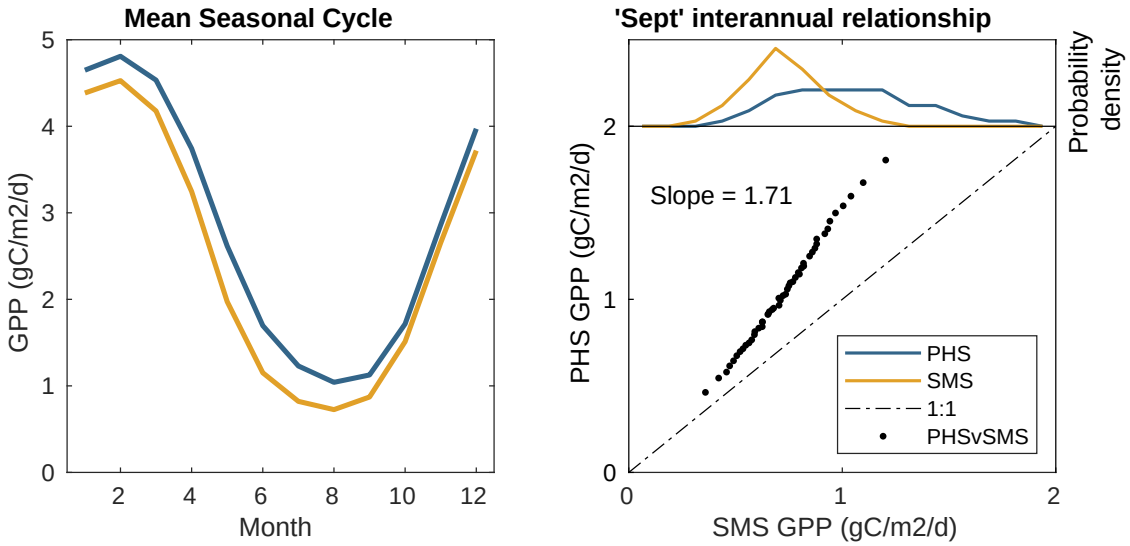

Figure B.2: Seasonal and interannual GPP. PHS has a much stronger response in dry season GPP to added water.

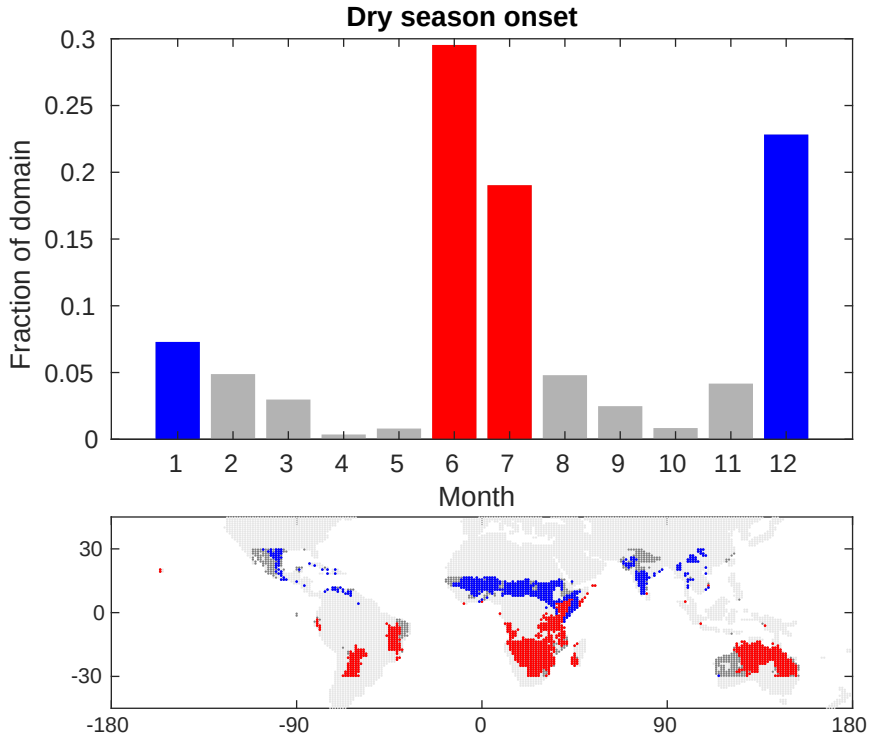

Figure B.3: Dry season onset. In order to compute the composite average soil potential seasonal cycles in Figure 2.4, we aligned the dry season across all grid-cells. Dry season was defined as the three month period with the lowest average precipitation across 1964-2013. The most common dry season was JJA, so this was chosen as the composite dry season. The next most common dry season was DJF. A map of the corresponding pixels demonstrates shows a sample of the geographic footprints. Light gray areas are not part of our semi-arid, tropical study domain.

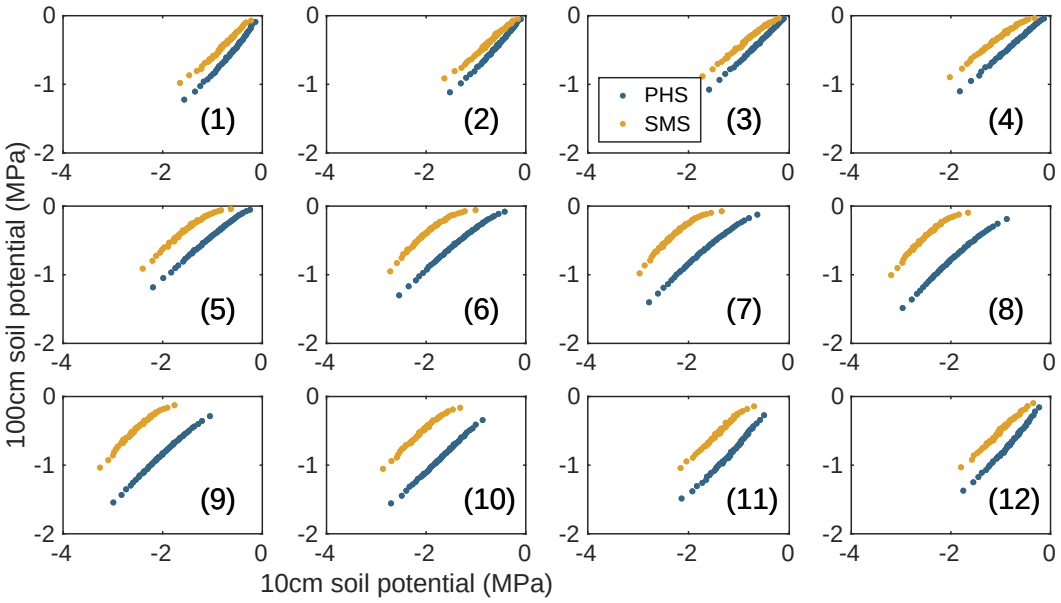

Figure B.4: The relationships between composite mean soil potential at depths of 100cm vs. 10cm across 50 years in the semi-arid tropcs. Subplots are numbered by month according to the dry season composite used for Figure 2.4. This means that 9 isn't necessarily September, but rather is 3 months after dry season onset.

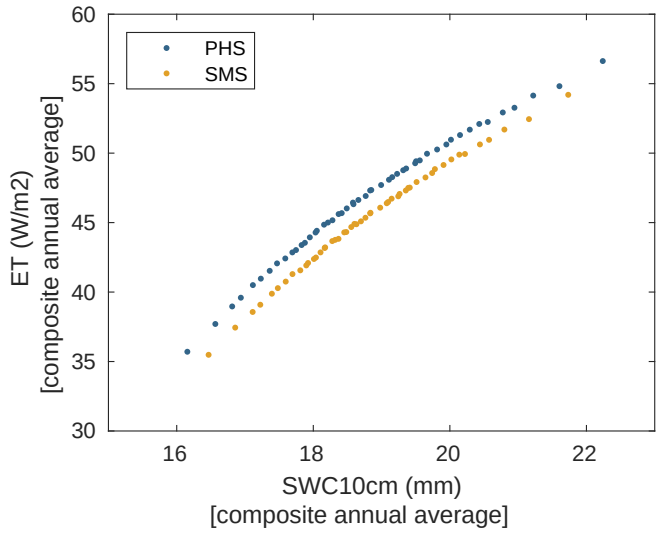

Figure B.5: ET vs. surface soil moisture. ET shows a comparable interannual sensitivity to SWC10cm in the two models.

Appendix C

Chapter 3 supplemental materials

C.1 Model description

For several of the simulations presented herein, we use a soil-plant-atmosphere continuum model with simplified plant hydraulics to test σ and I_R. As with the [Martínez-Vilalta et al., 2014] representation, we assume steady-state where transpiration T) matches sap flux (J). The same equation is used for T (Equation C.1), but several changes affect the parameterization of g_L (Equation 3.3).

$$T = g_L \cdot A_L \cdot D_L \tag{C.1}$$

$$g_L = g_{L,\max} \cdot f_g\left(\Psi_L\right) \tag{C.2}$$

First, instead of f_g depending on Ψ_s as in Equation 3.3, here the dependence is on Ψ_L (which, in turn, depends on Ψ_s). The use of Ψ_L reflects the influence of hydraulic constraints on stomatal function [Sperry and Love, 2015] and has been used in numerous other implementations [Kennedy et al., 2019, Xu et al., 2016, Wolf et al., 2016] Likewise, instead of the generic attenuation function f_g, we specify the relationship to Ψ_L subject to two parameters, $p_{g,1}$ and $p_{g,2}$, which represent the leaf water potential values at maximal and zero conductance, respectively. Conductance for Ψ_L outside the range of $p_{g,1}$ and $p_{g,2}$ are either 0 or $g_{L,\max}$, as appropriate.

$$f_g = \frac{\Psi_L - p_{g,2}}{p_{g,1} - p_{g,2}} \tag{C.3}$$

Furthermore, instead of defining $g_{L,\max}$ as a constant parameter, we adopt a common stomatal conductance model (Equation C.4), which incorporates the effects of photosynthesis, ambient CO_2 concentration (C_a), and D_L on stomatal conductance [Medlyn et al., 2011]. In doing so, we expand our model to also represent net photosynthesis (A) and intercellular CO_2 concentration (C_i), as described in Medlyn et al. [2011]. For simplicity, we set the Medlyn intercept parameter (g_0) to 0, and omit the effects of leaf respiration.

Table C.1: List of variables and abbreviations

Abbreviation	Full Name	Units
Γ	CO_2 compensation point	ppm
Λ	Ψ_L at $\Psi_s = 0$	MPa
σ	isohydricity slope	[-]
Ψ_L	leaf water potential	MPa
Ψ_s	soil water potential	MPa
Ψ	water potential along the hydraulic continuum	MPa
$\Delta\Psi$	$\Psi_L - \Psi_s$, hydraulic gradient from soil to leaf	MPa
A	net photosynthesis	μmol/m^2/s
A_J	rate of electron transport	mol/m^2/s
A_L	leaf area	[-]
A_s	basal sapwood area	[-]
C_a	ambient CO_2 concentration	ppm
C_i	intercellular CO_2 concentration	ppm
D_L	leaf-level vapor pressure deficit	[-]
f_g	fraction of maximum stomatal conductance	[-]
f_k	fraction of maximum hydraulic conductance	[-]
g_L	stomatal conductance to water vapor	mm/s
g_{Lc}	stomatal conductance to CO_2	mol/m^2/s
I_R	relative isohydricity	MPa^{-1}
J	sap flux	mm/s
k_s	whole plant hydraulic conductance	mm/s/MPa
SPAC	soil-plant-atmosphere continuum	not applicable
T	transpiration	mm/s

$$g_{L,\max} = g_0 + \left(1 + \frac{g_1}{\sqrt{D_L}}\right)\frac{A}{C_a} \tag{C.4}$$

$$A = \frac{A_j}{4}\frac{C_i - \Gamma}{C_i + 2\Gamma} \tag{C.5}$$

$$C_i = C_a - \frac{A}{g_{Lc}} \tag{C.6}$$

$$g_{Lc} = \frac{1}{1.6} g_L \tag{C.7}$$

We also adopt a more realistic model of J, where hydraulic conductance (k_s) varies along the continuum from soil-to-leaf (Equation C.8), as water potential (Ψ) decreases from Ψ_s to Ψ_L. Likewise, we specify the function for f_k, which depends on Ψ at the given point in the soil-to-leaf continuum subject to the parameters $p_{k,1}$ and $p_{k,2}$, which represent the water potential values at maximal and zero conductance, respectively. Like g_L, k_s is set to 0 or $k_{s,\max}$ outside the domain of $p_{k,1}$ and $p_{k,2}$. This is a common simplified sap flux representation in the vein of Sperry et al. [1998].

$$J = \int_{\Psi_s}^{\Psi_L} k_s(\Psi)\, d\Psi \tag{C.8}$$

$$k_s = k_{s,\max} \cdot f_k(\Psi) \tag{C.9}$$

$$f_k = \frac{\Psi - p_{k,2}}{p_{k,1} - p_{k,2}} \tag{C.10}$$

We do not present this as the only or best SPAC model. Our goal here is simply to expand the model from Martínez-Vilalta et al. [2014] in a way to allow further testing σ and I_R, imposing some typical model elements. In particular we will look at how these two metrics will respond to:

- a change in mean D_L
- when D_L is correlated with Ψ_s
- nonlinear parameterizations of f_g and f_k

C.2 Experiment description

Table C.2: List of isohydricity experiments

	Exp 1	Exp 2	Exp 3	Exp 4
Description	Relative isohydricity	Alter mean D_L	Covarying D_L	Dynamic k_s
Model	MV2014	⟵	Simple plant hydraulics	⟶
Variant	'Species 2'	D_L=3kPa	D_L=0.5→3.5kPa	$k_s = k_{s,\max} \cdot f(\Psi_s)$
Control	'Species 1'	D_L=1kPa	D_L=0.5kPa	n/a
D_L Forcing	constant	see above	see above	1 kPa
	(not explicitly defined)			
Ψ_s Forcing	⟵	0 to -3 MPa	⟶	
k_s	constant	constant	constant	varies
$k_{s,\max}$	(not explicitly defined)	2e-4	2e-4	4.5e-4 mm/s/MPa
$p_{g,1}$	(not explicitly defined)	-0.9	-0.6	-1.15 MPa
$p_{g,2}$	(not explicitly defined)	-3	-3	-2.25 MPa

C.3 Supplementary figures

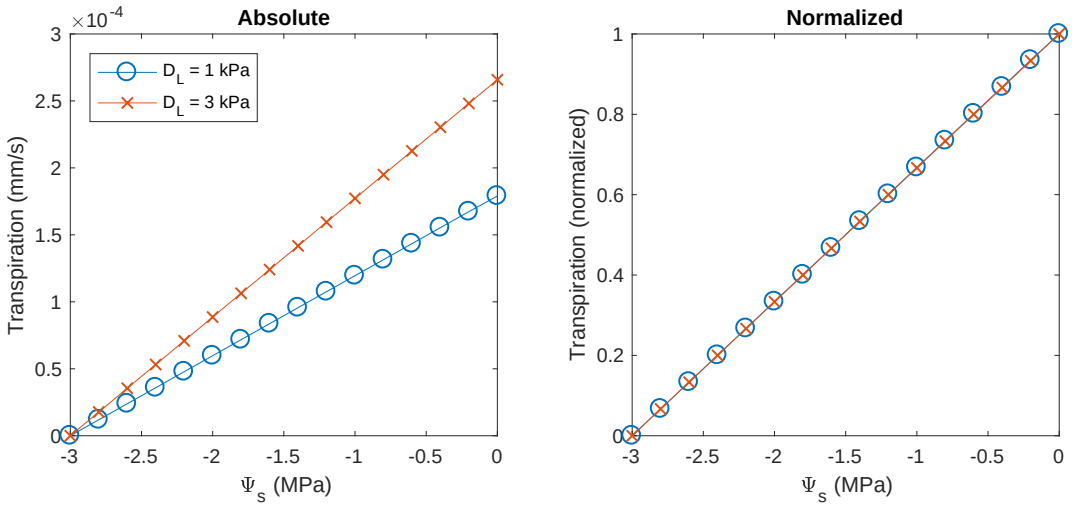

Figure C.1: Transpiration for a change in mean D_L

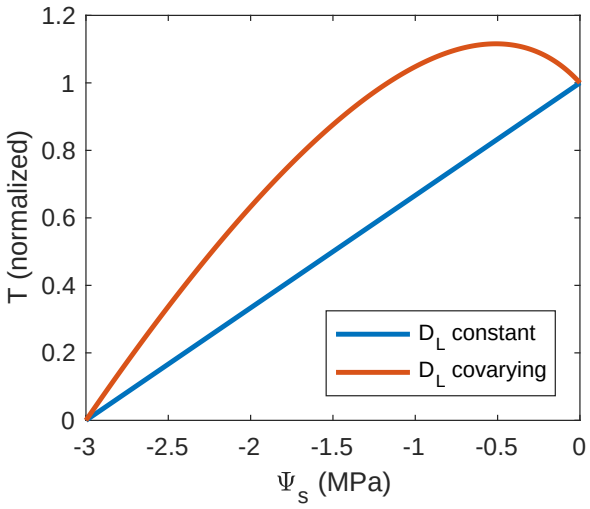

Figure C.2: Transpiration under constant and covarying D_L